

Active Manipulation of Extracellular Matrix Stiffness

SAHAN CHRISTIE BANDARA HERATH
B. Eng (Hons.), NUS

A THESIS SUBMITTED FOR THE DEGREE OF
DOCTOR OF PHILOSOPHY

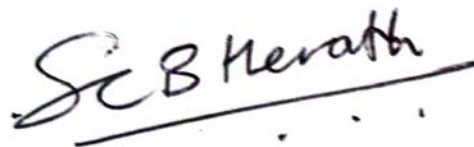
DEPARTMENT OF MECHANICAL
ENGINEERING
NATIONAL UNIVERSITY OF SINGAPORE

2014

Declaration

I hereby declare that this thesis is my original work and it has been written by me in its entirety. I have duly acknowledged all the sources of information which have been used in the thesis.

This thesis has also not been submitted for any degree in any university previously.

A handwritten signature in black ink, reading "S C B Herath", is written above a horizontal line. The signature is stylized and cursive.

Sahan Christie Bandara Herath

29 March 2014

Acknowledgements

I would like to express my sincere gratitude to my advisor Prof. Chen Chao Yu, Peter for the continuous support of my Ph.D study and research, for his patience, motivation, enthusiasm, and immense knowledge. His guidance helped me in all the time of research and writing of this thesis.

I would also like to thank my collaborators at BioSyM: Prof. Asada H. Harry, Dr. Shargi Namini Soheila, Dr. Ong Lee Ling Sharon, Dr Shi Hui and Mr Evan Tan for their encouragement, insightful comments, and hard questions.

I thank my fellow labmates in Control and Mechatronics Group: Dr Zhou Shengfeng, Dr Nam Joo Hoo, Ms Du Yue, Ms Hian Hian and Mr Chng Chin Boon, for the stimulating discussions, for the sleepless nights working together before deadlines, and for all the fun we have had in the last four years.

Last but not the least, I would like to thank my family members: Mr Kolitha Herath, Mrs Pradeepa Herath and Dr Kanishka Herath, for continuously supporting me throughout my graduate student life.

Contents

Summary	vii
List of Figures	xx
List of Symbols	xxiv
1 Introduction	1
1.1 Extracellular matrix	1
1.2 Hierarchical structure of collagen	2
1.2.1 Collagen molecule	3
1.2.2 Collagen fibril	3
1.2.3 Collagen fibres	4
1.3 Mechanical properties of collagen, collagen fibers and tendons	4
1.4 Motivation and proposed research work	5
1.5 Approach	7
1.6 Significance of research work	8
1.7 Objectives and scope of work	10
1.8 Outline of the thesis	11
2 Literature review	13
2.1 Introduction	13
2.2 Angiogenesis	13
2.2.1 Angiogenesis for life, disease and medicine	14
2.2.2 Mechanism of angiogenesis and arteriogenesis	14
2.2.3 Significance of the mechanical properties of the ex- tracellular matrix for angiogenesis	16
2.3 Mechanical factors affecting cellular reactions to matrix stiff- ening	17
2.3.1 ECM strain and integrin spacing	17
2.3.2 Stress fiber interactions with ECM	18
2.3.3 Bell model	19
2.4 Methods on changing substrate stiffness	20
2.4.1 Changing collagen concentration	20
2.4.2 Changing polymerization temperature	20
2.4.3 Changing pH of collagen	21

2.5	Stiffness of substrate and traction forces of filopodia	22
2.6	Stiffness of substrate and focal adhesions	24
2.7	Cellular force sensing techniques	25
2.7.1	Micro pillar traction force analysis	25
2.7.2	Cell traction force microscopy	27
2.7.3	Thin silicone membrane	27
2.8	Existing magnetic beads traps	28
2.8.1	Six solenoids magnetic tweezers	28
2.8.2	High force magnetic needle trap	31
3	Evaluating the change in macro scale stiffness of modified ECM	34
3.1	Introduction	34
3.2	Approach	37
3.3	Modelling of ECM deformation	38
3.3.1	Model of ECM deformation under internal point loads	39
3.3.2	Determination of apparent stiffness of modified ECM under the influence of an external magnetic field . . .	43
3.4	Experiment	45
3.4.1	Embedding beads in ECM	45
3.4.2	Preparation of samples	46
3.4.3	Experimental setup and procedure	48
3.4.4	Data processing	49
3.5	Results and discussion	51
3.5.1	Determination of pure ECM stiffness	51
3.5.2	Change in stiffness of modified ECM induced by the external magnetic field	52
3.5.3	Stiffness of ECM with streptavidin-coated magnetic beads	54
3.5.4	Stiffness of ECM with PEG coated magnetic beads .	55
3.5.5	Comparison of ECM apparent stiffness obtained from simulation and experiment	55
3.6	Concluding remarks	56
3.6.1	Utility of the proposed ECM deformation model . . .	56
3.6.2	Implication of the proposed method for active manipulation of ECM stiffness	57
4	Evaluating the change in micro scale stiffness of modified ECM	60
4.1	Introduction	60
4.2	Experimental design and implementation	63
4.2.1	Experimental design	63
4.2.2	Embedding beads in ECM	64

4.2.3	Preparation of samples	65
4.2.4	Fabrication of magnet-collagen holder	66
4.2.5	Determining the Young's modulus of ECM samples by atomic force microscopy	67
4.2.6	Experimental procedure	69
4.3	Theoretical analysis of change in ECM stiffness	70
4.3.1	Deformation of ECM due to pre-tension	71
4.3.2	Determination of change in Young's modulus by curve- fitting	74
4.4	Results and discussion	76
4.4.1	Experimental results	76
4.4.2	Data analysis	78
4.4.3	Change in the stiffness of sample embedded with streptavidin-coated beads	80
4.4.4	Comparison of analytical and experimental results . .	80
4.4.5	Change in the stiffness of sample embedded with PEG-coated beads	81
4.4.6	Relatively small changes in apparent stiffness at micro- scale level may amplify significantly at macro-scale level	82
4.5	Concluding remarks	83
5	Effect of HMVEC sprouting behaviour in the modified ECM	84
5.1	Introduction	84
5.2	Material and methods	86
5.2.1	Human microvascular endothelial cell culture	87
5.2.2	Microfluidic device design	87
5.2.3	Embedding beads in ECM	88
5.2.4	Tissue culture in microfluidic device	89
5.2.5	Magnetic force gradient	91
5.2.6	Quantification of endothelial cell sprouts	92
5.2.7	Cell immunofluorescence staining	93
5.3	Results and discussion	94
5.3.1	Sprouting number and height of sprouts	94
5.3.2	HMVEC focal adhesion numbers and size are depen- dent on amount of prestress in ECM	96
5.4	Concluding remarks	102
6	Localisation of magnetic fields	104
6.1	Introduction	104
6.2	Magnetism	105
6.2.1	Magnetic material properties	108
6.2.2	Magnetic forces	109

6.2.3	Magnetic needles	110
6.2.4	Magnetic particles	112
6.3	Simulation of magnetic fields and forces generated by electromagnetic needle (EMN) configurations	113
6.3.1	Single EMN	115
6.3.2	Force calculation single EMN	116
6.3.3	Single collector configurations	117
6.4	Experimental determination of magnetic fields and forces generated by electromagnetic needle	121
6.4.1	Electromagnetic needle	121
6.4.2	Force calculation single EMN	122
6.4.3	Magnetic field mapping with microscopic hall sensor	125
6.5	Preliminary results of influencing HMVEC sprouting by changing local stiffness of ECM	128
6.5.1	Results and discussion	130
6.6	Concluding remarks	132
7	Conclusion	133
7.1	Contribution	134
7.2	Future work	136
	Appendix	139
1	Preparation of PEG coated magnetic beads	139
2	Polyethylene glycol (PEG) coating	140
3	Magnetic force	141
4	Modified Thompson- τ test	144

Summary

The mechanical properties of the cellular environment influence cell behaviour in processes such as differentiation, proliferation, and apoptosis. Researchers have mainly sought to understand the scientific principles and mechanisms underlying the effect of the stiffness of the extracellular matrix (ECM) on cell-environment interaction. Reported in this thesis is a novel approach to directly manipulate the ECM in order to produce the desired changes in its stiffness.

This approach involves embedding super paramagnetic beads into the ECM and applying an external magnetic field to induce forces on these individual magnetic beads. These forces collectively oppose or aid the ECM deformation caused by cellular organisms. The results from this thesis quantify the changes in the stiffness of the modified ECM at the macro- and micro-scale and demonstrate the possibility of using this technique for cell manipulation.

There are six key contributions reported in this thesis. First, a new method was developed to alter the stiffness of modified ECM samples, in which the embedded superparamagnetic beads were coated with streptavidin to form strong covalent bonds with the ECM fibers.

Second, the macro-scale uniaxial stiffness of a modified ECM with a magnetic field perpendicular to the direction of a tensile force was characterised and a mechanical model was used to validate the experimental stretch tests. The results showed that the macro-scale stiffness of the ECM could be increased by up to 59%.

Third, a novel and customised AFM setup was used to verify experimentally the changes in the micro-scale stiffness of the modified ECM. The results showed that the micro-scale stiffness could be increased by up to 25%.

Fourth, an *in vitro* method was developed to study HMVEC sprouting dur-

ing angiogenesis by using a microfluidic device containing modified ECM and under the influence of an external magnetic field. Experimental results showed that the change in stiffness of the ECM led to an increase in sprout height and the number of focal adhesions of sprouting HMVECs.

Fifth, a new method was developed to generate stronger and more localized magnetic fields. This was achieved by utilising a novel combination of electromagnetic needles (EMN) and collectors. An in-depth simulation study with preliminary experimental results, has demonstrated the effectiveness of this method for more precise manipulation of magnetic beads.

Sixth, a technique for using the EMN to exert point forces on magnetic beads embedded in a 3D ECM was developed. Observations of the reaction of HMVECs to these point forces in the 3D ECM point to the feasibility of this technique for practical application.

These six contributions provide a set of fundamentally significant results that can serve as a point of departure for further study in active manipulation of ECM stiffness. By controlling the stiffness of the ECM, it may be possible to influence many biological processes such as cell migration, angiogenesis, stem cell differentiation, lymphangiogenesis and metastasis.

List of Figures

1.1	Structure of Collagen. Adapted from [1].	2
1.2	Stress Strain plot of hydrated collagen. Adapted from [2]. . .	5
1.3	Schematic illustration of the proposed approach.	8
1.4	Electromagnetic needles (EMNs) characteristic force distance curves and behaviour of magnetic particles to needle tip geometry.	9

2.1	Phase-contrast (A H) and polarization optics (I and J) views of endothelial cells before (A, C, E, G, and I) and after (B, D, F, H, and J) mechanical stresses were applied to cell surface receptors. (A and B) Pulling on a single RGD-coated microbead (4.5- μ m diameter) 15 min after binding to integrins using an uncoated glass micropipette; only 2 sec passed between A and B. (C and D) Similar displacement of a surface-bound AcLDL coated microbead. (E and F) Mechanical displacement of RGD-coated beads bound to the surface of a cell permeabilized with 0.5% Triton X-100 prior to force application. (G and H) A spread cell before (G) and after (H) a fibronectin-coated micropipette was bound to cell surface integrins for 5 min and pulled laterally (downward in this view). (I and J) The same cell shown in G and H viewed under polarization optics; arrowheads indicate white birefringent spots in the region of nucleoli. The movement of the pipette is downward, and vertical black arrows indicate the extent of pipette displacement in all views. Adapted from [3].	18
2.2	Mean G' (solid symbols) and G'' (open symbols) from multiple frequency sweeps ($n = 3$ gels/polymerization temperature, 31 frequencies per sweep) steadily increase between 4 and 37°C. Polynomial trendlines have been added as a visual aid. Adapted from [4].	21
2.3	Typical stress-strain curves as a function of pH for self assembled type I collagen fibers. Curves shown are measured at 25°C as a function of pH. Adapted from [5].	22

2.4	ECM Stiffness Is Synergistic with ROCK-Mediated Myosin II Activity in Inhibiting EC Branching: (A) Mouse aortic ECs grown in collagen/PA/glass sandwich gels (B, C, E, and F) Maximum intensity projections of confocal image z series. ECs in soft ([B] and [C], 0.45 kPa) or stiff ([E] and [F], 14 kPa) collagen/ PA/glass sandwich gels. D) shows quantification of branches per cell for ECs in collagen/PA/glass sandwich gels of the stiffness shown, with or without 30 mMblebbistatin. (G) Quantification of branch tips per cell on 2D collagen/PA substrates versus in collagen/PA/glass sandwich gels. (H and I) Mouse ECs stained with BODIPY-phalloidin on soft ([H], 0.45 kPa) or stiff ([I], 14 kPa) PA gels covalently coupled with a 2D layer of collagen treatment. Adapted from [6].	24
2.5	Mechanics of Cell Migration. Adapted from [7].	26
2.6	Micro pillar array for sensing cell migration force. Adapted from [8].	26
2.7	A typical example of applying a matching algorithm to determine the substrate displacement field and a 3D FEM analysis to determine cell traction forces (CTFs). (A) Human patellar tendon fibroblast on a polyacrylamide gel with embedded fluorescent beads (not shown). (B) Substrate displacement field. (C) Recovered CTF field. Adapted from [9].	27
2.8	Magnetic tweezers Setup. Adapted from [10].	29
2.9	Images of a magnetic bead showing its diameter observed at various positions of the microscope focus plane. Adapted from [10].	31
2.10	Schematic view of the setup. Adapted from [11].	31
2.11	120 degrees cone of magnetic influence. Adapted from [11].	33

3.1	Illustration of the proposed approach.	38
3.2	The Standard Linear Solid Model (SLSM) consists of two springs (represented by the spring constants E_1 and E_2 , and a dash-pot with a damping coefficient η).	39
3.3	Model of the ECM sample with point loads due to the virtual beads.	42
3.4	(a) von Mises stress generated in the ECM, and (b) the z -directional deformation of the top surface (S1) of the ECM.	42
3.5	Force-deformation relationships for three types of ECM, i.e., pure ECM, ECM with beads at a concentration of 0.1 mg/ml and 0.5 mg/ml. The ECM with beads are exposed to an external magnetic field created by a pair of permanent magnets.	45
3.6	Teflon mold for collagen formation.	47
3.7	Experiment Setup. The stiffness of the ECM was evaluated by a stretch test using an Instron 8848 micro-force tester. The micro-force tester has a load cell rated at 10 N with a 0.001 N resolution.	49
3.8	(a) Stretch test result of a sample embedded with beads at a concentration of 0.5 mg/ml and in the presence (solid curve) and absence (dotted curve) of a magnetic field. (b) Linear sections of the graphs taken to estimate the stiffness of two samples.	50
3.9	Force-deformation relationship of pure ECM samples.	52
3.10	Summary of results from experiments.	53

3.11	Schematic illustration of bead-embedded ECM and interaction between collagen fibers and cells via focus adhesion under the influence of an external magnetic field.	57
4.1	Schematic illustration of bead-embedded ECM and interaction between collagen fibers and cells via focus adhesions under the influence of an external magnetic field. This scenario provides the motivation for the work reported in this chapter on the determination of the change in the apparent local stiffness of the ECM under the influence of an external magnetic field.	62
4.2	Schematic illustration of the proposed approach.	64
4.3	Solid model and actual holder.	67
4.4	(a) AFM setup for experiment. (b) Close-up view of an indentation site.	68
4.5	Detailed illustration of indentation areas and bead locations.	69
4.6	(a) ECM is deformed in the z -direction due to the pre-tension in the x -direction. (b) Deformation $\hat{\delta}_p$ of ECM region near the magnet in the z -direction due to pre-tension in the x -direction, and deformation δ due to indentation.	71
4.7	Schematic illustration of setting for calculating the deformation of ECM due to pre-tension in x -direction.	72
4.8	ECM deformation (due to magnetic forces acting on all embedded beads) obtained by numerical simulation.	73
4.9	Determination of λ^* by curve-fitting.	75

4.10	Plots of force F versus indentation depth δ at points 4 mm, 5 mm, and 7 mm away from the magnet for ECM embedded with magnetic beads, and for pure ECM.	76
4.11	Force vs tip-sample separation graphs (plotted using the JPK software) for the cases where the magnetic field is (a) absent and (b) present. Trace (red) and retrace (dark red) curve clearly show hysteresis due to the viscous and plastic behaviour of the collagen.	78
4.12	Stiffness values of samples embedded with streptavidin-coated beads and with PEG-coated beads.	79
5.1	Schematic illustration of the proposed approach. (a) The magnetic beads are embedded in the ECM via bio-conjugation between the beads and the ECM fiber. (b) Applying an external magnetic field on the ECM produces forces on beads.. The magnetic field also collectively produces a force gradient on the beads to resist the dislocation of the ECM fibers due to migration of ECs.	87
5.2	Microfluidic device for observation of HMVECs sprouting during angiogenesis. (a) The device is constructed from a PDMS layer made by standard soft lithographic techniques and bonded to a glass slide (b) The device consists of a central 3D collagen gel matrix (channel b) with a media channel on either side. The gel channel is bounded by 37 posts for the growth of endothelial cells. The endothelial cells were seeded in channel a.	88

5.3	<p>Experimental Setup (a) Four 5mm by 4mm by 3mm neodymium, iron and boron (NdFeB) alloyed magnets are placed next to the HMVEC monolayer with their poles facing the collagen channel. A VEGF gradient was added with the cell channel having 20ng/ml and the opposite channel having 40ng/ml. (b) View of the posts and the HMVEC monolayer with sprouts moving through the gel. The location of the permanent magnet is shown relative to the microfluidic device.</p>	89
5.4	<p>Reflectance image showing the location of superparamagnetic beads embedded in collagen. (a) Collagen - Bead matrix in the microfluidic device with posts. (b) Image obtained by 60x oil immersion objective lens in reflectance mode. The bright lines indicate collagen fibers and the bright spots are magnetic beads.</p>	90
5.5	<p>Magnet field and force analysis of BioMag superparamagnetic particles (a) Magnetic field generated, (b) Magnetic force on individual beads. The length of arrows and the grayscale intensities indicate the magnitude of force acting on each individual bead. (c) Magnetization of BioMag particles. Adapted from figure provided by Bangs Laboratory, Inc., U.S.A.</p>	92

5.6	Simulation of forces on magnetic beads in the ECM (a)An example of magnetic beads embedded in the ECM. The magnetic beads are arranged in two layers experiencing forces generated by a magnetic field which are shown by the arrows. The layer further away with 33 beads experiences a lesser force compared to the layer with 15 beads which describes a gradient of forces exerted on the ECM (b) von Mises stress in the ECM due to the gradient of magnetic forces produced by the two layers of magnetic beads. It can be seen that there are varying stresses exerted in the ECM gel due to the forces from the magnetic beads. The red areas indicate regions of higher stress. These regions are situated close to the sprouting area hence increasing the amount of prestress present in this area.	93
5.7	Sprouting behaviour and structure at different magnetic conditions. Images of ECs migration on Day 1 and Day 4 in collagen gel with beads, without magnetic field (a and b) and with magnetic field (c and d). More sprouts have occurred in (c) and (d) indicating a preferential HMVEC sprouting condition where the beads exert magnetic forces within the ECM.	95
5.8	Quantification of the extent of sprouting in microfluidic devices. (a) Height (h) of each sprout is measured and counted. (b) Average number of sprouts that have heights above $100\mu\text{m}$ for each scenario were measured on Day 4.	95

5.9	Confocal images of ECs on day 4. The nucleus is stained with 405 hoechst blue and the actin filament is stained with 488 phalloidin green. Greater expression of actin stress fibers were observed in (b) compared to (a). The leading cell's (tip cell) filopodia extensions are more in number and spread in (b) compared to (a). Brighter areas in the reflectance images (c) and (d) show higher collagen concentrations where the tip cells and lumen walls are located.	97
5.10	HMVECs stained with vinculin to observe Focal adhesions (red) and nucleus stained with Hoechst (blue). (a)Focal adhesion staining of ECs on Day 4 without a magnetic field and ECM with magnetic beads, (b)Focal adhesion staining of ECs on Day 4 with a magnetic field and ECM with magnetic beads, (c)Focal adhesion staining of ECs on Day 4 without a magnetic field and ECM without magnetic beads, (d)Focal adhesion staining of ECs on Day 4 with magnetic field and ECM without magnetic beads.	99
5.11	Quantification of focal adhesions according to numbers and size. (a)Example image of an Endothelial cell stained with vinculin in ECM with beads and with magnetic field, (b)An example of FA counting done with IMARIS spot counter imaging tool, (c)Diameter of the FAs were measured using IMARIS measuring tool. The largest diameters were selected and measured.	100
6.1	Magnetic Field generated by a coil.	107
6.2	Elementary magnetic dipole.	107

6.3	The hysteresis curve characterises the behaviour of materials when exposed to a magnetic field B. The magnetic field B is plotted against the magnetisation of the material. When a magnetic field is applied ferromagnetic materials exhibit a high magnetisation at their saturation. If the B field is removed the material retains part of the magnetisation. This is the remanence and if the inner magnetisation is completely removed a B field of the strength of the materials coercivity has to be applied. Contrary to ferromagnetic materials, paramagnetic and super paramagnetic don't exhibit any remanence and differ only in terms of their saturation magnetisation	110
6.4	Schematic cross section of a magnetic needle. Magnetic needles consist of two parts: a ferromagnetic core and a electrical conductor wrapped around the coil. Through the external electric current, a magnetic field is induced in the ferromagnetic material. The magnetic field in the core is very strong due to the magnetisation of the ferromagnetic core. Thus, the utilised field at the sample is a result of the form of the core and in particular, of the tip	111
6.5	Magnetic hysteresis curve of the utilised super paramagnetic streptavidin-coated magnetic beads, Bangs Laboratories (Fishers, IN).	113
6.6	Magnetic field determination from conical geometries	114
6.7	(a) A sketch of the geometry of EMN tip. (b) Magnetic B-Field generated by the EMN fabricated by the ETH Zurich. Strong fields are coloured red, weak blue. The maximal field strength is achieved at the tip of the needle. The sample is indicated at a distance of 250 um from the tip.	116
6.8	Total force acting on a single particle in the sample.	117

6.9	Magnetic Setup with a single collector. The first needle on the right side generates a magnetic field which is collected by the second non-generating needle. The tips of the needles are separated by distance a . Both needles are tilted at an angle β from the horizontal.	118
6.10	Simulation of the magnetic field and force generated by a single EMN and collector	119
6.11	(a) Simulation of the magnetic field strength for 3 different setups along the sample (b) Simulation of the magnetic forces for 3 different setups along the sample	120
6.12	(a) Schematic design of the EMN. (b) CAD model of the EMN holder. (c) Actual image of EMN and holder.	121
6.13	Experimental Setup	124
6.14	Microscopic images of super paramagnetic beads movement .	125
6.15	Microscopic hall sensors	125
6.16	Electromagnetic needle holder containing both EMN and collector spaced $440\mu\text{m}$ apart and at angle of 50°	126
6.17	Hallsensor fixed onto a micromanipulation stage and moved in steps of $50\mu\text{m}$ at a distance of $700\mu\text{m}$ from the tip of the EMN and collector	126
6.18	Sensitivity plot of microscopic hall sensor	127
6.19	Surface plots of hall sensor data with different EMN and collector configurations. The height and colour of the plots correspond to the magnitude of the magnetic field	127

6.20	(a) Vertical EMN produced and area of $1.54mm^2$ threshold at a magnitude of $0.095T$, (b) EMN at 50° produced and area of $3.55mm^2$ threshold at a magnitude of $0.095T$, (c) EMN and collector at 50° produced and area of $0.40mm^2$ threshold at a magnitude of $0.095T$	128
6.21	Example of endothelial sprouting	129
6.22	(a) Microfluidic device used for observation of HMVEC sprouting. (b) Experimental setup of endothelial cells and EMN in a confocal microscope installed together with an incubator	130
6.23	Changes in sprouting HMVEC with magnetic forces within ECM exerted by electromagnetic needle	131
1	FTIR analysis for PEG coating of magnetic beads.	141
2	(a) Simulated magnetic field (b) Magnetic forces acting on beads. The length of arrows and the gray level of the points indicate the magnitude and direction of the force exerted on individual beads.	142
3	Magnetization of BioMag particles. (Adapted from figure provided by Bangs Laboratory, Inc., U.S.A.)	143
4	Results of statistical analysis using the modified Thompson-test. The asterisk indicates the mean and the two horizontal lines above and below the asterisk indicate the Standard Error of the Mean (SEM). When the outliers in the data as presented in (a) are excluded, data scattering is reduced due to the smaller standard deviation (not shown) and the relevant difference between the means in all cases increases as shown in (b). The reduced SEM in (b) further indicates that the sample mean thus obtained is a better estimate of the actual stiffness of the ECM for all cases.	144

List of Symbols and Acronyms

Symbols

nN	Nano Newton
μN	Micro Newton
fN	Femto Newton
I_u	Input current
I_z	z-direction current
I_x	x-direction current
I_y	y-direction current
P_u	Proportional coefficients
K_u	Integral coefficients
F_u	Input force
m	Magnetic moment
V	Volume
V_H	Voltage output
V_{off}	Offset Voltage
ρ	Density

B	Magnetic field
B_x	Magnetic field in x direction
B_s	Saturation magnetic field
μ	Magnetic permeability
μ_0	Magnetic permeability of vacuum
μ_r	Relative magnetic permeability
J	Current density
M	Magnetisation
φ_m	Magnetic scalar potential
\dot{B}	Derivative of the shape function
D	Relationship between the stress and the strain in three dimensions
S	Surface
χ	Magnetic susceptibility
E_1	Spring constant 1
E_2	Spring constant 2
E_{pure}	Young's modulus of the pure ECM
E_{bead}	Young's modulus of modified ECM in the absence of the magnetic field
E_{mod}	Young's modulus of modified ECM in the presence of the magnetic field
E_{point}	Apparent stiffness of the pure ECM subjected to the pre-tension induced by the point forces representing the magnetic forces acting on the beads
η	Damping coefficient

π_p	Potential energy
π_s	Strain energy
$\vec{\epsilon}$	Strain vector
$\vec{\sigma}$	Stress vector
W_p	Work done on the ECM by the external force
\vec{Q}	Displacement vector
\vec{f}	Body force vector
$\vec{\Phi}$	Surface force vector
τ	Time constant
K_c	Assembly of element stiffness matrix
K_{c_e}	Element stiffness matrix
T	Tesla
k	stiffness
L	Length
Br	Residual induction
ν	Poissons ratio
δ	Indentation
$\hat{\delta}_{p,j}$	z-direction deformation at a point p
$r_{p,j}$	distance from magnetic to point p
$P_x(a_j)$	Hertz pressure field
$G_{xz}(r_{j,p})$	Greens function
ΔF	Extra force

Acronyms

ECM	Extracellular matrix
VEGF	Vascular endothelial growth factor
MMP	Matrix metalloproteinase
EMN	Electromagnetic needle
AFM	Atomic force Microscope
HMVECs	Human microvascular endothelial cells
ECFN	Embryonic chick forebrain neurons
ROCK	Rho kinases
FAKs	Focal Adhesion Kinases
FAs	Focal Adhesions
PDMS	Poly dimethyl siloxane
PEG	Polyethylene glycol
PTFE	Polytetrafluoroethylene
EDTA	Ethylenediaminetetraacetic acid
EGM	Endothelial Growth Medium
BSA	Bovine serum albumin
NdFeB	Neodymium, iron and boron

Chapter 1

Introduction

This chapter provides detailed background information about the macro and micro scale components in the extracellular matrix (ECM) which comprise mainly of collagen. The importance of ECM stiffness in influencing cellular behaviour is also discussed in this chapter. A novel approach used to change ECM stiffness is introduced and the key contributions made from utilising this approach are presented in this chapter.

1.1 Extracellular matrix

The development of modern analytical methods and tools is crucial in providing a deep understanding of diseases at the molecular, cellular and organ levels and such an understanding will essentially drive progress in medicine, as they offer novel solutions for the healthcare industry. A current challenge is to achieve an understanding of the behaviour of a cell population and develop new technologies to control it. It is well known that cell behaviour, such as differentiation, proliferation, apoptosis and locomotion, is influenced by the properties of the extracellular matrix (ECM) [12–14]. The stiffness of the ECM particularly influences cell locomotion [15, 16]. One possible means of controlling cell locomotion is to manipulate stiffness gradients in the ECM [17, 18].

The extracellular matrix comprises mainly of collagen, which is a protein found in vertebrates and which adds up to 66% of all proteins in the human body [19]. It has been documented that there are a total of 25 types of collagen [20]. Collagen type I is the main type of collagen present in the body and it is responsible for bearing the tensile stress in the body. For

this type of collagen, the collagen triple helices, (i.e. collagen molecules), are assembled in fibrils and cross-linked via the amino acids lysine and hydroxyl lysine present in their telopeptide regions [1, 21]. These fibrils are then bundled into fibres and, depending on the tissues, they are then assembled into fascicles like in tendon.

1.2 Hierarchical structure of collagen

Collagen can be found in both fibril and non-fibril forming structures. The fibril-forming collagen including type I, II, III, V and XI are the ones that provide the structural framework and the mechanical strength of tissues [1]. Collagen type I is the main focus of this thesis. Hence, the hierarchical structure of fibril-forming collagen will be described in this chapter. Collagen has a highly organised structure starting from the collagen molecule, fibril, fibre, and higher levels such as fascicles in a tendon [21, 22] as shown in Figure 1.1 below.

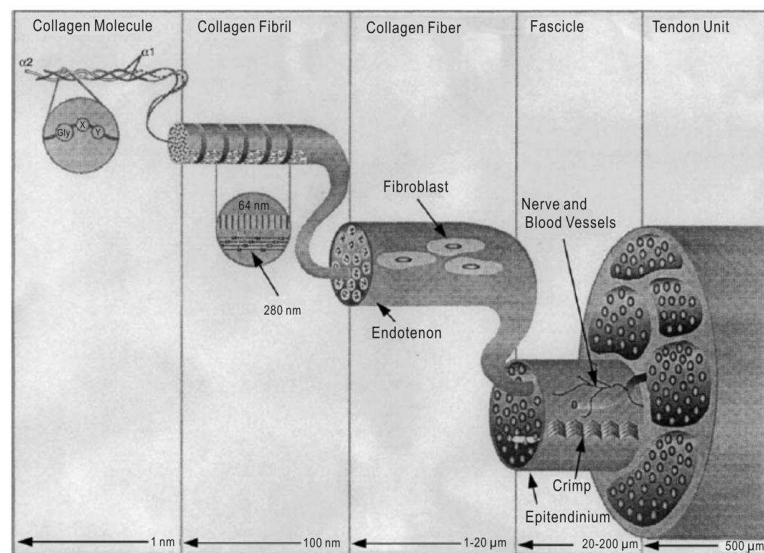


Figure 1.1: Structure of Collagen. Adapted from [1].

1.2.1 Collagen molecule

The smallest structure of collagen is the polypeptide chain, a linear collection of α -amino acids, comprising mainly the repeating tripeptide unit Gly-X-Y (Gly = glycine). The nature of the X and Y amino acid residues can vary but X is mostly proline (Pro) and Y is mostly hydroxyl-proline (Hyp) [23]. Three of these polypeptide chains are wrapped around each other forming a triple helix which is named the collagen molecule. Collagen molecules have a long, rod-like structure with a diameter of 1.5 nm, a length of 300 nm and a molecular weight of 285 kDa [21]. The triple helices of collagen type I are composed of two α 1-chains and one α 2-chain which differ only slightly in amino acid composition [24].

Collagen molecules are stable because of the hydrogen bonds between the backbones of the three α -chains and also because of the water-mediated hydrogen bonds. The hydrogen bonds are formed between the N-H group of Gly residues in one chain and the C=O group of a residue at the X-position in an adjacent chain [25].

1.2.2 Collagen fibril

The collagen fibril consists of self assembled collagen molecules. These fibrils are cylindrical in shape and have diameters ranging from 10 to 500 nm [26]. The distinct and regular pattern of the collagen fibrils can be observed by electron microscopy or atomic force microscopy. A D-period was highlighted in the model by Hodge and Petruska which occurs after every 67nm [27]. In this model, there are five collagen molecules arranged in a staggered formation.

There has been much debate over the conversion of the 2D Hodge and Petruska model to a 3D model. Several models have been proposed and they are all separated into two main categories. The first category is a model that describes five collagen molecules forming a microfibrillar structure with connections in the telopeptide region [21]. For the second category the collagen molecules form a crystalline 3D array [26]. For the first model the collagen molecular segments are tightly packed in the overlap

region and have more flexibility in the gap region [28]. This D-periodic five stranded microfibril model for molecular packing of collagen by Smith has been widely accepted [29]. The second category consists of quasi-crystalline 3D array models which are based on X-ray diffraction data. Hulmes and Miller developed this which was based on quasi-hexagonal molecular packing without microfibrillar sub-structure that showed a much better agreement with their X-ray diffraction data [30].

1.2.3 Collagen fibres

Collagen fibres are formed by arranging many collagen fibrils into bundles. The fibrils are arranged at angles to each other which results in a macroscopic crimped structure visible with an optical microscope [31]. These fibres form the structural frame of all biological fibril-forming collagen.

1.3 Mechanical properties of collagen, collagen fibers and tendons

Mechanical properties collected from tendons and collagen fibres have been the most comprehensive and exhaustive so far. The stress strain relationship of collagen fibres have been evaluated for many years. A typical stress strain plot of collagen in the hydrated state is shown in the Figure 1.2 [2].

The initial section of the graph is called the “toe region”. This region lies between 0 - 2% of the strain where there is high strain and low stress. The “toe region” is followed by the “heel region” where the stress increases as a result of the reduction in the disorder of the fibres in the collagen. At about 3% strain, the graph will reach the linear region, which defines the stress strain behaviour of the collagen fibres. The slope of the linear region is taken as the Young’s modulus of the collagen fibres.

The fibres in collagen usually have visco-elastic properties whereby their mechanical properties are strain rate dependent. This visco-elastic property

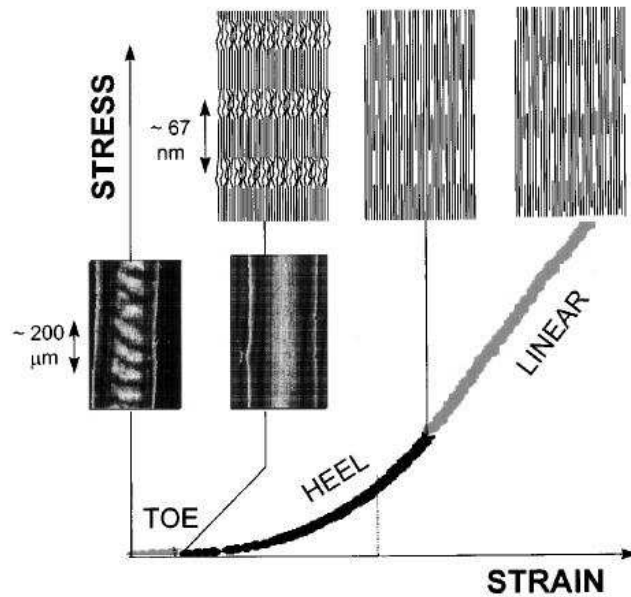


Figure 1.2: Stress Strain plot of hydrated collagen. Adapted from [2].

is considered to be important for collagen to behave as a substrate for cell growth [32]. Extensive tensile testing and synchrotron X-ray diffraction research into the visco-elastic behaviour of rat-tail tendon, has found that the overall strain of the collagen is larger than the strain of the individual fibrils which indicates that some deformation is taking place in the matrix between fibrils [33]. As a result of these findings, many authors have come up with a model that combines both collagen and collagen fibrils as a coupled visco-elastic system [34] [22]. There have also been suggestions that the tensile force is transmitted through the collagen directly to the fibrils and the sliding of collagen fibres with respect to each other is the main mechanism underlying the visco-elastic behaviour of collagen [35].

1.4 Motivation and proposed research work

The micro-environment surrounding cells plays an important role in influencing their behaviour (e.g. migration, proliferation and differentiation). Two groups of factors exert such an influence: the soluble cues and the insoluble cues. The first group involves biochemical components, such as

growth factors, metabolites and dissolved gases, while the second group involves structural and mechanical components, such as composition, architecture and elasticity of the ECM and cell-cell interactions. All these components can be found in the micro-environment.

To develop a comprehensive knowledge about cell behaviour in culture remains a challenge in fields such as life science, basic biological research [36], drug discovery [37], and tissue engineering/regenerative medicine [38]. Incorporating all these cues in the micro-environment for *in vitro* cultivation of cells is a crucial step towards gaining such knowledge. Significant work has been carried out to find the appropriate mixture of soluble cues in liquid media for culturing stem cells while the effect of insoluble cues has yet to be extensively investigated [39–42]. It is interesting to note that the impact of insoluble cues could in fact be far more important than previously thought, as in the case of mammalian cell and human mesenchymal stem cell differentiation [43].

The creation of new healthcare technologies and the quick diagnosis of disease require a deep understanding of chemistry, biology, medicine, and engineering, since the various biochemical pathways involving homeostasis are linked to tissue structure and function. Both mechanical and biochemical feedback loops exist in order to combine mechanical and chemical events that will provide a method for development and homeostasis. These mechanical and chemical feedback loops are altered during ageing and maturation of cells. Combined with cell death, these alterations will lead to the onset of diseases. For example, a stretch-dependent increase in tyrosine phosphorylation of Crk associated substrate protein (Cas) was shown to be involved in various cellular events such as migration, survival, transformation, and invasion [44]. Mechanical forces are responsible for ongoing changes that occur in diseased blood vessels. Mechanical forces also play an important role in the tissue homeostasis of musculoskeletal tissues as evidenced by the bone resorption and muscle atrophy experienced by astronauts, as well as in disease processes such as the deposition of lipids and the progression of atherosclerosis. Therefore, it is important not only to be able to measure the structure and normal function of tissues, but also to be able to understand the relationship between external mechanical

loading on tissues and the resultant changes in gene expression and protein synthesis.

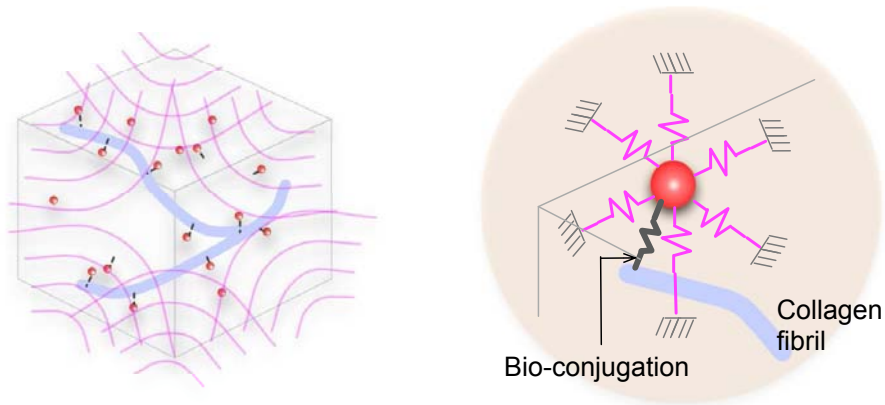
Epithelial, endothelial, and a variety of other cell types respond to external mechanical loading by changing the expression of certain genes and regulating the synthesis of several types of macromolecules. There are many biological products that are affected by mechanical loading for example the cell cytoplasmic structure and surrounding changes in the ECM is generally influenced by mechanical loading [45–47]. Therefore it is essential to understand the interaction between cells and mechanical forces present in the ECM.

1.5 Approach

In our proposed approach, superparamagnetic particles or beads were embedded in the ECM and manipulated with an external magnetic field to actively manipulate its stiffness. Embedding individual (or small numbers of) superparamagnetic particles in the ECM in order to probe cells or to manipulate cell-ECM interaction is a well-known practice [48] [49] [50].

The novelty of the proposed approach is that an ensemble of such magnetic particles will be directly manipulated to generate a desired stiffness for the extracellular matrix. Specifically, magnetic beads were embedded in the ECM via bio-conjugation between the beads and the ECM fibers. Applying an (external) magnetic field on the ECM produced a restoring force on the beads to resist the dislocation of the ECM fibers from their nominal positions due to forces generated by cell motility. This alters the apparent stiffness of the ECM as sensed by the cells. Figure 1.3 illustrates this approach.

Human microvascular endothelial cells (HMVECs) were cultured in the magnetic bead embedded ECM (modified ECM) and exposed to an external magnetic field to observe the effect of HMVEC sprouting under the modified ECM stiffness changes. A novel electromagnetic needle (EMN) design was also used to exert strong and localised point forces on the magnetic beads in the modified ECM. EMNs have been used in many biological



(a) Beads embedded in ECM via bio-conjugation and manipulated by an external magnetic field. (b) Magnetic field produces a restoring force on the bead to resist its motion.

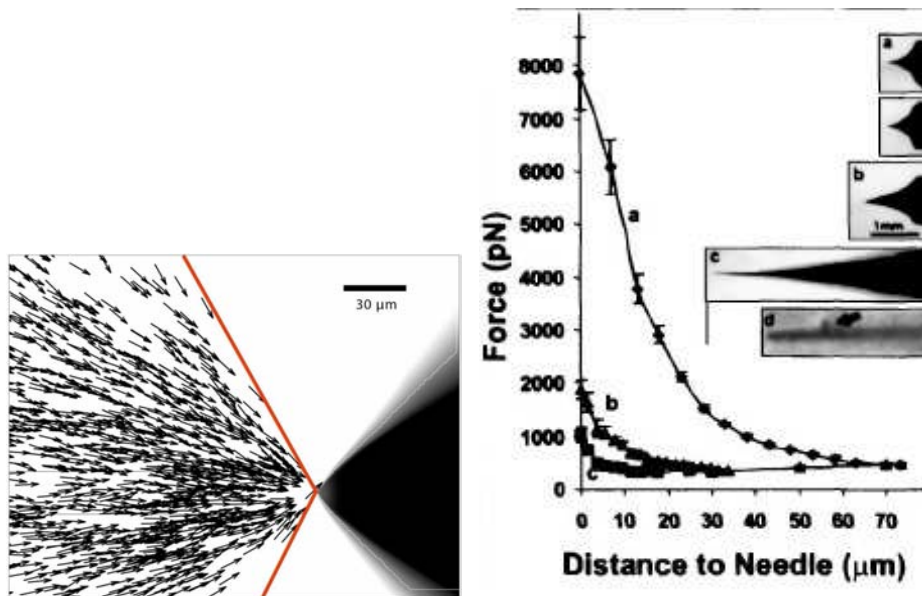
Figure 1.3: Schematic illustration of the proposed approach.

applications [10, 11, 49–55]. Most EMNs have single or double pole tips to generate a magnetic field gradient that induces a force on the magnetic beads. By creating more localised magnetic fields, these micro beads can be trapped and moved to arbitrary positions. If strong localised fields at the micro scale can be generated, vascularisation can be influenced through the application of forces to the micro beads in the vicinity of the leading cell (tip cell).

So far there have been a few attempts to generate localised magnetic fields with strong forces. Most EMNs that are able achieve such strong forces are due to the needle tip geometry and high input current [11] [51]. Such EMNs induce magnetic forces on micro magnetic beads that point directly towards the needle tip. The forces induced on these beads directly depends on the distance they are away from the needle tip as shown in Figure 1.4.

1.6 Significance of research work

The stiffness of the extracellular matrix (an insoluble cue) has been shown to influence cell behaviour [12] [15]. Studies from the literature concerning the stiffness of the extracellular matrix mainly sought to understand the sci-



(a) Force vectors point towards the needle tip. Force magnitude only depends on the bead-tip distance for all beads within a cone of about 120 around the tip. Adapted from [11].

(b) The lines in the graph indicate the force distance relationship for respective pole tip geometries measured using 4.5 μm magnetic beads in glycerol. Adapted from [51].

Figure 1.4: Electromagnetic needles (EMNs) characteristic force distance curves and behaviour of magnetic particles to needle tip geometry.

entific principles and mechanisms underlying its effect on cell-environment interaction [16]. For biosystems/bioengineering research, an immediate challenge is to develop engineering approaches to directly manipulate the extracellular matrix in order to produce the desired change in its stiffness. The work reported in this thesis explores the possibility of such manipulation of ECM stiffness.

This thesis describes an approach that achieves such manipulation, and reports experimental results that demonstrate the effectiveness of this proposed approach. The results show the possibility of altering the stiffness of the ECM to affect various biological processes such as proliferation, differentiation and apoptosis. This new platform for creating different stiffness gradients in the ECM will allow researchers and clinicians to analyse the reaction of cells for certain malignant conditions where the stiffness of the extracellular environment changes dynamically.

The work reported in this thesis will provide a new avenue to explore the

protein expressions and morphological changes that occur in different types of cells when the stiffness of its environment is manipulated. Furthermore this thesis will introduce a novel method of altering the stiffness in a localised area to provide single cell analysis of their reaction to these changes in stiffness.

There were six contributions made from the research work presented in this thesis. First, a new method was developed to alter the stiffness of modified ECM samples, in which the embedded superparamagnetic beads were coated with streptavidin to form strong covalent bonds with the ECM fibers. Second, the macro-scale uniaxial stiffness of a modified ECM with a magnetic field perpendicular to the direction of a tensile force was characterised. Third, an innovative method to quantify the micro-scale change in stiffness of a modified ECM in the presence of a magnetic field was developed. Fourth, an *in vitro* method was developed to study HMVEC sprouting during angiogenesis by using a microfluidic device containing modified ECM and under the influence of an external magnetic field. Fifth, in order to exert controlled point forces on individual or a smaller group of magnetic beads in a microscopic region of interest, a new method was developed to generate stronger and more localized magnetic fields. Sixth, a technique for using the EMN to exert point forces on magnetic beads embedded in a 3D ECM was developed.

1.7 Objectives and scope of work

The extracellular matrix (ECM) comprises the microscale collagen molecule which combined to form the macroscopic bundle of collagen fibrils known as collagen fibers. Therefore it is essential to verify our approach of manipulating the stiffness of the ECM in the macro and micro scale by carrying out individual mechanical tests at different scales.

The micro force tensile tester has been widely used to characterize the stiffness of several types of collagen [56–59]. Therefore the change in the modified ECM stiffness at macro scale was first tested with a microforce tester.

Once the change in the macroscale stiffness of the ECM has been verified, the change in microscale stiffness of the ECM was verified using an AFM indentation technique [60–63]. This provided a close investigation into the change in stiffness sensed by a cell migrating within such an environment.

Human microvascular endothelial cells (HMVECs) were introduced into the modified ECM. Their sprouting and vascularisation behaviour were observed in order to study the change in the modified ECM stiffness. This would help to quantify the effect of the change in stiffness of the modified ECM on HMVEC's sprout morphology and recruitment of certain proteins.

To locally influence the sprouting and migration of HMVECs in the modified ECM, magnetic forces were generated with a specialised electromagnetic needle (EMN). The EMN is capable of focusing the magnetic field to a microscopic region at its tip. By doing this it is possible to observe individual cells' reactions (eg tip cell) to external forces in the cells' vicinity.

In order to manipulate magnetic fields and forces on micro superparamagnetic beads in the microscopic scale, it requires the characterisation of the magnetic forces on such beads and the resultant magnetic fields generated by the EMN. To further localise the magnetic field, a collector was introduced to collect the stray field produced by the EMN. It has been observed that certain configurations of EMN and collectors have produced different levels of localised magnetic fields in the ECM. The localisation of magnetic fields will allow magnetic forces to be induced on individual or smaller groups of magnetic beads for precise manipulation of micro magnetic beads embedded in the ECM.

1.8 Outline of the thesis

The remaining chapters of this thesis are organised as follows:

Chapter 2 reviews different approaches that emphasize on angiogenesis,

the mechanics of visco-elastic deformation, and existing electromagnetic needles.

Chapter 3 and chapter 4 show the work done on the characterization of micro/macro-level stiffness of ECM embedded with magnetic beads via bioconjugation. These chapters show the changes in stiffness of the ECM due to the magnetic forces from magnetic beads embedded in the ECM. This study is essential to verify the possibility of changing the stiffness of the ECM by embedding magnetic beads in the ECM and applying external magnetic fields.

Chapter 5 presents the effect of in vitro 3D HMVEC sprouting during angiogenesis in the modified ECM exposed to a static external magnetic field. The sprouting length and number of focal adhesions formed by the endothelial cells are discussed and quantified in this chapter.

Chapter 6 discusses the design of an electro magnetic needle for localized manipulation of beads. Electro magnetic needles were designed and fabricated together with a specialised holder to use in an existing confocal microscope. The simulation and verification of experimental setups capable of generating highly localised magnetic fields and forces are demonstrated.

Chapter 7 summarises the work performed in this thesis and outlines some future research directions.

Chapter 2

Literature review

2.1 Introduction

The mechanical properties of the extracellular matrix have been an area of increasing interest in cell biological studies. Various bioengineering tools have been developed for quantitative investigation of how cells sense and respond to an external environment. These techniques are capable of quantifying the forces exerted on the extracellular matrix during cellular migration. The stiffness of the extracellular matrix plays a crucial role in the behaviour of cells particularly during angiogenesis. In this section, a review on angiogenesis is presented and an existing force sensing method for detecting cell migration forces will be described. Cell traction forces and focal adhesion protein expressions in different extracellular matrix stiffness will be reviewed. Existing magnetic bead trapping systems will also be discussed in detail for trapping and exerting forces on individual micro magnetic beads.

2.2 Angiogenesis

Blood vessels can be considered as a complex network of passages that delivers blood and nutrients to the body. Angiogenesis is described as the process of growing new blood vessels. Angiogenesis is one of the first events that occurs during organ development. It also occurs in wound healing by providing blood flow to injured tissues. Angiogenesis is controlled by an intricate balance of growth factors and inhibitors. If any imbalance

occurs this will lead to disease. The following sections will describe the development and characteristics of angiogenesis [64].

2.2.1 Angiogenesis for life, disease and medicine

In the embryo, blood vessels provide the growing organs the necessary nutrients and oxygen to develop. All blood vessels start from endothelial cells (ECs) which undergo different reactions to many different growth factors. Vascular Endothelial Growth Factor (VEGF) and its homologue VEGF-C are the key regulators of vascular and lymphatic EC sprouting respectively. The formation of blood vessels is a complex balance between various signals arising from integrins, angiopoetins, chemokines, junctional molecules, oxygen sensors, endogenous inhibitors, etc [65]. Endothelial cells have the ability to react to physiological stimulus such as hypoxia for blood vessels [65]. Therefore angiogenesis is reactivated for wound healing and repair. So far the best known cases where angiogenesis is activated are malignant, ocular and inflammatory disorders.

There have been intensive efforts in the past to inhibit angiogenesis in cancer, ocular, joint or skin disorders. Unfortunately, clinical trials testing the pro-angiogenic potential of VEGF as fibroblast growth factors (FGF) did not yield the expected results [66]. Angiogenesis does not initiate malignancy but promotes tumor progression and metastasis. Unlike tumour cells, ECs are stable and are considered the ideal entity for anti-angiogenic therapy. However, recent clinical experience with VEGF inhibitors provides an unclear conclusion. The anti-VEGF antibody Avastin only provides an effect in colorectal, breast and lung cancer patients when combined with conventional chemotherapy. It is still not clear why VEGF inhibitors alone do not prove effective in humans [67].

2.2.2 Mechanism of angiogenesis and arteriogenesis

Angiogenesis initiates with vasodilation, a process involving nitric oxide. Vascular permeability increases in response to VEGF and provides a platform for migrating endothelial cells. This increase in permeability is me-

diated by the formation of fenestrations, vesiculo-vacuolar organelles and the redistribution of platelet endothelial cell adhesion molecule (PECAM)-1 and vascular endothelial (VE)-cadherin, and involves Src kinases [68]. Although permeability promotes angiogenesis, excessive vascular leakage can be bad and lead to circulatory collapse, intracranial hypertension, formation of adhesions, metastasis, premenstrual discomfort or blindness. Angiopoietin (Ang) 1, a ligand of the endothelial Tie2 receptor, is a natural inhibitor of vascular permeability, tightening pre-existing vessels. When acutely administered to adult vessels, Ang1 protects against plasma leakage without profoundly affecting vascular morphology [69]. For endothelial cells to emigrate from their resident site, they need to loosen interendothelial cell contacts and to relieve periendothelial cell support; that is, mature vessels need to become destabilized. Ang2, an inhibitor of Tie2 signalling, may be involved in detaching smooth muscle cells and loosening the matrix [70] [71]. Proteinases of the plasminogen activator, matrix metalloproteinase (MMP), chymase or heparanase families influence angiogenesis by degrading matrix molecules and by activating or liberating growth factors (bFGF, VEGF and IGF-1), throughout the extracellular matrix [72].

Once the path has been cleared, proliferating endothelial cells migrate to distant sites. VEGF [73], placental growth factor (PLGF), VEGF-B, VEGF-C, VEGF-D and their receptors VEGFR2, VEGFR3 [74] and neuropilin-1 (a co-receptor of VEGFR2; [75]) have specific functions: VEGF and its receptor VEGFR2 affect embryonic, neonatal and pathological angiogenesis and are therapeutic targets, although much remains to be learned about the involvement of the distinct VEGF isoforms or of the heterodimers of VEGF family members.

Molecules involved in cell-cell or cell-matrix interactions, such as the $\alpha_v\beta_3$ integrin, which localizes MMP-2 at the endothelial cell surface, mediate endothelial spreading, explaining why $\alpha_v\beta_3$ antagonists inhibit angiogenesis [75]. Nitric oxide, a downstream effector of VEGF, TGF-1 and other angiogenic factors, is not essential for embryonic vascular development, but affects pathological angiogenesis and improves the reendothelialization of denuded vessels [76]. A growing list of molecules is being discovered that are angiogenic after exogenous administration, but whose endogenous an-

giogenic function remains undetermined.

Many stimulators and inhibitors affect adult blood vessel formation. Another difference between physiological or pathological angiogenesis, is that the latter is often induced by inflammation. Monocytes/macrophages, platelets, mast cells and other leukocytes are chemoattracted to sites of inflammation or wound healing, in part by angiogenic factors such as VEGF. These blood-borne cells produce angiogenic and arteriogenic factors (VEGF, bFGF, TGF-1, interleukin-8, PDGF, IGF-1, monocyte chemoattractant protein 1, TNF- and proteinases) that, in turn, attract endothelial and smooth muscle cells, fibroblasts, leukocytes or platelets [72] [77] [78].

2.2.3 Significance of the mechanical properties of the extracellular matrix for angiogenesis

From the earlier section, it can be seen that Vascular Endothelial Growth Factors is an essential soluble cue for the proliferation, differentiation and apoptosis. However unlike normal vascular pathways, tumour vessels are irregularly shaped and do not have uniform pericyte and base membrane covering [79] [80]. Limiting tumour vascular growth can improve cancer therapy. There had been attempts to control one of the growth factors, VEGF-A in particular, which is one of the frequent growth factors that promote tumour angiogenesis [81] [82]. However the anti-VEGF only provided short term effects. Hence a deeper understanding of the mechanisms required for the formation of tumour vascular structure is required.

Although soluble cues such as VEGF promote endothelial sprouting, endothelial cells also respond to external mechanical forces when the cells exert traction forces to the extracellular matrix through their focal adhesion complexes [83]. Contractile forces generated in the cytoskeleton keep the ECM in a tensile state [84]. These changes to the forces in the environment and the cells distortion will feedback to the cell and exert the right amount of cell tension [85] [86]. There has been work done to prove this mechanosensing effect of endothelial cells by exposing them to uniaxial cyclic strain during angiogenesis [87]. The results show that tumour en-

endothelial cells exhibit abnormal mechanosensitivity to uniaxial cyclic strain transmitted through the ECM, as seen by their failure to reorient perpendicularly to the strain direction. This abnormal mechanosensitivity arises from higher Rho-mediated tension, which suppresses the ability of tumour endothelial cells to reorient in response to applied mechanical strain. It enables these tumor endothelial cells to spread and form capillary networks over ECM material with a wide range of properties (stiffness), as compared with their normal counterparts. These differences in mechanosensitivity may explain why tumour microvessels exhibit much greater variability in shape and structural configuration than normal vessels, as well as why these vessels are dysfunctional. Further understanding of the role of the Rho signalling pathway and mechanotransduction in tumour vessel malformations may potentially lead to the development of novel vascular normalization and anti-cancer therapies in the future.

2.3 Mechanical factors affecting cellular reactions to matrix stiffening

2.3.1 ECM strain and integrin spacing

Research have reported that living cells and nuclei are programmed such that a mechanical tug on cell surface receptors can immediately change the organization of molecular assemblies in the cytoplasm and nucleus. When integrins were pulled by micromanipulating bound microbeads or micropipettes, cytoskeletal filaments reoriented, nuclei distorted, and nucleoli redistributed along the axis of the applied tension field. These effects were specific for integrins, independent of cortical membrane distortion, and were mediated by direct linkages between the cytoskeleton and nucleus. Actin microfilaments mediated force transfer to the nucleus at low strain; however, tearing of the actin gel resulted with greater distortion. In contrast, intermediate filaments effectively mediated force transfer to the nucleus under both conditions as shown in Figure 2.1.

These filament systems also acted as molecular tension cables to mechani-

cally stiffen the nucleus and anchor it in place, whereas microtubules acted to hold open the intermediate filament lattice and to stabilize the nucleus against lateral compression. Molecular connections between integrins, cytoskeletal filaments, and nuclear scaffolds may therefore provide a discrete path for mechanical signal transfer through cells as well as a mechanism for producing integrated changes in cell and nuclear structure in response to changes in extracellular matrix adhesivity or mechanics [3].

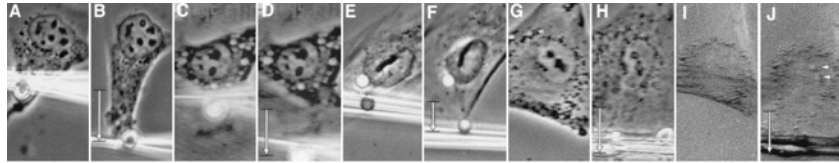


Figure 2.1: Phase-contrast (A H) and polarization optics (I and J) views of endothelial cells before (A, C, E, G, and I) and after (B, D, F, H, and J) mechanical stresses were applied to cell surface receptors. (A and B) Pulling on a single RGD-coated microbead (4.5- μ m diameter) 15 min after binding to integrins using an uncoated glass micropipette; only 2 sec passed between A and B. (C and D) Similar displacement of a surface-bound AcLDL coated microbead. (E and F) Mechanical displacement of RGD-coated beads bound to the surface of a cell permeabilized with 0.5% Triton X-100 prior to force application. (G and H) A spread cell before (G) and after (H) a fibronectin-coated micropipette was bound to cell surface integrins for 5 min and pulled laterally (downward in this view). (I and J) The same cell shown in G and H viewed under polarization optics; arrowheads indicate white birefringent spots in the region of nucleoli. The movement of the pipette is downward, and vertical black arrows indicate the extent of pipette displacement in all views. Adapted from [3].

2.3.2 Stress fiber interactions with ECM

Cytoskeletal tension is primarily associated with linear bundles of actin filaments known as stress fibers. Stress fibers in living cells terminate at discrete focal adhesions connecting the cytoskeleton to the extracellular matrix. Therefore, on a stiff substrate that cannot be deformed by the cell, stress fiber contraction leads to development of tension within the stress fiber. Since actin and myosin filaments are extensible structures a stress fiber under such tension should be elongated beyond its unloaded slack length.

To show the effect of stress fiber formation and disassembly, researchers have cultured human aortic endothelial cells on a pre-stretched silicone substrate coated with a fibronectin- like polymer. Release of the substrate caused stress fibers aligned in the shortening direction in adhered cells to buckle when compressed rapidly. Subsequently, the actin cytoskeleton completely disassembled in 5 sec and reassembled within 60 sec [88].

2.3.3 Bell model

The resistance of molecular bonds to rupture is of key importance to understanding cell-substrate adhesion. For many adhesion molecules, a key function of the adhesive bond is to resist forces in the body that would otherwise break cell-substrate contact. The "strength" of a receptor-ligand bond or multiple bonds is not a simple function of affinity, because bonds have "mechanical properties" that affect their ability to resist applied force. Whereas affinity is related only to the net energy change of a bond, mechanical properties are a function of the shape of the energy landscape in the transition states of bond formation and dissociation. Specific physical models have been proposed to describe the effect of force on receptor-ligand association and dissociation [89].

Bell proposed a model that uses an exponential relationship that had been demonstrated experimentally for the rupture of materials. In the Bell model, $k_{off} = k_{off}^0 \exp(\sigma F/kT)$ where k_{off}^0 is the k_{off} in absence of force, σ is the distance range of the bond potential-energy minimum. F is the force on the bond, k is Boltzmann's constant, and T is absolute temperature. Therefore the Bell model predicts that the dissociation rate, k_{off} , increases exponentially with force on the bond.

2.4 Methods on changing substrate stiffness

2.4.1 Changing collagen concentration

Changing the concentration of collagen has shown to vary the modulus of the ECM [90]. A stock solution of type I collagen at 5 mg/ml in 0.1% acetic acid was either diluted to make a 2 mg/ml solution or concentrated to make 10 or 15 mg/ml solutions. The concentration process was carried out by controlled evaporation of the solvent in sterile conditions. The collagen concentration was then estimated by hydroxyproline titration. Each collagen solution (at 2, 5, 10 or 15 mg/ml) and the culture medium were placed at 25 °C for 1 h before processing the hydrogels.

Mechanical properties of collagen hydrogels were then investigated by rheological measurements at day 0. Storage, G' and loss, G'' moduli were measured versus frequency. In each case, G' was around one decade superior to G'' which was to be related to a mainly elastic behavior and both G' and G'' were almost independent of frequency. Both features were typical of three-dimensional gels. Both moduli G' and G'' increased with collagen concentration from 0.66 mg/ml to 3 mg/ml which shows that collagen concentration plays a role in material rigidity. The elastic modulus (G') measured in 3 mg/ml was about twenty two times higher than 0.66 mg/ml. As this modulus is related to hydrogel stiffness, 3 mg/ml was drastically stiffer than 0.66 mg/ml.

2.4.2 Changing polymerization temperature

Fiber structure and fluorescent cross-link content of collagen hydrogels was systematically altered by changing polymerization temperature [4]. Collagen hydrogels were polymerized by mixing the following components in order on ice: 100 ml 10x phosphate buffered saline (PBS), consisting of 0.1 M phosphate buffer, 1.38 M NaCl, and 0.027 M KCl, pH 7.4), 0.41 ml ddH₂O with 0.025 M sodium hydroxide added (to reach a pH of 12.38), and 0.49 ml 8.16 mg/ml acid-soluble rat tail tendon collagen. After vortex-

ing, the collagen concentration was 4 mg/ml and pH 7.4. For multiphoton microscopy imaging, the collagen mixture was immediately pipetted into eight-chambered cover glasses at 0.1 ml/chamber and incubated for 48 h at four temperatures: 4, 14, 24, and 37°C. Typical values of the storage (G') and elastic (G'') modulus for the four polymerization conditions, measured for dynamic strain frequencies from 0.1 to 100 rad/s. Mean G' increases with polymerization temperature, roughly two orders of magnitude, from 0.3–0.2 Pa for 4°C-polymerized gels to 22.7–2.3 Pa for 37°C-polymerized gels and G'' increases in parallel with G' which can be seen from Figure 2.2

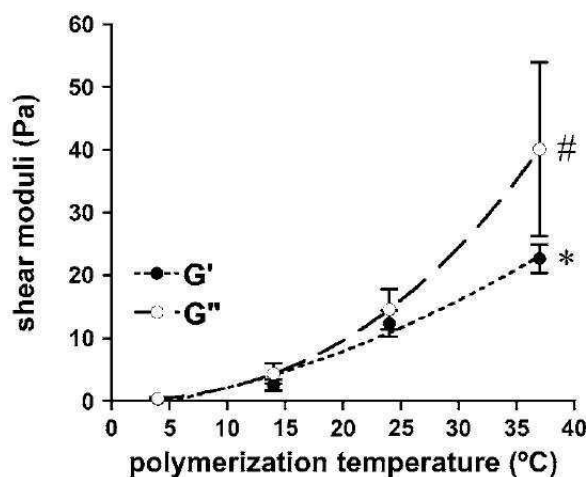


Figure 2.2: Mean G' (solid symbols) and G'' (open symbols) from multiple frequency sweeps ($n = 3$ gels/polymerization temperature, 31 frequencies per sweep) steadily increase between 4 and 37°C. Polynomial trendlines have been added as a visual aid. Adapted from [4].

2.4.3 Changing pH of collagen

Results of collagen fibril diameter distribution measurements show that the largest fibril diameters were approximately 40 nm and were obtained in the presence of glycine at pH 5.5 while the smallest diameters were seen at pH 8.5 and were approximately 20 nm. The presence of glycine increased the fibril diameter while the presence of

NaCl did not change the fibril diameter at pH 6.0. In general, fibers formed

at acidic pH tended to have larger fibril diameters than those formed at the neutral and basic pH values. Comparison of fiber types shows that for fibers formed at acidic pH values, the low strain modulus was greater than the high strain modulus indicating a greater resistance to deformation at low strains than at high strains. At higher pH the low strain moduli became smaller and the high strain moduli became greater, thus indicating that as incubation pH increased the resistance to deformation at low strain became less and increased at high strain as shown in Figure 2.3 [5].

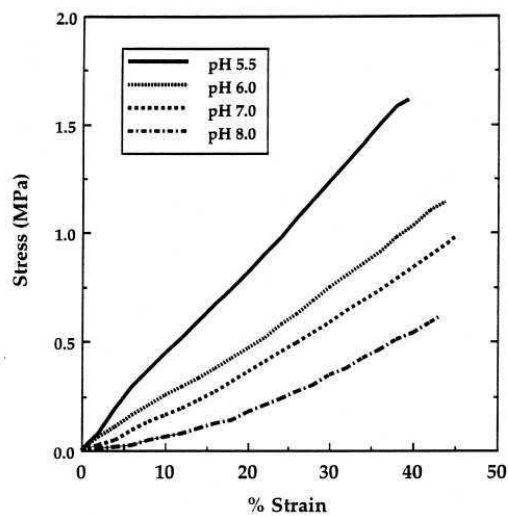


Figure 2.3: Typical stress-strain curves as a function of pH for self-assembled type I collagen fibers. Curves shown are measured at 25°C as a function of pH. Adapted from [5].

2.5 Stiffness of substrate and traction forces of filopodia

Cells sense the mechanical stiffness of their environment to control their own shape, migration and fate. A study conducted on embryonic chick forebrain neurons (ECFNs) by Chan *et al* [91], showed that retrograde flow was significantly slower on soft substrates ($P < 0.0001$). A stochastic model was constructed of the motor-clutch force transmission system, where molecular clutches link F-actin to the substrate and mechanically resist myosin-driven F-actin retrograde flow. The model predicts two distinct

regimes: (i) frictional slippage, with fast retrograde flow and low traction forces on stiff substrates and (ii) oscillatory load-and-fail dynamics, with slower retrograde flow and higher traction forces on soft substrates. Untransfected ECFNs also exhibited a similar response to substrate stiffness, suggesting that this effect is independent of GFP-actin. Filopodia on substrates with stiffness ranging from 730 to 1300 Pa showed high sensitivity to stiffness, abruptly increasing their retrograde flow rates as substrate stiffness increased (Figure 3D, blue region). Once substrate stiffness exceeded a critical value of 1300 Pa, retrograde flow rates became insensitive to stiffness, having a mean velocity of 110 nm/s. On extremely soft substrates (≤ 84 Pa), ECFNs appeared unhealthy, often dying within 1 to 2 days.

Another study done by Fisher *et al* developed an in vitro 3D Endothelial Cell (EC) model system in which migrating ECs display branched pseudopodia morphodynamics similar to those in living zebrafish [6]. Using this system, it was found that ECM stiffness and ROCK-mediated myosin II activity inhibit EC pseudopodial branch initiation. Figure 2.4 shows the reliance of stiffness in accordance with filopodia movement and branching.

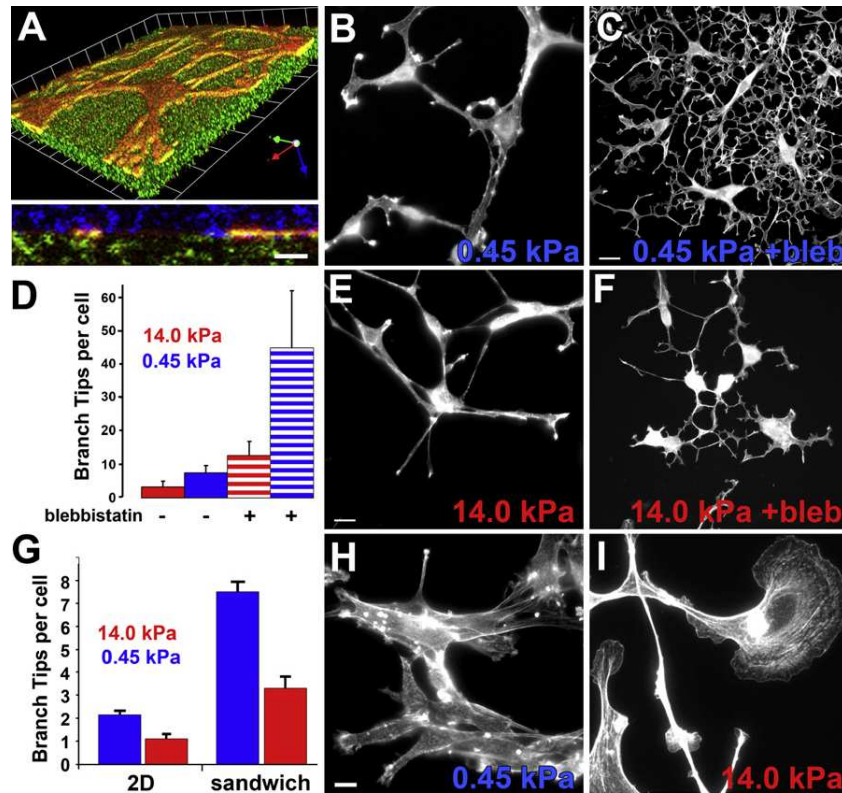


Figure 2.4: ECM Stiffness Is Synergistic with ROCK-Mediated Myosin II Activity in Inhibiting EC Branching: (A) Mouse aortic ECs grown in collagen/PA/glass sandwich gels (B, C, E, and F) Maximum intensity projections of confocal image z series. ECs in soft ([B] and [C], 0.45 kPa) or stiff ([E] and [F], 14 kPa) collagen/PA/glass sandwich gels. D) shows quantification of branches per cell for ECs in collagen/PA/glass sandwich gels of the stiffness shown, with or without 30 mM blebbistatin. (G) Quantification of branch tips per cell on 2D collagen/PA substrates versus in collagen/PA/glass sandwich gels. (H and I) Mouse ECs stained with BODIPY-phalloidin on soft ([H], 0.45 kPa) or stiff ([I], 14 kPa) PA gels covalently coupled with a 2D layer of collagen treatment. Adapted from [6].

2.6 Stiffness of substrate and focal adhesions

The size and number of focal adhesions (FA) have shown to be good indicators of cell migration dynamics. It has been observed that the mean size of focal adhesions robustly and precisely predicts cell speed independently of focal adhesion surface density [92]. There has also been evidence that cell motility and FAs are regulated by substrate flexibility. Pelham et al

have shown that the stiffer substrates produce an increased expression in FAKs such as vinculin, paxillin and phosphotyrosine [12]. This dependence on substrate stiffness for cell motility and ECs vascular formations shows the possibility of controlling angiogenesis through the variation of substrate stiffness.

Focal adhesions (FAs) are areas on a cell membrane that transmit force and regulate signals. They mediate Cell-ECM adhesions and interactions such as anchorage. FAs function as mechanical linkages to the ECM and serve as a biological signalling complex that concentrates and directs many signaling proteins through integrin binding and clustering [93]. Vinculin is known to be one of the primary protein that exists in FAs [94]. The adaptor protein vinculin is a key regulator of FAs and cells depleted of vinculin have fewer and smaller adhesions compared with wild-type cells [95]. Due to their dynamic nature, FAs may increase or decrease in size depending on the constituent proteins of the FAs. These proteins act in response to the external microenvironment. FAs are able to sense the stiffness of the extracellular matrix and act according to it [96]. A stiffer matrix contributes to more FAs. Furthermore focal adhesions on stiffer substrates are static, stronger, larger and more stable [12].

2.7 Cellular force sensing techniques

The mechanics of cell migration is shown in Figure 2.5. This shows that due to the propulsive forces that the cell exerts, the substrate will experience an equal and opposite force. Depending on either a stiffer or a more compliant substrate, the deformation of the substrate will reduce or increase respectively. Hence the stiffness of the extracellular matrix is very important for the purpose of mechanotransduction.

2.7.1 Micro pillar traction force analysis

A novel cell force sensor has been developed recently for the quantification of traction during cell spreading and contact guidance. This sensor provides

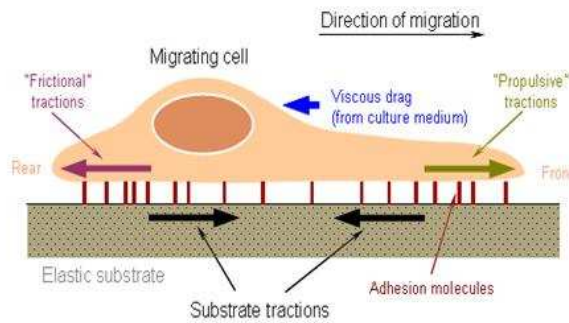


Figure 2.5: Mechanics of Cell Migration. Adapted from [7].

evidence that the cell does exert forces on its substrate during migration. The force sensor was fabricated by N. Tymchenko et al, which consists of tiny micro-scale Poly dimethyl siloxane (PDMS) pillars as shown in Figure 2.6. These pillars form a substrate for two types of cells to grow on, namely endothelial cells and fibroblast cells. Once the cells start to spread, the PDMS pillars will deform due to the traction forces exerted on them. These forces can then be quantified since the stiffness, deflection and dimensions of the PDMS pillars are all known. The forces detected by these micro pillar arrays indicate a force of 138nN for fibroblast cells and 57nN for endothelial cells [8].

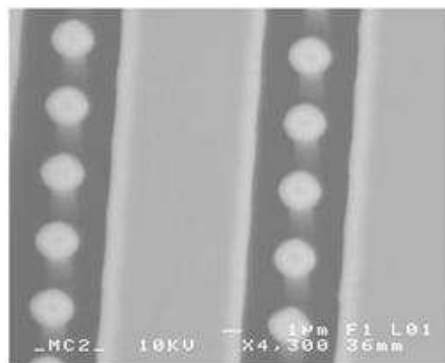


Figure 2.6: Micro pillar array for sensing cell migration force. Adapted from [8].

2.7.2 Cell traction force microscopy

The current cell traction force microscopy methods, which use elastic polyacrylamide gel substrate in measuring cell traction forces, follow a decoupled approach and involve three major steps. The first step is to fabricate elastic polyacrylamide gel substrate with a flat surface. The next step is to obtain a pair of "null force" and "force loaded" microscopy images, from which the displacement field is determined based on the movement of markers on the surface of the polyacrylamide gel substrate. In the final step, the substrate deformation is used to compute cell traction forces [9].

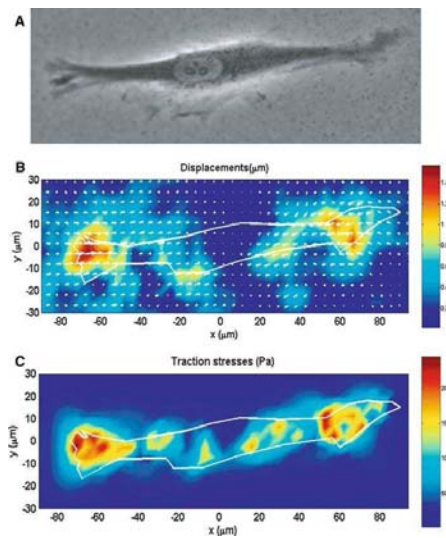


Figure 2.7: A typical example of applying a matching algorithm to determine the substrate displacement field and a 3D FEM analysis to determine cell traction forces (CTFs). (A) Human patellar tendon fibroblast on a polyacrylamide gel with embedded fluorescent beads (not shown). (B) Substrate displacement field. (C) Recovered CTF field. Adapted from [9].

2.7.3 Thin silicone membrane

The use of thin silicone membrane introduces another method to measure cell traction forces. Applying this technique, demonstrated that individual fibroblasts generate traction forces [97, 98], as evidenced by the fact that cells create wrinkles on thin silicone membrane. Force applied to the thin silicone membrane by an adherent cell is estimated by applying a flexible

microneedle to reverse the wrinkles. The needle stiffness is measured by hanging weights fabricated with small glass beads.

However, as wrinkling presents an inherently non-linear problem, there is currently no suitable computational method to accurately predict the wrinkles caused by a complex, non-isotropic traction force field generated by a single cell.

2.8 Existing magnetic beads traps

To be able to manipulate the beads and fix them in their specific locations, a suitable magnetic trap is required. This trap should be able to sense changes in the position of the magnetic beads and restore the beads back to their specific location. The basic principle behind this trap is to use machine vision to detect the deviation of the position of the beads and to produce a suitable force (by either changing the position of the electromagnet or the current in it) to bring the bead back to its original position. This section will discuss the available methods of trapping magnetic beads of the size of 1-4 microns in diameter.

2.8.1 Six solenoids magnetic tweezers

This is a setup produced by Gosse *et al* [10] involving six solenoids and a microscope based particle tracking system through a digital feedback loop as shown in Figure 2.8.

This setup is capable of creating a potential well of stiffness 10^{-7} N/m. By stretching a DNA molecule between a magnetic particle and a glass surface, vertical forces ranging from 50 fN to 20 pN were obtained. Similarly, nearly horizontal forces of up to 5 pN were obtained. The magnetic field was produced by six vertical coils made of copper. Different current configurations were used to move the magnetic beads along the x,y and z axes. Images of the sample were collected through the 100x oil immersion objective of an inverted microscope. A CCD camera operating in 50-Hz field mode sent the data to a video acquisition card installed in a computer. The 3D

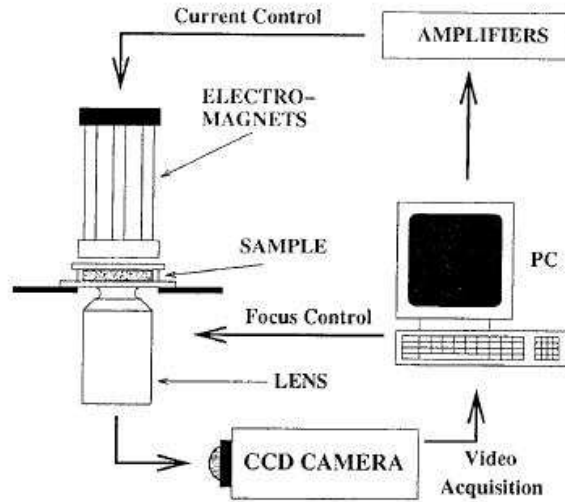


Figure 2.8: Magnetic tweezers Setup. Adapted from [10].

tracking of the bead was done in real time by a computer program. The x , y positions were first obtained by real-time correlation of the bead images (Gelles et al., 1988). Then the z position was obtained by the bead image which is surrounded with diffraction rings the diameter of which increases with the distance of the particle from the focal plane.

Digital proportional-integral feedback loops are used to lock a particle in a given position. In the horizontal plane, I_x and I_y are considered proportional to the main current I_z and are calculated as

$$I_u = -I_z C_u \text{ with } C_u = \left[P_u \bullet u + K_u \sum (u) \right] \quad (2.1)$$

In this equation, u corresponds to the error signal between the present position of the particle and the desired one; P_u and K_u are, respectively, the proportional and integral coefficients, $\sum(u)$ is the sum over the previous error signals; and C_u is the normalized correction signal.

Using only a proportional correction is equivalent to generating a force proportional to u , i.e., attaching the bead to a virtual spring whose stiffness k_u is directly determined by P_u . Let A_u be the proportionality factor between the force and the driving current associated with direction u , i.e. $F_u = A_u I_u$. Then

$$F_u = -A_u I_z P_u \bullet u \text{ and } k_u = A_u I_z P_u \quad (2.2)$$

Adding an integral term ($K_u \sum (u)$) is important to stabilize the bead to its exact reference position in the presence of a constant and continuously applied force (e.g., gravity). In this case, Equation 2 becomes

$$F_u = -A_u I_z C_u \quad (2.3)$$

The feedback in the z direction is done by monitoring I_z . However, the force applied on the bead is not a linear function of this current. To ensure a correct feedback, a square-root function was applied to the error signal,

$$I_z = I_0 \sqrt{-\left(P_u \bullet u + K_u \sum (u)\right)} \quad (2.4)$$

with I_0 being the current just required to equilibrate the bead weight. When the forces applied to the bead are small, the previous relations can be linearized around their means values,

$$I_z = I_0 \left(1 - \frac{(P_z \bullet z)}{2}\right) \text{ and } F_z = mg - A_z I_0^2 P_z \bullet z \quad (2.5)$$

Thus, the tweezer's vertical stiffness is given by

$$k_z = A_z I_0^2 P_z \quad (2.6)$$

The Figure 2.9 below shows how the camera detects the height of the bead using the bead image which is surrounded with diffraction rings the diameter of which increases with the distance of the particle from the focal plane.

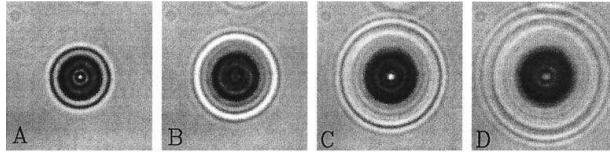


Figure 2.9: Images of a magnetic bead showing its diameter observed at various positions of the microscope focus plane. Adapted from [10].

2.8.2 High force magnetic needle trap

This setup is inexpensive and capable of generating a large force of about 100 nN on 5 μm magnetic beads. The application of such large forces can be used to characterize the local viscoelasticity of soft materials in the non-linear regime, or to study force-regulated processes and mechanochemical signal transduction in living cells and their environment [11]. The set up is shown in Figure 2.10.

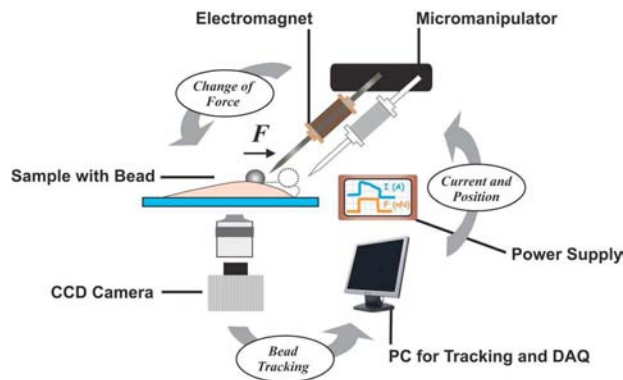


Figure 2.10: Schematic view of the setup. Adapted from [11].

The magnetic microneedle consists of a cylindrical rod made of high permeability nickel alloy. The core has a diameter of 4.5 mm and a length of 100 mm. One end is tapered and has a sharp tip with radius of $< 10\mu\text{m}$. If a magnetic bead with volume V and magnetic susceptibility χ is exposed to an external magnetic field $H = B/\mu$, the field induces in the bead a magnetic moment

$$m = \chi \times V \times H \quad (2.7)$$

and the force is given by

$$F = \left(m \bullet \frac{\partial}{\partial r} \right) B \quad (2.8)$$

The force calibration is done by immersing the needle into a solution, and bead movements are tracked during repeated current on-off cycles, with each on or off phase lasting 1 s. Settling of the viscous fluid causes a bead drift, which was determined during the current-off phases. The force acting on a bead during the current-on phase was then computed from the drift-corrected velocities v according to Stokes formula for viscous drag,

$$F = 6\pi \times \eta r \times v \quad (2.9)$$

Force distance curves for multiple beads and currents are recorded, and a simple mathematical expression is fitted to the data of all beads, distances, forces, and currents.

$$F = F_0 \times \left(\frac{d}{d_0} \right)^{c(I)} \quad (2.10)$$

where the function $c(I)$ is given by

$$c(I) = \frac{c_1}{1 + c_2 \times \exp(c_3 \times I)} \quad (2.11)$$

The magnitude of the magnetic field gradient, and hence the force magnitude, depends crucially on the shape of the needle tip. The stongest forces and steepest gradients are obtained using the smallest possible tip radius. The direction of forces was found to point always to the surface normal of the tip. That means, for beads within an angle of about 120° around the tip and at a distance not larger than 100μ m from the tip, the force vector points towards the center of the circle describing the tip as shown in Figure 2.11.

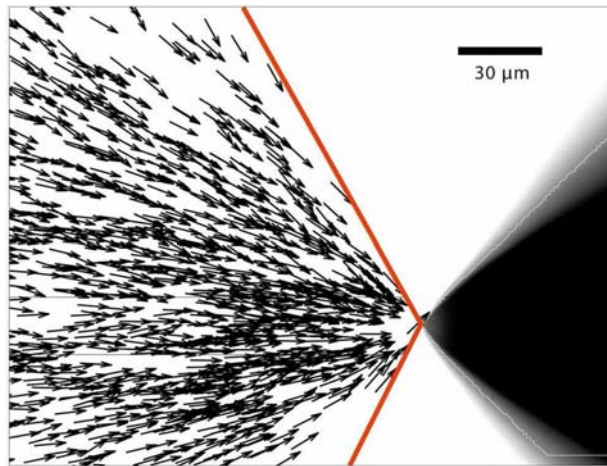


Figure 2.11: 120 degrees cone of magnetic influence. Adapted from [11].

Chapter 3

Evaluating the change in macro scale stiffness of modified ECM

3.1 Introduction

The extracellular matrix (ECM) ranges from the microscale collagen molecule to the macroscopic bundle of collagen fibrils known as collagen fibers. Therefore it is essential to verify the approach to manipulate the stiffness of the ECM in the macro(1cm-5cm) and micro scale (1-10 μ m) by carrying out individual mechanical tests at different scales. In this chapter, this approach is applied to investigate changes in the macroscale stiffness of the ECM.

The microenvironment surrounding cells plays an important role in influencing their behavior, e.g., migration, proliferation and differentiation. Two groups of factors exert such influence: the soluble cues and the insoluble cues. The first group concerns biochemical means, including growth factors (such as the vascular endothelial growth factor, VEGF), metabolites and dissolved gases, while the second group involves structural and mechanical properties, such as composition, architecture and elasticity of the extracellular matrix and cell-cell interactions.

Developing comprehensive knowledge about cell behavior in culture remains a challenge in basic biological research [36], drug discovery [37], tissue engineering, and regenerative medicine [38]. Incorporating all these

cues in the microenvironment for *in vitro* cultivation of cells is a crucial step in gaining such knowledge. Significant advances have been made on finding the appropriate mixture of soluble cues in liquid media for culturing various types of cells, while the effect of insoluble cues remains a fertile area to be explored [39] [40] [41] [42]. It is interesting to note that the impact of insoluble cues in fact could be far more important than previously thought, as is illustrated in the case of mammalian cell and human mesenchymal stem cell differentiation [43].

The stiffness of the ECM (an insoluble cue) is known to influence many types of cellular behavior [12] [15]. Cells within tissues can sense the mechanical stiffness of both the ECM and other cells. ECM stiffness regulates the degree of cell-matrix adhesion, the size of the focal adhesion, as well as the stiffness and tension developed by the cell itself [17] [99]. Motility and cell alignment are also associated with ECM stiffness, manifested in the tendency of cells to migrate from softer to stiffer environment [100]. At the basic level, ECM stiffness can regulate cell growth and viability, as well as resistance to apoptosis. Although the mechanisms of many of these effects are still unknown, it is generally accepted that the mechanical properties of the ECM influence cell biology at various levels, including protein expression [101].

A number of methods have been proposed in the literature for changing the stiffness of collagen for the purpose of observing *in vitro* cell behavior in an ECM sample [102] [103]. One involves changing collagen concentration, as demonstrated in the work by Helary et al [90]. Another method involves varying the pH value in a sample, since solution acidity during fibrillogenesis affects collagen stiffness. Silver et al showed that the Young's modulus of an ECM sample changed from 0.5 MPa to 5.5 MPa when the pH value was reduced from 8.5 to 6 at 37°C [5]. Changing the temperature of an ECM sample can also lead to change in its stiffness. The Young's modulus of ECM samples has also been shown to increase with polymerization temperature, e.g., from 0.3 Pa at 4°C to 22.7 Pa at 37°C [4]. These currently known methods mainly rely on manipulating soluble cues.

Manipulating the stiffness of ECM by mechanical means offers an alternative to approaches that rely on soluble cues. Recent results have demon-

strated the possibility of changing mechanical and rheological properties of composites with highly elastic polymer matrices that are filled with magnetic particles [104] [105]. It had been reported that these materials show significant change in their mechanical properties under the influence of magnetic fields.

An approach to alter the stiffness of ECM samples by mechanically manipulating the deformability of the collagen fibers in the ECM was proposed recently. A very brief description of the concept underlying this approach was initially presented (with limited preliminary experimental data) in [106]. This approach involves embedding micron-size magnetic beads in an ECM sample (hereafter referred to as an *modified* ECM sample) through bio-conjugation between the streptavidin-coated beads and the collagen fibers, then applying an external a magnetic field on the sample to exert a magnetic force on the beads. Embedding a single or very few superparamagnetic particles in the ECM in order to probe cells or to manipulate cell-ECM interaction is a well-known practice [48] [49] [50]. The novelty of our proposed approach manifests in the ability to directly manipulate an ensemble of such magnetic particles to alter the apparent stiffness of the macrostructure. While the basic concept and some very preliminary results have been briefly reported in [106], to develop this approach into a practical technique for *in vitro* manipulation of cellular behavior requires a substantive quantitative characterization of the effect of an external magnetic field on the stiffness of the modified ECM. The work reported in this chapter focuses on establishing such a characterization by means of both detailed analytical modeling and extensive experimental investigation.

Specifically, in this chapter investigation was done on the effect of an external magnetic field on the uniaxial stiffness of modified ECM samples by (i) developing an analytical model (described by a set of constitutive equations) of the behavior of the modified ECM under the influence of an external magnetic field, (ii) designing and implementing a stretch test to quantify such changes based on statistically meaningful data collected from a set of carefully designed experiments, and (iii) evaluating the effectiveness of this approach by comparing the analytical and the experimental results.

The remainder of this chapter is organized as follows. Section 2 presents an overview of the approach and the general principles in the design of the experiments. Section 3 develops an analytical model describing the viscoelastic behavior of the modified ECM samples under the influence of an external magnetic field. Section 4 describes the design and the implementation of the experiments and presents the results. Section 5 evaluates the results from the analysis and the experiments, and discusses the implication of the results and directions for further research to improve the practicality of the proposed approach.

3.2 Approach

Superparamagnetic beads are embedded in the ECM via bio-conjugation between the beads and the ECM fibers. The beads are coated with streptavidin that enables the formation of strong covalent bonds between the beads and the collagen fibers in the ECM, as is illustrated in Figure 3.1a. Applying an external magnetic field on the beads produces a pre-tension (along in the direction of the magnetic field) in a region in the ECM due to the magnetic forces experienced by the beads. This externally created pre-tension can be configured to generate resistance to the deformation of the collagen fibers in that region, which in turn affects the deformation of the ECM. This resistance to deformation manifests in the change in the apparent stiffness of the ECM.

This change in the apparent stiffness was characterised in one dimension in the setting of a stretching test, as is illustrated in Figure 3.1c. A modified ECM strip is fixed at one end while the other end is stretched. During the stretching, two magnets (one on each side of the ECM strip) produce two magnetic forces on the individual beads. Each of these two forces can be resolved into two components: one along the axis of stretching and point towards the center line between the two magnets, while the other pointing towards a magnet. Figure 3.1c illustrates this situation for the case where the bead is initially located near the center line of the two magnets. The distribution of deformation in the collagen can be observed from Figure

3.1b, which shows a greater deformation in the region of the ECM closer to the free moving end than in the fixed end. Since the deformation is greater at the point where the stretching force is applied and reduces linearly to zero at the fixed end, the beads located above the magnets are displaced more significantly than the beads located below the magnets.

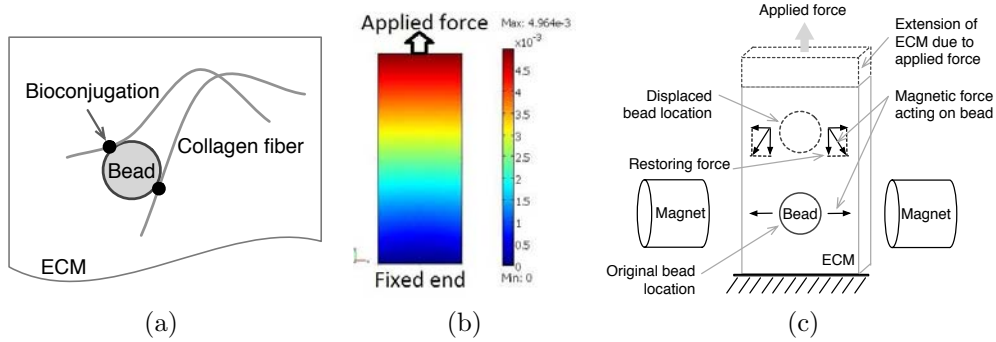


Figure 3.1: Illustration of the proposed approach.

The beads above the magnet experiences a downwards force that opposes the deformation of the collagen. Therefore a larger force is required to overcome these forces while stretching. The magnetic field also induces forces on the beads perpendicular to the direction of stretching. This force will also reduce the tensile deformation caused by the stretching force.

3.3 Modelling of ECM deformation

In a modified ECM sample, the beads (with a diameter of approximately $1.5 \mu\text{m}$) are thoroughly mixed with the collagen solution to ensure a uniform distribution. At a typical bead concentration of 0.1 to 0.5 mg/ml, the number of beads is in the order of 10^8 . Such a large number of beads poses a problem in constructing a model for describing the viscoelastic behaviour of the modified ECM using existing FEM techniques, since in these techniques the beads need to be accounted for individually. A model is thus developed to analyze the structural mechanics of the modified ECM in which the ECM is treated as viscoelastic and subjected to numerous distributed point loads generated by the magnetic beads when under the influence of a magnetic field.

3.3.1 Model of ECM deformation under internal point loads

The viscoelasticity of the ECM (prepared from Rat Tail Collagen Type I) is modelled by using the Standard Linear Solid Model (SLSM), which consists of two springs and a dashpot, as is illustrated in Figure 3.2. Compared to the Maxwell model and the Kelvin-Voigt model, the SLSM describes the deformation behaviour of viscoelastic material more accurately. An instantaneous elastic deformation is observed when a viscoelastic material experiences an instantaneous stress. The existence of E_2 in the SLSM contributes to the improved accuracy in the model for describing such an instantaneous deformation [107]. From this conceptual model shown in Figure 3.2, various constitutive equations that link stress with strain have been developed [108] [109] [110] [111].

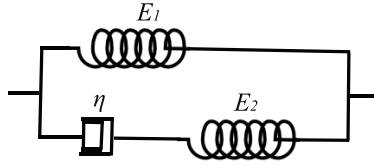


Figure 3.2: The Standard Linear Solid Model (SLSM) consists of two springs (represented by the spring constants E_1 and E_2 , and a dash-pot with a damping coefficient η).

The method employed in the derivation of viscoelastic deformation (due to an external force) of an ECM sample follows the principle of minimum potential energy. This method seeks to determine a deformation state of the ECM corresponding to a minimum potential energy over all possible deformation states [112] (The notations of some parameters in [112] are used in this chapter). The potential energy π_p is defined as

$$\pi_p = \pi_s - W_p,$$

where π_s is the strain energy involving the strain $\vec{\epsilon}$ and the stress $\vec{\sigma}$, and is given by

$$\pi_s = \frac{1}{2} \iiint_V \vec{\epsilon}^T \vec{\sigma} dV,$$

while W_p is the work done on the ECM by the external force, i.e.,

$$W_p = \iiint_V \vec{Q}^T \vec{f} dV + \iint_S \vec{Q}^T \vec{\Phi} dS + \sum_i \vec{Q}_i^T \vec{P}_i,$$

with \vec{Q} being the displacement vector, \vec{f} , $\vec{\Phi}$ and \vec{P}_i the body force vector, the surface force vector, and the point force vector, respectively, V the volume of the ECM, and S the surface of the ECM that experiences the surface force.

The stress $\vec{\sigma}$ is derived based on the viscoelastic constitutive model developed in [108]. The total stress $\vec{\sigma}$ is given as

$$\vec{\sigma} = \vec{\sigma}_1 + \vec{\sigma}_2,$$

with $\vec{\sigma}_1$ and $\vec{\sigma}_2$ being the elastic stress generated in the springs $E1$ and spring $E2$, respectively. From $\vec{\varepsilon} = \dot{B}\vec{Q}$ (with \dot{B} being the derivative of the shape function with respect to the physical coordinates), $\vec{\sigma}_1$ is expressed as $D_1\dot{B}\vec{Q}$, where D_1 represents the relationship between the stress and the strain in three dimensions for the spring E_1 . The stress $\vec{\sigma}_2$ for the spring $E2$ can be estimated recursively as

$$\vec{\sigma}_2^{n+1} \approx e^{-\frac{\Delta t}{\tau}} \vec{\sigma}_2^n + \alpha \frac{1 - e^{-\Delta t/\tau}}{\Delta t/\tau} \left(\vec{\sigma}_1^{n+1} - \vec{\sigma}_1^n \right),$$

where $\tau = E2/\eta$ is the time constant, and α is the relative stiffness $E2/E1$. Hence, the total stress $\vec{\sigma}$ is

$$\vec{\sigma}^{n+1} \approx \vec{\sigma}_1^{n+1} + e^{-\frac{\Delta t}{\tau}} \vec{\sigma}_2^n + \alpha \frac{1 - e^{-\frac{\Delta t}{\tau}}}{\Delta t/\tau} \left(\vec{\sigma}_1^{n+1} - \vec{\sigma}_1^n \right). \quad (3.1)$$

The numerical approach based on the finite element method is applied for analyzing the structural mechanics of the modified ECM. The ECM is meshed into a total of m four-node linear tetrahedron elements. The generated nodal displacements can be converted to the displacement at any point in the ECM. The potential energy at time step $(n + 1)$ is

$$\begin{aligned}
\pi_p^{n+1} = & \frac{1}{2} \vec{Q}^{n+1T} \sum_{e=1}^m \iiint_{V_e} \dot{B}^T \vec{\sigma}^{n+1} dV - \\
& \vec{Q}^{n+1T} \sum_{e=1}^m \left(\iiint_{V_e} N^T \vec{f}^{n+1} dV + \right. \\
& \left. \iint_S N^T \vec{\Phi}^{n+1} dS \right) - \vec{Q}_i^{n+1T} \vec{P}_i. \tag{3.2}
\end{aligned}$$

The deformation state corresponding to a minimum potential energy is obtained by solving $\partial \pi_p^{n+1} / \partial \vec{Q}^{n+1} = 0$, leading to the formula to generate the nodal displacements at time step $(n+1)$, i.e.,

$$\begin{aligned}
\vec{Q}^{n+1} = & \frac{1}{2} [K_{inst}^{n+1}]^{-1} \left[K_c \vec{Q}^n \left(\frac{\alpha(1 - e^{-\frac{n\Delta t}{\tau}})}{n\Delta t/\tau} \right) \right. \\
& \left. - (B')^T \vec{\sigma}_2^n e^{-\frac{n\Delta t}{\tau}} + \vec{F}_{nodes} \right], \tag{3.3}
\end{aligned}$$

where K_c is the assembly of element stiffness matrix $K_{c_e} = V_e B_e^T D B_e$ for the spring E_1 , with D (which is the same as D_1) describing the relationship between the stress and the strain in three dimensions relevant to E_1 and the Poisson's ratio, B' is the assembly of $B_e^T V_e$, with B_e and V_e being the matrix of the derivative of the shape function and the volume of the element, respectively, K_{inst}^{n+1} is the assembly of the instantaneous element stiffness matrix, i.e.,

$$K_{inst_e}^{n+1} = \left(1 + \frac{\alpha(1 - e^{-\frac{n\Delta t}{\tau}})}{n\Delta t/\tau} \right) K_c,$$

and \vec{F}_{nodes} is the nodal force, i.e.,

$$\vec{F}_{nodes} = \sum_{e=1}^m \left(\iiint_{V_e} N^T \vec{f}^{n+1} dV + \iint_S N^T \vec{\Phi}^{n+1} dS + \vec{P}_i \right)$$

Since the streptavidin-coated beads are bound to the collagen fibers and experience magnetic forces, their impact on the ECM can be considered as point forces \vec{P}_i , as is illustrated in Figure 3.3, where the arrangement of the beads and magnetic forces \vec{P} mimics the conditions in the stretch-test experiment. In the experiment, the ECM is subjected to two groups of point forces pointing outwards (and perpendicular to its length) in opposite directions. Figure 3.4a shows the von Mises stress while Figure 3.4b shows the deformation of the ECM sample in the z direction. From these figures, it can be observed that larger stress is generated around the beads. The combined influence of the beads results in the contraction of the ECM in the negative z -direction.

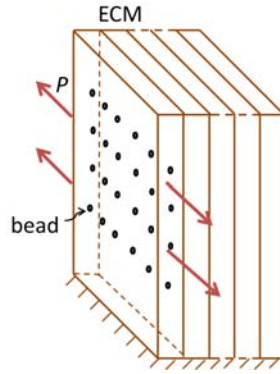


Figure 3.3: Model of the ECM sample with point loads due to the virtual beads.

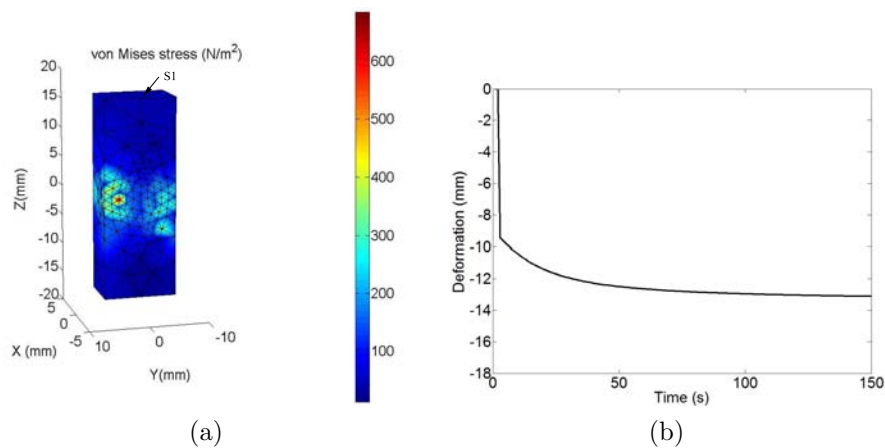


Figure 3.4: (a) von Mises stress generated in the ECM, and (b) the z -directional deformation of the top surface (S1) of the ECM.

3.3.2 Determination of apparent stiffness of modified ECM under the influence of an external magnetic field

Let E_{pure} , E_{bead} , and E_{mod} denote the Young's modulus of the pure ECM, the modified ECM in the absence of the magnetic field, and the modified ECM in the presence of the magnetic field, respectively. The analytical model developed in Section 3.3.1 is now applied to determine E_{mod} based on E_{pure} , E_{bead} , and the magnetic force acting on the beads due to the magnetic field. This magnetic force is generated by a pair of magnets (described later in Section 3.4.3), and its magnitude is computed based on the approach presented in [113]. In the analytical model, the effect of the external magnetic field on the ECM is accounted for in terms of the point forces generated by the (virtual) beads in the ECM. In this context, the stiffness of a modified ECM sample under the influence of an external magnetic field can be expressed as the sum of the following two terms:

- (i) the apparent stiffness of the pure ECM subjected to the pre-tension induced by the point forces representing the magnetic forces acting on the beads (denoted by E_{point}), and
- (ii) the *increase* in the Young's modulus of the ECM solely (i.e., without the magnetic field) due to the presence of the magnetic beads (denoted by ΔE_{bead}); that is, $\Delta E_{\text{bead}} = E_{\text{bead}} - E_{\text{pure}}$.

therefore,

$$E_{\text{mod}} = E_{\text{point}} + \Delta E_{\text{bead}} \quad (3.4)$$

The term E_{point} (due to the pre-tension in the pure ECM) can be determined as follows. Firstly the pre-tension was calculated using Equation (3.3), based on the magnetic forces exerted in the ECM through the beads and the stiffness of the pure ECM. Specifically, K_c and K_{inst} in Equation (3.3) are obtained, using Equation (3.4), from the stiffness of the pure ECM, which is determined by experiment as described later in Section 3.5.1, while \vec{F}_{nodes} takes on the values of the magnetic forces. In this case, the beads are considered “virtual” in the sense that the modified ECM is

constitutively the same as the pure ECM — other than the existence of the “virtual” point loads when the magnetic field is present. The portion of force required to overcome this pre-tension is then calculated and added to the force that is needed to deform the pure ECM for a given deformation, leading to the total force required to produce that deformation in the modified ECM in the presence of a magnetic field.

Figure 3.5 shows the total forces required to deform the ECM at a constant rate of 10 mm/min in the presence of the magnetic field for different concentrations of beads. For the pure ECM, this force increases linearly under a constant rate of elongation. By contrast, for the ECM with beads exposed to the magnetic field, this force increases exponentially under the same rate of elongation. It can be also seen that a greater force is required to deform the ECM with beads exposed to the magnetic field as compared to the case of pure ECM. Moreover, the increase in bead concentration is associated with the growth of the force. The reason is that the increase in bead concentration causes a larger pre-tension that resists ECM deformation.

Now the term E_{point} in Equation (3.4) can be calculated by linearizing the force-deformation curves after the transition point as shown in Figure 3.5. The region before this transition point is the creep region commonly found in viscoelastic deformation. The slope of the curve after the transition point is used to determine E_{point} [114] [2]. To obtain E_{mod} , ΔE_{bead} is then calculated based on E_{bead} and E_{pure} , which are obtained from the experiments (discussed in Section 5). Table 3.1 shows the values of E_{mod} thus obtained for two types of ECM samples with different bead concentrations. It can be seen that increasing the concentration of beads from 0.1 mg/ml to 0.5 mg/ml leads to a significant increase in the apparent stiffness of the modified ECM. Comparison between results from numerical simulation (using the analytical model) and that obtained experimentally is presented in Section 3.5.5.

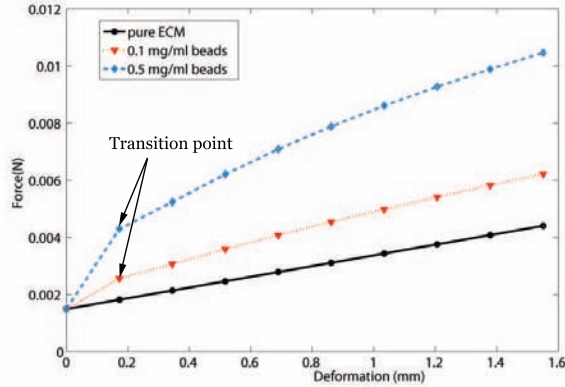


Figure 3.5: Force-deformation relationships for three types of ECM, i.e., pure ECM, ECM with beads at a concentration of 0.1 mg/ml and 0.5 mg/ml. The ECM with beads are exposed to an external magnetic field created by a pair of permanent magnets.

Table 3.1: Apparent stiffness of modified ECM exposed to an external magnetic field, obtained from numerical simulation.

Bead concentration (mg/ml)	Apparent stiffness (N/mm)
0.1	0.0053
0.5	0.0103

3.4 Experiment

Magnetic beads were embedded in the ECM and evaluated its apparent stiffness empirically. The stiffness evaluation involved three types of ECM samples: (i) pure ECM without any beads, (ii) ECM embedded with beads that were bio-conjugated with the collagen fibers, and (iii) ECM embedded with beads that were *not* bound to the collagen fibers.

3.4.1 Embedding beads in ECM

To embed beads in the ECM with bio-conjugation, magnetic beads were prepared with a coating having a good affinity with the collagen fibers to form a strong attachment. Beads coated with streptavidin were used since

streptavidin will affix to areas dense with collagen. Streptavidin contains an Arg-Tyr-Asp (RYD) amino acid sequence that mimics the Arg-Gly-Asp (RGD) receptor domain of fibronectin [115]. This form of bio-conjugation involves four types of bonding, namely, hydrophobic, van der Waals, hydrogen bonding network, and covalent bonds. The complementary shapes, charges, polarity, and hydrophobicity of the streptavidin and the collagen fibers permit multiple weak interactions which in combination produce a tight binding [116] [117].

To embed beads in the ECM such that there is no binding between the beads and the collagen fibers, Polyethylene glycol (PEG) coated beads were used. Due to its hydrophilicity, this coating prevents bio-conjugation from occurring between the collagen fibres and the beads. PEG coating is done on the amine coated beads so that it creates an inert coating around the beads. The PEG structure contains hydrogen bonded to water molecules that results in a hydration layer, which makes bonds between the PEG coated beads and the collagen fibres difficult to form since this layer must be disrupted for any form of bio-conjugation to occur. The detailed procedure is described in Appendix 1.

3.4.2 Preparation of samples

The collagen was prepared according to the recipes listed in Table 5.1. All of the samples contain 2.0 mg/ml of Rat Tail Collagen Type 1, obtained from BD Biosciences. The streptavidin-coated magnetic beads, BM551, were procured from Bangs Laboratory. To enable conjugation of Polyethylene glycol (PEG) to the magnetic beads requires beads with an amine functional end group. The amine-coated magnetic beads, BM546, were procured from Bangs Laboratory and the PEG (at 3400 g/mol) was procured from Sigma Aldrich. Two groups of samples were prepared: one with magnetic beads and one without. For samples with magnetic beads, two different concentrations, i.e., 0.1 mg/ml and 0.5 mg/ml, of the beads were added (as indicated in Table 5.1). A PTFE mold with a through hole and a base was fabricated and used to contain the liquid collagen until gellation occurred. The dimensions of this mold are shown in Figure 3.6.

The collagen (or the collagen with beads mixture) was thoroughly vortexed for two minutes until a homogeneous solution was formed and all the components of the mixture were spread throughout the entire volume. The mixture was then pipetted into the mold carefully so that no visible air cavities were formed. Fibrillogenesis was usually done in an external incubator at 37°C and 5% CO_2 . To achieve self-assembly of collagen molecules into fibers and binding of beads to the collagen fibers, the samples were placed in an incubator for at least 22 hours to ensure that gellation occurred throughout the entire collagen strip.

Table 3.2: Recipes for collagen preparation.

Components	Without magnetic beads	With magnetic beads (0.1 mg/ml) (Streptavidin coated)	With magnetic prbeads (0.5 mg/ml) (Streptavidin coated)	With magnetic beads (0.5 mg/ml) (PEG-coated)
Collagen (4.62 mg/ml)	1.593 ml	0.1.593 ml	1.593 ml	1.593 ml
Water	1.089 ml	1.024 ml	0.764 ml	0.764 ml
PBS (10x)	0.325 ml	0.325 ml	0.325 ml	0.325 ml
NAOH (0.5 N)	0.244 ml	0.244 ml	0.244 ml	0.244 ml
Beads (5 mg/ml)	0 ml	0.065 ml	0.325 ml	0.325 ml
Total	3.250 ml	3.250 ml	3.250 ml	3.250 ml

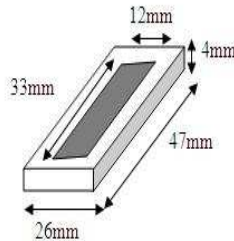


Figure 3.6: Teflon mold for collagen formation.

3.4.3 Experimental setup and procedure

The stiffness of the ECM was evaluated by a stretch test using an Instron 8848 micro-force tester. The micro-force tester has a load cell rated at 10 N with a 0.001 N resolution.

Stretch tests were carried out on ECM samples at the fixed rate of 10 mm/min. While performing the stretch tests, a certain portion of the sample was exposed to a static magnetic field produced by a permanent magnet, as is depicted in Figure 3.7. This permanent magnet is made of an alloy of neodymium, iron and boron (NdFeB) and it is capable of producing a magnetic field of 0.2T. Two magnets form an aligned configuration such that the ECM sample is located between the magnets with a gap of 1.5 cm from each magnet. This leads to the creation of restoring forces on the beads when they are dislocated from their original positions (when the ECM sample is in its un-stretched state) by the stretching action.

The introduction of the magnetic field thus creates a region of higher stiffness in the ECM such that a larger force is required to produce a given deformation (i.e., elongation, in this case) compared to the amount of force required to produce the same deformation in the absence of the magnetic field. The stretch tests were carried out until the ECM ruptures. The force applied on, and the extension of, the ECM were recorded during the test.

Eight sets of tests (involving four ECM samples in each set) were conducted under the conditions summarized in Table 3.3. The first two sets involve ECM samples without any beads embedded (i.e., pure ECM samples). These two sets of tests were designed to demonstrate that the magnetic field alone does not affect the stiffness of a pure ECM, and to establish a basis on the stiffness of the pure ECM for comparison with the results from the other four sets of tests. The next four sets (i.e., Sets 3–6) investigate the effect of the external magnetic field on the stiffness of the modified ECM. Finally, Sets 7 and 8 examine the effect of the presence of the beads (in the ECM but without any bio-conjugation between the beads and the collagen fibers) on the ECM stiffness.

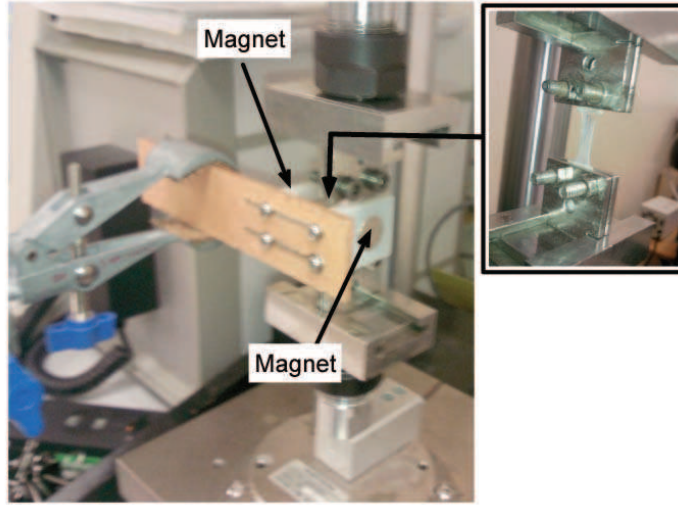


Figure 3.7: Experiment Setup. The stiffness of the ECM was evaluated by a stretch test using an Instron 8848 micro-force tester. The micro-force tester has a load cell rated at 10 N with a 0.001 N resolution.

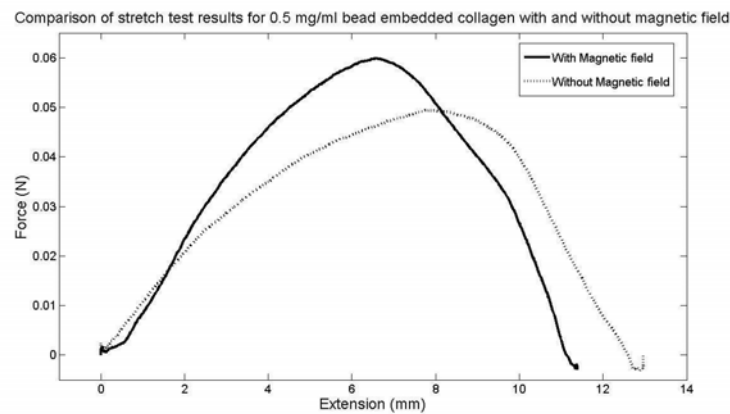
Table 3.3: Test scenarios. Each set involves four ECM samples.

Set No.	Bead concentration	Magnetic field
1	0	off
2	0	on
3	0.1 mg/ml	off
4	0.1 mg/ml	on
5	0.5 mg/ml	off
6	0.5 mg/ml	on
7	0.5 mg/ml PEG Coated	off
8	0.5 mg/ml PEG Coated	on

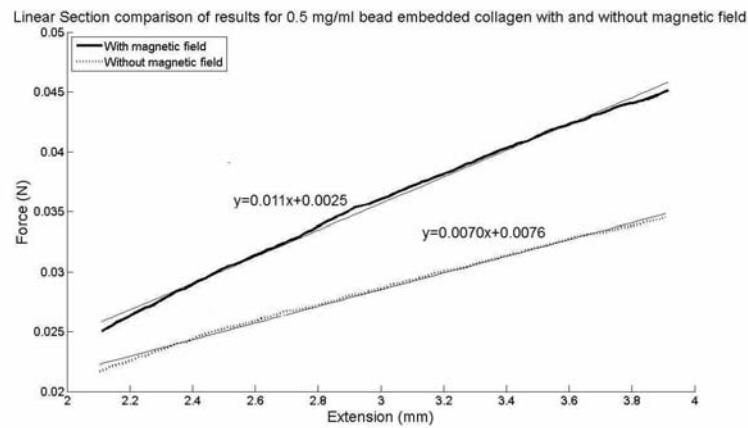
3.4.4 Data processing

The full stretch graph from one sample is shown in Figure 3.8a. Figure 3.8b shows the linear section of the curve that is used to determine the stiffness of the pure collagen sample. There is a clear distinction of the two set of curves in the elastic region before sample rupture occurs as shown

in Figure 3.8. It can be observed from Figure 3.8b that the sample under the influence of the magnetic field exhibits a steeper slope than the sample without a magnetic field. The graphs of each of the stretch tests were plotted and the gradient of the linear section of each graph was extracted. The mean was obtained from the four samples in each set, as shown in Figure 3.10.



(a)



(b)

Figure 3.8: (a) Stretch test result of a sample embedded with beads at a concentration of 0.5 mg/ml and in the presence (solid curve) and absence (dotted curve) of a magnetic field. (b) Linear sections of the graphs taken to estimate the stiffness of two samples.

3.5 Results and discussion

3.5.1 Determination of pure ECM stiffness

The stiffness of pure ECM is obtained from linear-fitting of the force-deformation curve of pure ECM generated from experimental data. The parameter E_1 in the SLSM model (shown in Figure 3.2) determines the steady-state deformation of the ECM under external forces, while E_2 is only relevant to the rate of approaching the steady deformation. Here E_2 is randomly chosen to be 500 Pa in the simulation as it has negligible impact on the result concerning the change in ECM stiffness. The parameters E_1 and η were obtained by linear-fitting of the force-deformation curves shown in Figure 3.9, which were obtained experimentally. The thick straight line in the figure is the result of the linear-fitting, whose slope is the stiffness of the pure ECM, while the initial offset is related to the viscosity of the pure ECM. Based on this stiffness, the Young's modulus of the pure ECM $E_{\text{pure}} \equiv E_1$ is calculated from $E_{\text{pure}} = kL/A$, with the stiffness $k = 0.003$ N/mm, the cross-sectional area of the ECM $A = 48$ mm², and the length of the ECM $L = 28$ mm. (In the experiment the original length of the ECM samples was 33 mm. With the two ends of the sample clamped by the micro-force tester, the effective length of the ECM was thus reduced by 5 mm.) The Young's modulus E_{pure} is calculated to be 1750 Pa. The offset z in Figure 3.9 is used to calculate the viscosity η of the ECM based on the equation $\eta = zL/(A\dot{\epsilon})$, with $z = 0.0023$ N and the deforming rate $\dot{\epsilon} = 10$ mm/min (which is the rate used in the experiment). The viscosity of the ECM is calculated to be 134 Pa·min.

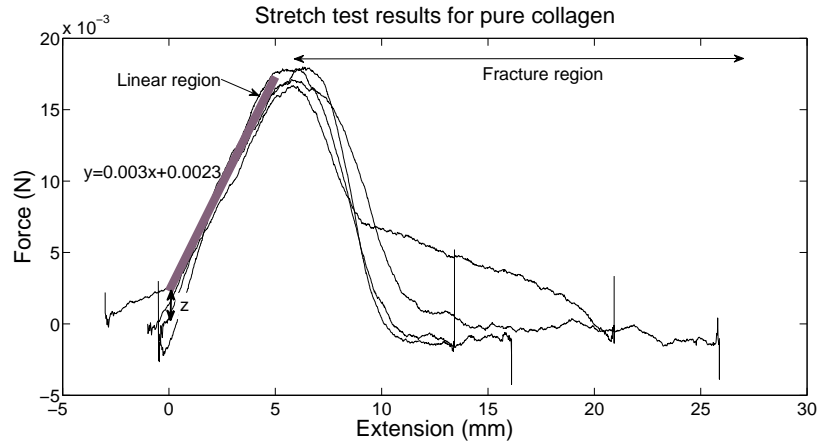


Figure 3.9: Force-deformation relationship of pure ECM samples.

3.5.2 Change in stiffness of modified ECM induced by the external magnetic field

Figure 3.10 shows the results of the eight sets of tests done on a total of 32 ECM samples. Cross-test comparison provides direct quantification of the effect of (i) the bio-conjugated beads, (ii) the bio-conjugation, and (iii) the external magnetic field, on the uniaxial stiffness of the ECM samples, as summarized in Table 3.4.

Comparison of results from Set 1 and Set 2 reveals that the pure ECM samples exhibit similar stiffness, regardless of whether the magnetic field was on or off. As is shown in Table 3.4, the average stiffness of pure collagen with and without the magnetic field differs by 5×10^{-4} in magnitude. The unpaired t -test shows that the two-tailed P value equals 0.5718; this difference is considered to be not statistically significant. It can therefore be concluded that the magnetic field had no significant effect on the stiffness of the pure ECM samples, and that the differences among the force-displacement relationships of the eight samples (in this set) were due to sample variations attributed to the repeatability of the ECM preparation process. The average slope of the linear approximation of the force-displacement relationship (calculated from data of Set 1 and Set 2) is 3×10^{-3} N/mm.

The effect of the mere presence of bio-conjugated beads in a ECM sam-

ple can be studied by comparing the results of Set 1 and Set 3. It can be seen, from both Figure 3.10 and Table 3.4, that embedding beads in a pure ECM sample (in the absence of an external magnetic field) slightly increases its uniaxial stiffness. The moving average line (dotted line) shown in Figure 3.10 shows the increase in stiffness of the ECM when the concentration of streptavidin beads was increased and when a magnetic field was present.

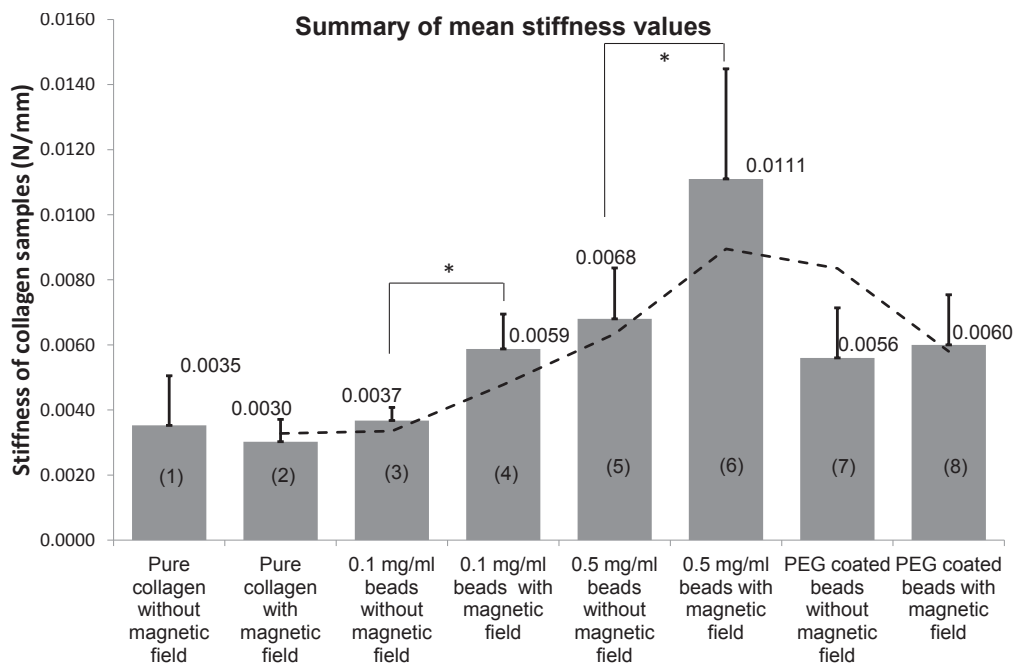


Figure 3.10: Summary of results from experiments.

To examine how an external magnetic field may affect the uniaxial stiffness of modified ECM samples, the results were compared from Set 5 and Set 6. It can be observed that there is a significant increase in the stiffness when the magnetic field is in effect. Similar conclusion can be drawn for the case involving Set 3 and Set 4, where the beads are at a lower concentration.

The case where the embedded beads are not bound to the ECM fibers was investigated next. To see the effect (if any) of such no-binding beads on the stiffness of the ECM, stretch test results are obtained from experiments Set 7 and Set 8. From Figure 3.10 and Table 3.4, it can be seen that the

Table 3.4: Summary of two-tailed P values from unpaired t tests and difference in magnitude of the mean values of stiffness. The numbers in brackets have the same meanings as those labeled on the bars in Figure 3.10; the top number in each entry indicates the P value while the bottom number indicates the difference in the mean value of stiffness.

	(1)	(3)	(5)	(7)
(2)	0.5718			
	5×10^{-4}			
(3)	0.8084			
	2×10^{-4}			
(4)		0.0085		
		2.2×10^{-3}		
(5)	0.0234			
	3.3×10^{-3}			
(6)			0.0605	
			4.3×10^{-3}	
(8)				0.7259
				4×10^{-4}

stiffness of the ECM samples embedded with non-binding beads (i.e., beads coated with PEG) is significantly lower than that of the samples with beads coated with streptavidin (and thus bio-conjugated to the ECM fibers). This is expected since the beads not bound to the ECM fibers offer, when under the influence of the external magnetic field, much weaker resistance against the dislocation of the fibers during ECM deformation.

3.5.3 Stiffness of ECM with streptavidin-coated magnetic beads

Figure 3.10 and Table 3.4 indicate that the external magnetic field produced significant changes in the stiffness of the modified ECM. Specifically, the

increase is 63% in the case of Set 6 (i.e., from 0.0068 N/mm to 0.0111 N/mm). A similar observation can be made for Set 4, which shows an increase in stiffness of 59% (i.e., from 0.0037 N/mm to 0.0059 N/mm). Furthermore the stiffness of the modified ECM with a lower concentration of beads is very close to that of the pure collagen when the magnetic field is off (i.e., Set 3 and Set 1). This clearly indicates that embedding beads at a low concentration alone will not significantly alter the mechanical properties of the modified ECM; the change in stiffness becomes significant only when an external magnetic field is applied.

3.5.4 Stiffness of ECM with PEG coated magnetic beads

For Set 7 and Set 8, the change in stiffness of 7% (i.e., from 0.0056 N/mm to 0.0060 N/mm) is not as significant compared to an increase of 63% for the case of Set 5 and Set 6. This indicates that the binding between the beads and collagen fibers indeed plays a significant role in altering the overall stiffness of the ECM when a magnetic field is applied. Such binding enables the collagen fibrils to attach to the beads strongly, resulting in a greater resistance to deformation in the fibers when an external magnetic field generates magnetic forces that oppose the movement of the beads.

3.5.5 Comparison of ECM apparent stiffness obtained from simulation and experiment

Table 3.5 shows the values of the Young's modulus of the modified ECM obtained from the model presented in Section 3.3 and from the experiments. It can be seen that the analytical results are in close agreement with that obtained from the experiments.

Table 3.5: Comparison of Young’s modulus of modified ECM.

Bead concentration (mg/ml)	Simulation	Experimental (Streptavidin-coated)
0.1	0.0053	0.0059
0.5	0.0103	0.0111

3.6 Concluding remarks

By analytical modeling and experiment it was demonstrated that the uniaxial stiffness of the ECM can be altered actively to a significant degree by embedding (in the ECM) magnetic beads that are bio-conjugated with the collagen fibers and applying an external magnetic field. The experimental results point to the possibility of creating desired stiffness gradients in an *in vitro* extracellular matrix to influence various cell behavior, such as proliferation, differentiation and apoptosis. The exertion of such influence can be interpreted in the context of the force-bearing interaction between cells and the collagen fibers.

3.6.1 Utility of the proposed ECM deformation model

In Section 3.3, a new model was proposed for describing the viscoelastic behavior of the modified ECM. Specifically, it was shown that the Young’s modulus of the modified ECM under the influence of an external magnetic field can be determined analytically based on E_{pure} , E_{bead} , and the magnetic force acting on the beads due to the magnetic field. The advantage of having this model is that it enables the determination of the stiffness of a modified ECM sample corresponding to a given external magnetic field without having to conduct a stretch test on the sample involving the instrumentation for the generation of that specific external magnetic field. This is particularly useful in an application where the stiffness of the modified ECM is being actively manipulated by dynamically varying the strength of the external magnetic field. In such a case, the model offers an efficient way to determine the *instantaneous* value of the Young’s modulus of the

modified ECM.

3.6.2 Implication of the proposed method for active manipulation of ECM stiffness

Application of an external magnetic field on a modified ECM sample creates a pre-tension in the collagen fibers. When a traction force acting in the direction opposite to the magnetic force is exerted on the fibers by a cell, the fibers exhibit a greater resistance to deformation, as is illustrated in Figure 3.11 .

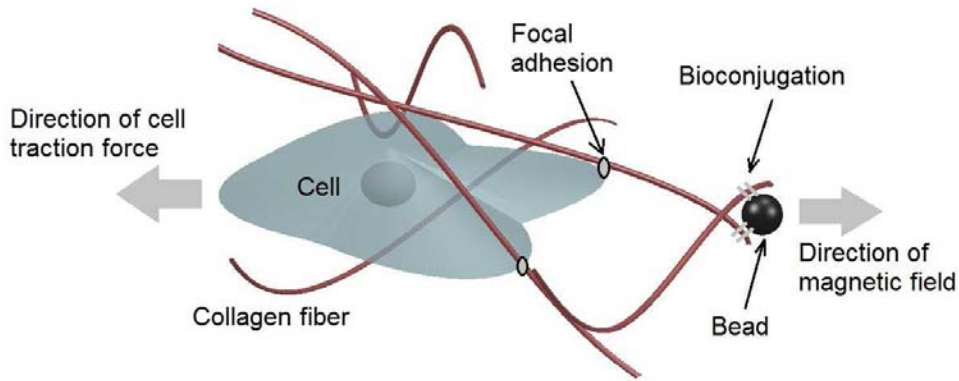


Figure 3.11: Schematic illustration of bead-embedded ECM and interaction between collagen fibers and cells via focus adhesion under the influence of an external magnetic field.

Due to this increased resistance to deformation in the fibers, cells will experience a greater stiffness in regions of the ECM where beads are present, which in turn may affect the cell behavior, such as cell migration. This stiffness sensed by the cells is known as the *apparent local stiffness* of the ECM at those sites, since this externally and mechanically induced change in the local deformability of the collagen fibers is only apparent to a cell near the site of an embedded bead and is localized at that site, while the global intrinsic material properties of the ECM remain unchanged. The advantage of this approach is that the stiffness of the ECM can be manipulated directly in real-time without significantly changing the *in vitro*

environmental conditions (such as temperature or pH value) for a cell.

A number of attempts have been reported in an effort to make practical this approach for active manipulation of ECM stiffness. A pure computational and simulation-based study on the stiffness of the modified ECM was reported in [118]; it uses a conceptual model constructed by calculating the total stress directly from the strain, which is less efficient than the method used in this chapter. Another work focuses on the microscopic stiffness of the ECM in the vicinity of a magnetic bead [119]. Although there is generally a similarity between micro-scale and macro-scale stiffness for stiffer materials, such a similarity does not apply to soft biological materials. The stiffness of soft materials vary significantly when measured in micro- and macro-scale, due to their heterogeneous structures. (The work presented in this chapter concerns only macro-scale measurements.) Lastly, the effect of the induced change in stiffness of the modified ECM on the behaviour of angiogenic sprouting was reported in [120].

While all these works mentioned above yielded useful insight on the mechanical behavior of the modified ECM and how that behavior may influence certain biological behavior of endothelial cells, they remain preliminary and various issues remain to be investigated. First, the effect of a number of variables on the stiffness of the modified ECM remains to be explored; these variables include bead concentration, size and placement of the magnets and their distance to the ECM sample, and strength of the magnetic field, etc. Second, the experiments described in this chapter only concern manipulation of ECM stiffness along a single axis. To study how ECM stiffness affects cell behavior *in vitro* requires the ability to manipulate the stiffness gradient in 3D. Third, although magnetic beads have been used in many applications (both *in vivo* and *in vitro*), their effect on the actual biological behaviour of cells are not yet fully understood. This is particularly true when an ensemble of beads are embedded in the ECM via bio-conjugation. It may be argued (based on available experimental results, e.g., [121] [122] [123]) that the bio-compatibility and toxicity of these magnetic beads with respect to its biological environment solely depends on the surface coating that is adhered to the magnetic particle, it is essential to verify that such an ensemble of beads do not directly interfere with

the natural behaviour of cells.

Chapter 4

Evaluating the change in micro scale stiffness of modified ECM

4.1 Introduction

The previous chapter showed the possibility of changing the macroscale uniaxial stiffness of magnetic bead embedded ECM by applying magnetic fields orthogonal to the stretching direction. In this chapter the approach to change the stiffness of ECM is verified by investigating the local microscale stiffness changes in the ECM.

Significant changes in cell behaviours due to variation in the physical properties of local areas of ECM where cell-ECM interactions occur have been observed [12] [15]. Although the exact mechanism involved in the interactions between a cell and the stiffness of its pericellular environment is not yet fully understood, it is generally accepted that the mechanical properties of the ECM influence cellular interactions at various levels, including protein expression [101]. One such mechanical property is the stiffness of the ECM, which has been observed to regulate the degree of cell-matrix adhesion, the size of focal adhesion, as well as the stiffness and tension developed by the cell itself [17] [99]. Cell motility and polarity are also associated with ECM stiffness, manifested in the tendency of cells to migrate from softer to stiffer environment [100].

There are methods for altering the stiffness of the ECM in order to observe

(*in vitro*) cell behaviour under various stiffness conditions. These methods rely on manipulating soluble cues, such as by changing the collagen concentration [90], varying the pH value in the ECM sample [5], or changing the polymerisation temperature of the ECM [4]. One factor that limits the applicability of these methods is that the change in stiffness realized by these methods is permanent and irreversible. Furthermore, some of these methods (such as that involving changing collagen concentration) alter the chemical composition of the ECM, leading to inconsistencies when comparing the observed cell behaviour under different stiffness conditions.

Manipulating the stiffness of ECM by mechanical means offers an alternative to those methods that rely on soluble cues. A novel approach was proposed where the stiffness of the ECM is altered by mechanically manipulating the deformability of the collagen fibers in the ECM [124]. The approach works by embedding magnetic beads in the ECM through bioconjugation between the streptavidin-coated beads and the collagen fibers, then applying an external magnetic field on the ECM to exert a magnetic force on the beads. This magnetic force, when applied statically, creates a pre-tension in the collagen fibers. When a traction force opposing the magnetic force is exerted on the fibers by a cell, the fibers exhibit a greater resistance to deformation, as is illustrated in Figure 4.1.

Due to this increased resistance to deformation in the fibers, cells will experience a greater stiffness in regions of ECM where magnetic beads are present, which in turn may affect the cell behavior, such as cell migration [87]. This stiffness sensed by the cells is referred to as the *apparent local stiffness* of the ECM at those sites, since this externally and mechanically induced change in the local deformability of the collagen fibers is only apparent to a cell at the pericellular level near the site of an embedded bead and is localized at that site, while the global intrinsic material properties of the ECM remain unchanged [125]. The advantage of this approach is that the stiffness of the ECM can be manipulated directly in real-time without significantly changing the *in vitro* environmental conditions (such as temperature or pH value) for a cell.

In this chapter, investigation was done on the effect of the presence of magnetic beads (when under the influence of an external magnetic field)

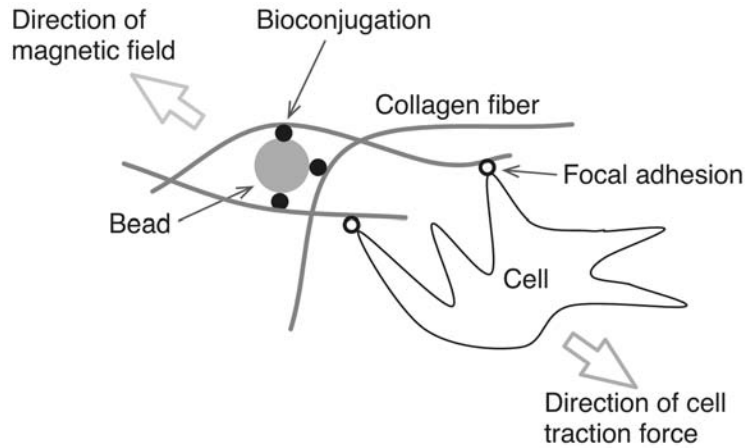


Figure 4.1: Schematic illustration of bead-embedded ECM and interaction between collagen fibers and cells via focus adhesions under the influence of an external magnetic field. This scenario provides the motivation for the work reported in this chapter on the determination of the change in the apparent local stiffness of the ECM under the influence of an external magnetic field.

on the *local* micro-scale stiffness of the ECM. This investigation focuses on determining the *change* in the apparent Young's modulus of the bead-embedded ECM when the external magnetic field is present (in comparison to the case when it is absent).

Since cellular behaviour is known to be influenced by the stiffness of the immediate surroundings of a cell, the ECM with which the cells interact must be characterized in order to develop a deeper understanding of the observed *in vivo* cell functions in a laboratory setting. An effective approach to obtain such a characterization is to study the mechanical deformation behavior of the ECM by indentation, using micro/nano-manipulation devices such as the atomic force microscope (AFM). Indenting a bio-material using an AFM in order to determine its Young's modulus is a well-known technique (e.g., [60] [61] [62] [63]). For soft hydrogels, indentation techniques are highly suitable for determining the mechanical properties of materials that may vary at micro- and nano-scale [126] [125]. In the work described in this chapter, this technique was adapted by using an AFM to indent ECM samples at locations in the vicinity of the magnetic beads.

The novelty in the adaptation of this technique manifests in the specific

arrangement of the magnetic field, the indentation direction, and the ECM sample in such a configuration that the indentation is resisted by the magnetic force. The indentation force exerted by the AFM on the ECM is thus transmitted to the beads to simulate the action of cell traction forces acting on the beads, while the presence of the external magnetic field induces a localized change in the resistance to deformation in the ECM. By applying the same prescribed force on a set of indentation sites individually, quantitative data was obtained reflecting the change in the local apparent stiffness of the ECM in the vicinity of beads solely due to the presence of the external magnetic field. Moreover, an analytical model was developed for predicting such changes, and verify that the prediction obtained by the model generally agrees with the experimental results.

The remainder of this chapter is organized as follows. Section 2 describes the method and materials used in the experiment. Section 3 describes the analytical model for predicting the change in ECM stiffness. Section 4 discusses the results obtained from the AFM indentation experiment, and compares the experimental results with the corresponding analytical prediction. Section 5 presents the conclusions.

4.2 Experimental design and implementation

4.2.1 Experimental design

An AFM is used to indent ECM samples to generate force and displacement data for estimating the value of the Young's modulus of the ECM. The tip of the cantilever probe of the AFM has a microsphere to generate three dimensional contact with the ECM embedded with magnetic beads. An external magnetic field is applied on the ECM during the indentation. This magnetic field is oriented such that the magnetic force acting on a bead is orthogonal to the direction of the indentation, as is illustrated in Figure 4.2.

The presence of an external magnetic field induces a pre-tension (i.e., a pre-tensile stress) in the ECM. When the indentation site is selected in such

a way that the pre-tension acts against the indentation, the deformation of ECM is reduced in the presence of a magnetic field compared to the case where the magnetic field is absent when an identical indentation force is applied. This reduction in deformation is localized at the indentation site, and corresponds to an increase in the stiffness of ECM therein. The force and displacement data thus collected by the AFM are then used to determine the *change* (due to the presence and absence of the magnetic field) in the Young's modulus of the ECM at the indentation site.

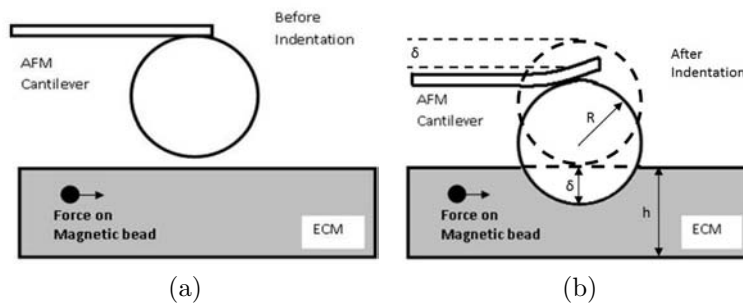


Figure 4.2: Schematic illustration of the proposed approach.

4.2.2 Embedding beads in ECM

To quantify the change in local ECM stiffness, four scenarios were investigated as listed in Table 4.1. The first two scenarios are for studying the effect of the magnetic field on the apparent stiffness of the ECM embedded with bioconjugated beads, while the last two are for studying the effect of the mere presence of non-bioconjugated beads on the ECM stiffness.

Table 4.1: Scenarios in experiment.

Scenario	1	2	3	4
Bioconjugation	yes	yes	no	no
Magnetic field	off	on	off	on

To embed beads in the ECM with bioconjugation, magnetic beads were prepared with a coating having a good affinity with the collagen fibers to form a strong attachment. Streptavidin contains an Arg-Tyr-Asp (RYD)

amino acid sequence that mimics the Arg-Gly-Asp (RGD) receptor domain of fibronectin, which enables streptavidin to affix to collagen-rich areas. The complementary shapes, charges, polarity, and hydrophobicity of the streptavidin and the collagen fibers permit multiple weak interactions which in combination produce a tight binding [115] [116] [117].

For Scenarios 3 and 4 (as listed in Table 4.1), non-bioconjugated beads were embedded into ECM such that there is no binding between beads and collagen fibers. For this purpose, Polyethylene glycol (PEG) coated beads were used because of its hydrophilicity. PEG coating was done on amine coated beads to create an inert coating around the beads. The PEG structure contains hydrogen bonded to water molecules that results in a hydration layer, which makes bonds between the PEG coated beads and the collagen fibres difficult to form since this layer must be disrupted for any form of bio-conjugation to occur. The detailed procedure for obtaining PEG coated beads is described in 2.

4.2.3 Preparation of samples

The collagen was prepared according to the recipes listed in Table 5.1. All samples contain 2.5 mg/ml of Rat Tail Collagen Type 1 from BD Biosciences. The streptavidin-coated magnetic beads, BM551, and amine coated beads, BM546, both with a diameter of 1.5 μm , were procured from Bangs Laboratory, Inc. For all cases, the samples have identical bead concentrations of 0.075 mg/ml.

The collagen-bead mixture was thoroughly vortexed for two minutes until a homogeneous solution was formed and the components of the mixture were spread throughout the entire volume. The mixture was then pipetted into a holder (discussed in Section 4.2.4 below) so that no visible air cavities were formed. Fibrillogenesis was done in an external incubator at 37°C and 5% CO₂. To achieve self-assembly of collagen molecules into fibers and binding of beads to the collagen fibers, the samples were placed in an incubator for at least 22 hours to ensure that gelation occurred throughout the entire collagen strip.

Table 4.2: Protocol for collagen preparation.

Components	Without magnetic beads	With streptavidin-coated magnetic beads	With PEG-coated magnetic beads
Collagen (4.62 mg/ml)	0.216 ml	0.216 ml	0.216 ml
Water	0.137 ml	0.131 ml	0.131 ml
PBS (10x)	0.040 ml	0.040 ml	0.040 ml
NAOH (0.5 N)	0.007 ml	0.007 ml	0.007 ml
Beads (5 mg/ml)	0 ml	0.006 ml	0.006 ml
Total	0.400 ml	0.400 ml	0.400 ml

4.2.4 Fabrication of magnet-collagen holder

For applying a magnetic field on the beads embedded in the ECM, a holder was designed to house the magnet and the collagen in close proximity to each other. The specifications of this holder are constrained by the physical configuration of the AFM and the operation of the magnet. These specifications are: (i) there should be a separate chamber to house the magnet, (ii) the wall between the magnet chamber and the cavity containing the collagen should be as thin as possible in order to maximize the magnetic force on the beads, and (iii) the sides of the holder should be filleted to achieve a height of 2 mm so that the clips on the alloy base of the AFM can be used to keep the holder in place.

A 4 mm cubic permanent magnet, made of N50 Grade Neodymium Iron Boron and procured from Liftonmagnet, was housed in this holder. This magnet is capable of generating approximately 6400G surface Gauss and 14500G residual induction (Br). Figure 4.3 shows a solid-model drawing of the holder and the actual item fabricated using an Eden 350 3D printer.

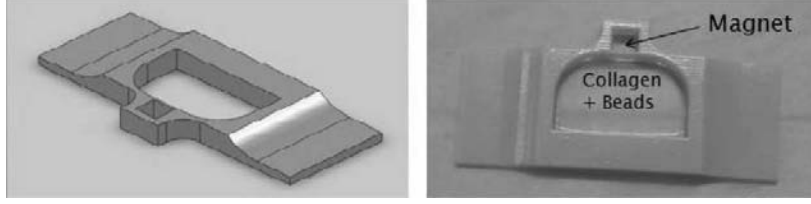


Figure 4.3: Solid model and actual holder.

4.2.5 Determining the Young's modulus of ECM samples by atomic force microscopy

The geometry of the AFM indenter influences how the Young's modulus can be calculated. A microsphere at the tip of the probe (i.e., the indenter) exerts minimal stress-strain concentration. It is assumed that the indenter is non-deformable and that there is no additional interactions between the indenter and the sample. With the approximation that the sample behaves as an isotropic and linear elastic solid occupying an infinitely extending half space, the Young's modulus of the sample can be calculated using the Hertz contact mechanics model [127]:

$$F = \lambda \delta^{3/2} \left(1 - \sum_{n=1}^4 (-1)^n \gamma^n - \frac{32\beta_0}{15\pi} \chi^3 + \frac{8\alpha_0\beta_0}{5\pi^2} \chi^4 \right), \quad (4.1)$$

where

$$\begin{aligned} \lambda &= \frac{4E\sqrt{R}}{3(1-\nu^2)}, & \gamma &= \frac{2\alpha_0}{\pi} \chi, & \chi &= \frac{\sqrt{R\delta}}{h}, \\ \alpha_0 &= (-1.2876 + 1.4678\nu - 1.3442\nu^2)/(1-\nu), \\ \beta_0 &= (0.6387 - 1.0277\nu + 1.5164\nu^2)/(1-\nu), \end{aligned}$$

with E being the Young's modulus of the sample, δ the indentation, h the sample height, R the radius of the microsphere, and ν the Poisson's ratio. For soft biological samples, it is common practice to use 0.5 for the value of ν [127].

The Hertz model may lead to significant error when applied to thin samples (i.e., small h) due to possible error in the estimation of the actual sample height [127]. There is an appropriate range of sample thickness and

indentation for any given tip radius for which the above formula is valid. As the parameter χ is increased with smaller sample thickness, the series expansion shown in equation 4.1 may lose accuracy. However such an error can be ignored in this experiment for the following reason. The height of the collagen gel used in this experiment is about $800 \mu\text{m}$. When compared to the depth of the indentation that is limited (by design) to a maximum of $5 \mu\text{m}$, the sample height h can be considered as infinitely large. Thus, with $\chi \rightarrow 0$, the force-indentation relationship, as shown in Equation (4.1), reduces to

$$F = \lambda \delta^{3/2}. \quad (4.2)$$

Consequently, by measuring F and δ experimentally, E for a given ECM sample can be estimated.

A JPK NanoWizard II AFM module, incorporated with a tip-scanning concept for long-time position stability, was used in conjunction with a microsphere (with a radius of $2.25\text{-}\mu\text{m}$) as the probe. The AFM is capable of exerting a force of 0.5 nN at an indenting speed of $1 \mu\text{m/s}$ and at a sampling rate of 2048 Hz . The force exerted and the resultant extension were used to determine the Young's modulus using Equation (4.2). Optical microscopy was also integrated with the AFM for image acquisition during the experiment. Figure 4.4a shows the AFM setup, while Figure 4.4b shows a close-up view of a typical indentation area.

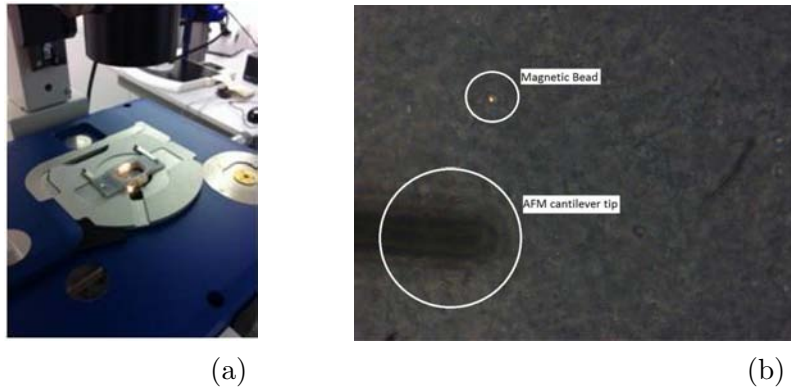


Figure 4.4: (a) AFM setup for experiment. (b) Close-up view of an indentation site.

To provide a basis for comparison, the Young’s modulus of a pure ECM sample was determined based on measurements taken at random points on the sample. The Young’s modulus thus obtained was 22.27 Pa.

4.2.6 Experimental procedure

The experiment was conducted for the four scenarios specified in Table 4.1 at selected indentation sites as illustrated in Figure 4.5. A set of force and indentation depth measurements were obtained along Line 1 in the y -direction, as shown in Figure 4.5. Another set of measurements were taken along Line 2, which was separated from Line 1 in the x -direction by about $50 \mu\text{m}$. Two reference points were chosen along each line and fifteen to twenty measurements were made. Each measurement was taken at a point located a few microns away from a nearest bead (and between that bead and the magnet) to ensure that there was a bead that generated the dominant resistance to the indentation. For each sample, two sets of measurements for each scenario were obtained at selected points located 4 mm away from the two lines.

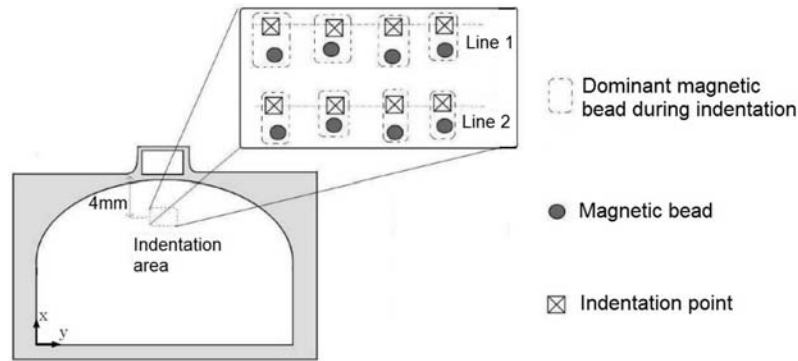


Figure 4.5: Detailed illustration of indentation areas and bead locations.

The results of the experiments are discussed later in Section 4, in conjunction with the analytical prediction obtained from the model presented in the next section.

4.3 Theoretical analysis of change in ECM stiffness

In this section the change in the Young's modulus of a ECM sample due to the effect of the external magnetic field acting on the beads embedded in the sample was analysed.

When exposed to a magnetic field, the magnetic beads bound to the collagen fibrils generate a pre-tension in the ECM. Since the ECM is confined on all sides except the top surface where indentation occurs, one consequence of this pre-tension manifests in a change in the height of the ECM (i.e., a deformation in the z -direction). This change in height is positive (i.e., an increase, with respect to the original height) for region closer to the magnet and negative for region further away from the magnet, as is illustrated in Figure 4.6(a).

Let $\hat{\delta}_p$ denote the total z -direction deformation of the ECM at a point p on that surface due to the pre-tension in the x -direction. Suppose that for a *pure* ECM sample that contains *no* beads a force F_0 is required to achieve a z -direction indentation of δ from the point p , and that for a ECM sample embedded with beads and under the influence of a magnetic field an indenting force F^* is required to achieve the same δ . In general F^* differs from F_0 due to the effect of the pre-tension. For instance, $F^* > F_0$ for the same δ when the deformation is positive (i.e., $\hat{\delta}_p > 0$), since an extra force of $\Delta F = F^* - F_0$ is required to overcome the effect of the pre-tension due to the magnetic forces. Figure 4.6(b) illustrates this situation.

ΔF (for all δ) is referred as the change in the indentation force due to the effect of the pre-tension. It reflects the change in the apparent stiffness of the ECM with respect to the point p . This change in the apparent stiffness is represented in terms of the change in the Young's modulus of the ECM as $\Delta E = E^* - E_0$, where E^* is the Young's modulus of the ECM embedded with beads and in the presence of the magnetic field, while E_0 is the Young's modulus of the pure ECM. An estimate E^* is required to predict ΔE .

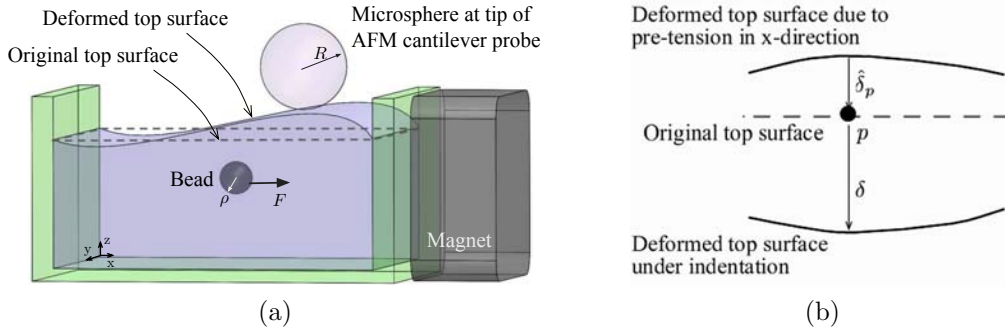


Figure 4.6: (a) ECM is deformed in the z -direction due to the pre-tension in the x -direction. (b) Deformation $\hat{\delta}_p$ of ECM region near the magnet in the z -direction due to pre-tension in the x -direction, and deformation δ due to indentation.

Section 4.3.1 presents an analytical method for determining $\hat{\delta}_p$, while Section 4.3.2 describes this approach for analytically estimating the new apparent Young's modulus E^* based on $\hat{\delta}_p$ and E_0 .

4.3.1 Deformation of ECM due to pre-tension

Consider an ECM sample embedded with N beads uniformly distributed therein. Let S denote the set of all points on the top surface of the ECM in the absence of any pre-tension. Let $\hat{\delta}_{p,j}$ denote the z -direction deformation at a point $p = (x_p, y_p, z_p) \in S$ due to the pre-tension generated by the magnetic force F_j acting on a single bead j located at a distance of d_x from the magnet and at a distance of $r_{j,p} = |\mathbf{r}_{j,p}|$ from p , as is illustrated in Figure 4.7. Summing up such deformations at p due to all N beads yields the total z -direction deformation at p due to the pre-tension in the x -direction, that is,

$$\hat{\delta}_p = \sum_{j=1}^N \hat{\delta}_{p,j}. \quad (4.3)$$

The approach proposed by Landau and Lifshitz [127] [128] was adopted to calculate $\hat{\delta}_{p,j}$. Consider a spherical bead j with radius ρ subjected to a force F_j that acts in the positive x -direction and is distributed over a contact circle of radius a_j . (The detailed steps for calculating F_j for the experiment setup described in Section 4.2 is presented in 3.) Assume that

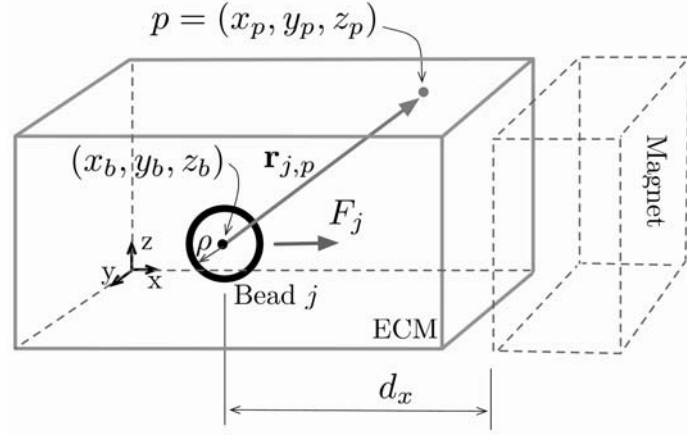


Figure 4.7: Schematic illustration of setting for calculating the deformation of ECM due to pre-tension in x -direction.

F_j is applied at the center of a semi-infinite solid, which coincides with the center of the bead at (x_b, y_b, z_b) , as shown in Figure 4.7. Then for a point $p \in S$, $\hat{\delta}_{p,j}$ can be expressed as

$$\hat{\delta}_{p,j} = \int \int P_x(a_j) G_{xz}(r_{j,p}) dA, \quad (4.4)$$

where $P_x(a_j)$ is the Hertz pressure field, $G_{xz}(r_{j,p})$ is the Green's function, and A is the contact region, i.e., $A = \pi a_j^2$. The Hertz pressure field generated by the bead j (due to F_j) is

$$P_x(a_j) = \frac{2E_0 a_j}{\pi \rho (1 - \nu^2)}, \quad (4.5)$$

where ν is the Poisson's ratio, and the contact radius a_j can be expressed as

$$a_j = \left(\frac{3F_j \rho (1 - \nu^2)}{4E_0} \right)^{1/3}. \quad (4.6)$$

The Green's function describes the displacement created in the z -direction by a force acting in the x -direction, and can be written as [129]

$$G_{xz}(r_{j,p}) = \frac{d_j(1 + \nu)(1 - 2\nu)}{2\pi E_0 r_{j,p}^2}, \quad (4.7)$$

where d_j is the length and direction of the x -axis component of the vector $\mathbf{r}_{j,p}$, i.e., $d_j = x_p - x_b$.

Using Equations (4.3)-(4.7), a numerical simulation in MATLAB[®] was conducted to determine $\hat{\delta}_p$ for an ECM sample (with a dimension of $25 \times 15 \times 0.8$ mm) used in the experiment as described in Section 4.2. The simulation involved a total of $N = 1.5 \times 10^6$ beads, distributed uniformly in 14 layers covering a physical depth of 0.8 mm in the z -direction, with each layer containing a 429×258 grid of beads over a physical dimension of $25 \text{ mm} \times 15 \text{ mm}$. The distance between any two adjacent beads in x , y , or z direction is approximately $60 \mu\text{m}$. A total of $429 \times 258 = 110,682$ points on the top layer were chosen in the calculation of $\hat{\delta}_p$. To ensure that the simulation was consistent with the actual indentation process (as described in Section 4.2.6), these points were purposely selected to be $5 \mu\text{m}$ away in the x -direction from a bead in the top layer located just beneath the top surface of the ECM, and in between that bead and the magnet.

Figure 4.8 shows the deformation $\hat{\delta}_p$ of the top surface of the ECM obtained from the numerical simulation. In this simulation, the magnet is located at $x = 0.015$ m. The value of $\hat{\delta}_p$ ranges from $-3 \mu\text{m}$ (at locations furthest from the magnet) to $2 \mu\text{m}$ (at locations near the magnet).

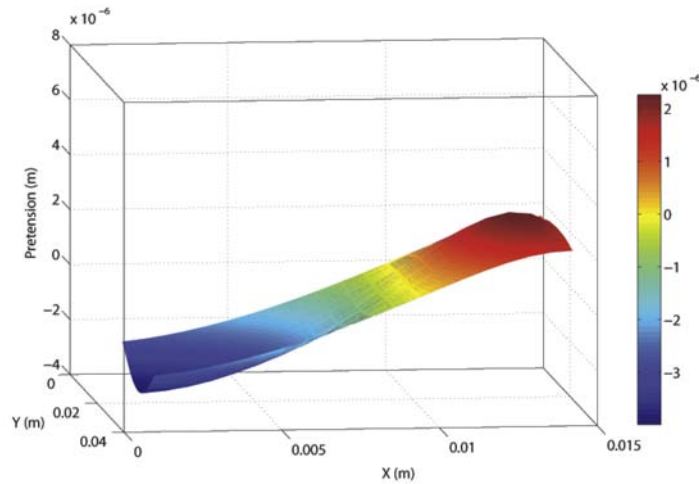


Figure 4.8: ECM deformation (due to magnetic forces acting on all embedded beads) obtained by numerical simulation.

4.3.2 Determination of change in Young's modulus by curve-fitting

Figure 4.8 shows that the deformation of the top surface of the ECM due to the x -direction pre-tension can be positive or negative. The case where deformation is positive will be focused in the subsequent analysis, i.e., $\hat{\delta}_p > 0$. The same approach, however, can be readily applied to the case where $\hat{\delta}_p < 0$, as is highlighted in the remark at the end of this section.

For a pure ECM sample, the force-deformation relationship as shown in Equation (4.2) is described by $F = \lambda_0 \delta^{3/2}$, where $\lambda_0 = \frac{4E_0\sqrt{R}}{3(1-\nu^2)}$. Consequently, for an ECM sample embedded with magnetic beads and under the influence of a magnetic field, the force-deformation relation can be expressed as

$$F = \lambda_0 \delta^{3/2} + \Delta F, \quad (4.8)$$

where ΔF is the extra force required to overcome $\hat{\delta}_p$ in order to achieve the same δ as in the case of pure ECM. Now imagine that the top surface is confined in the same way as all the other surfaces of the ECM, and hence is not allowed to deform upwards when under the x -direction pre-tension generated by the magnetic forces acting on the beads. This in effect leads to the pre-tension in the x -direction being transduced into an upward tension in the z -direction. This upward tension then acts against the indentation, leading to an increase in the indentation force F for the same indentation depth (as compared to the case of pure ECM). This force-deformation relationship can be defined by the new value of the Young's modulus E^* , and can be expressed as

$$F = \lambda^* \delta^{3/2}, \quad \text{with } \lambda^* = \frac{4E^*\sqrt{R}}{3(1-\nu^2)}. \quad (4.9)$$

The extra force ΔF can be calculated based on Equation (4.2) by replacing δ with $\hat{\delta}_p$, i.e., $\Delta F = \lambda_0 \hat{\delta}_p^{3/2}$. Since $\hat{\delta}_p$ depends on the configuration involving the ECM and the magnet and is independent of δ , for the experiment setup as described in Section 4.2 $\hat{\delta}_p$, and thus ΔF are considered to be fixed quantities with respect to a given point p in an indentation process where

$\delta \neq 0$.

For a given ECM-magnet configuration, the plot of Equation (4.8) can be obtained by shifting the plot of $F = \lambda_0 \delta^{3/2}$ upwards by a constant ΔF . This up-shifted plot can be readily generated for any given point $p \in S$, since λ_0 contains only known parameters, and $\hat{\delta}_p$ can be calculated by numerical simulation (as was presented in Section 4.3.1). By a curve-fitting process that yields a value for λ^* that minimizes the difference between the plots of Equation (4.8) and Equation (4.9) over a range of δ values (as is illustrated in Figure 4.9), the value of E^* can be estimated.

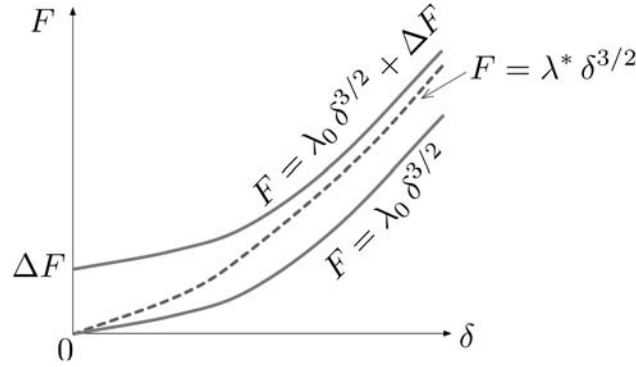


Figure 4.9: Determination of λ^* by curve-fitting.

The curve-fitting process is as follows. A set of δ values are chosen for which the corresponding values of F are determined by using Equation (4.8). The equation $F = \lambda^* \delta^{3/2}$ is then used to fit these F - δ value pairs using the Trust-Region-Reflective Least Square algorithm provided in MATLAB[®] to yield the optimal value for λ^* . The value of E^* is then calculated from the expression for λ^* in Equation (4.9).

Figure 4.10 shows the plots of Equation (4.9) with the optimal λ^* for the cases where the indenting points are 4 mm, 5 mm and 7 mm away from the magnet in the ECM-magnet configuration described in Section 4.2. The Young's modulus E^* for these three cases were calculated as 27.64 Pa, 25.51 Pa, and 23.91 Pa, respectively. Compared to $E_0 = 22$ Pa (which was experimentally determined as described in Section 4.2.5), the stiffness of the region of the ECM 4 mm away from the magnet is increased by 26%.

As the distance increases to 5 mm and 7 mm, the change in stiffness are 15.9% and 8%, respectively.

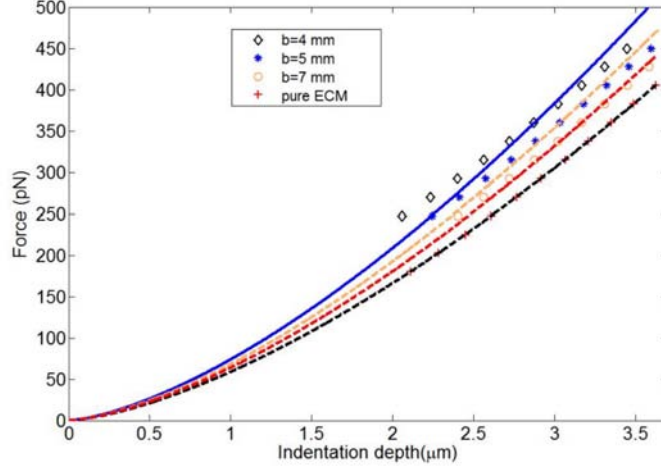


Figure 4.10: Plots of force F versus indentation depth δ at points 4 mm, 5 mm, and 7 mm away from the magnet for ECM embedded with magnetic beads, and for pure ECM.

Remark: The above curve-fitting approach was formulated based on the case where $\hat{\delta}_p > 0$. For the case where $\hat{\delta}_p < 0$, the same approach applies. The difference is that for this case the counterpart of Equation (4.8) becomes

$$F = \begin{cases} 0 & \text{for } \delta < |\hat{\delta}_p| \\ \lambda_0 \delta^{3/2} & \text{for } \delta \geq |\hat{\delta}_p|. \end{cases}$$

4.4 Results and discussion

4.4.1 Experimental results

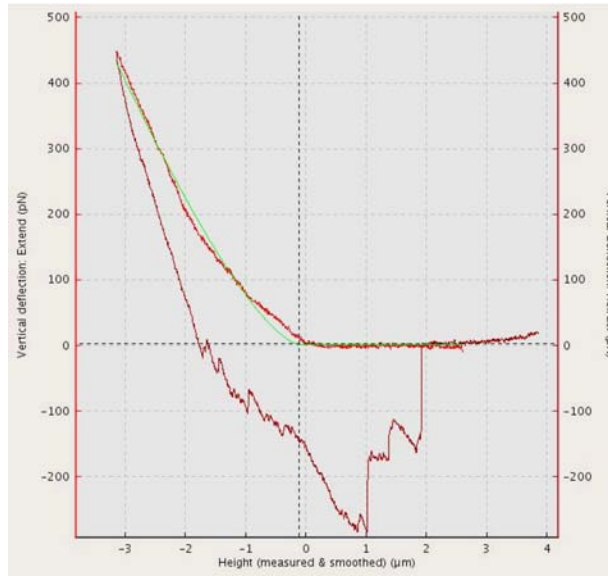
Figure 4.11 shows experimental results obtained at an indentation site of a sample embedded with streptavidin-coated beads. Two graphs show the relationship between the indentation force and the separation between the AFM cantilever tip and the ECM in the absence (Figure 4a) and the presence (Figure 4b) of the magnetic field. In each graph, the vertical axis

indicates the force registered by the AFM (due to cantilever deflection), while the horizontal axis represents the separation. The dark vertical dotted line separates the graph into a contact region (i.e., to the left of this line) and a non-contact region (to the right). A negative separation value in the contact region indicates the depth of the indentation.

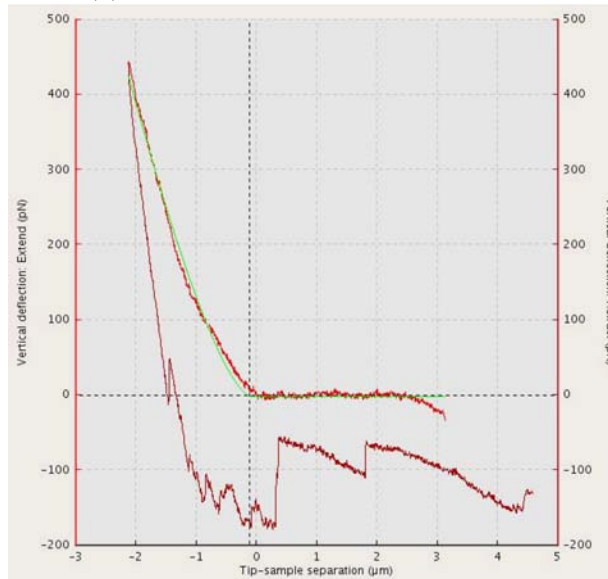
During an indentation experiment, the motion of the AFM cantilever tip consists of a downward motion pressing onto the sample, followed by a retracting motion away from the sample. The bright red curve (on the top) corresponds to the downward motion while the dark red curve (at the bottom) corresponds to the retraction. The Young's modulus was then determined by fitting the force and separation values collected during the downward motion using the Hertz model described by Equation (4.2). The green curve in both figures represents the result of the curve-fitting process, with a residual error RMS of 9.118 pN for the case in Figure 4a and 8.994 pN for Figure 4b. It can be seen from the graphs that (i) the indentation reached the common maximum force of 450 pN before the AFM tip retracted, and (ii) at this maximum force, the indentation depth of 2.1 μm for the case when the magnetic field was present was significantly smaller than the depth of 3.2 μm achieved when the magnetic field was absent.

The hysteresis reflected by the indentation and the retraction curves in the contact region of the graph is due to the viscous and plastic behaviour of the collagen. In the non-contact region, the noisy signal in the retraction curve reflects the movement of the cantilever as it retracts from the sample.

The average values of Young's modulus for Line 1 and Line 2 (as illustrated in Figure 4.5) were calculated for each sample using the force and separation data collected only during the indentation motion, and the average value associated with the line that gave the least standard deviation was chosen as the Young's modulus for that sample. A minimum of 15 stiffness values were taken for each sample. The same process was repeated for the sample embedded with PEG-coated beads.



(a) AFM result without magnetic field



(b) AFM result with magnetic field

Figure 4.11: Force vs tip-sample separation graphs (plotted using the JPK software) for the cases where the magnetic field is (a) absent and (b) present. Trace (red) and retrace (dark red) curve clearly show hysteresis due to the viscous and plastic behaviour of the collagen.

4.4.2 Data analysis

Variability was observed in the data obtained from the AFM indentation experiments. It can be attributed to microscopic gel inhomogeneities. The

ECM is highly porous, with gaps roughly 150 nm in size [127]. During an indentation, the spherical indenter of the AFM may indent over gaps on the ECM surface that consist mainly of water, or at the edges of the gaps (which are formed by collagen fibers), resulting in uncharacteristically high or low stiffness readings.

The data was analyzed, using the modified Thompson- τ test [130] [131], to remove the outliers as shown in Figure 4 in 4. The results are summarized in Figure 4.12 and Table 4.3, which show the average Young's modulus associated with the four scenarios listed earlier in Table 4.1.

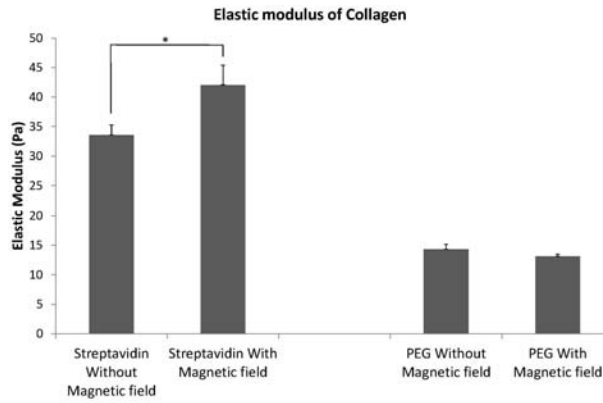


Figure 4.12: Stiffness values of samples embedded with streptavidin-coated beads and with PEG-coated beads.

Table 4.3: Summary of results.

Sample	Magnetic field	E (Pa)	Change in E
With streptavidin coated beads	off	33.59	
	on	42.06	25.21%
With PEG coated beads	off	14.32	
	on	13.13	-8.27%

4.4.3 Change in the stiffness of sample embedded with streptavidin-coated beads

From Table 4.3, it can be seen that there is an increase in the Young's modulus of 25.21% (in the ECM samples embedded with streptavidin-coated beads) around the region indented by the AFM when the magnetic field is applied. An unpaired- t test was conducted on the data for Scenario 1 and Scenario 2 to compare their respective average values of Young's modulus. The P value from this test is 0.0207, indicating that the difference by 25.21% in the average Young's modulus between these two sets of data is statistically significant. This provides direct evidence that the magnetic field affects the local stiffness of a sample embedded with streptavidin-coated beads.

4.4.4 Comparison of analytical and experimental results

According to the experimental results, the stiffness of the ECM at a location 4 mm away from the magnet is increased by 25.21% due to the magnetic field. This experimental result is comparable to the 26% increase predicted by the analysis (as presented in Section 4.3). This discrepancy reflects the difference between the indentation force calculated by the analysis and that determined by the AFM. There are three main causes for this difference.

The first is that the actual magnetic forces experienced by the beads in the ECM may differ significantly from those calculated using Equation (1) shown in Appendix 3, due to the fact that the percentage of magnetizable material (i.e., Fe_2O_3) in each bead varies because of manufacturing irregularities, whereas the analysis does not consider such variations.

The second cause is that the value of the Poisson's ratio used in the analysis may not reflect the actual value of that of the ECM used in the experiment. The value of $\nu = 0.5$ was used for the ECM samples in the analysis, under the common assumption of incompressibility due to their high water

content [127]. However it has been reported that the Poisson's ratio for collagen type I matrices may range from 0.15 to 0.48 [132].

The third cause concerns the structural characteristics of the ECM samples. The analysis considers the ECM samples to be uniform and non-porous, while the physical ECM samples are highly heterogenous (leading to variations in the readings from the AFM over the selected indentation sites).

4.4.5 Change in the stiffness of sample embedded with PEG-coated beads

From Table 4.3, it can be seen that the Young's modulus of the sample embedded with PEG-coated beads decreased by 8% upon the application of the magnetic field. This decrease can be explained by the fact that the PEG-coated beads had no strong attachment to the ECM fibers. When the magnetic force was applied, the individual beads were pulled and dislocated slightly from their original surrounding. This created space around a bead, making it less constricted so that, when the sample was indented by the AFM there was less resistance from the beads against the movement of the AFM tip, resulting in the observed reduction in the value of the Young's modulus.

It is also noted, from the experimental results, that the Young's modulus of samples embedded with PEG-coated beads in the absence of the magnetic field is less than that of pure collagen with no beads embedded (which was measured to be 22.27 Pa as reported at the start of this section). This can be explained by considering the fact that the PEG coated beads do not form any cross-linking sites with the collagen fibers, and so the number of cross links in such a sample would be lower than that in a pure collagen sample. Structural variation due to sample preparation may also play a role.

4.4.6 Relatively small changes in apparent stiffness at micro-scale level may amplify significantly at macro-scale level

Comparing the changes in stiffness obtained in these experiments conducted in micro-scale to results in the literature where ECM stiffness is measured in macro-scale [133] [134] [135], the results of 25% change (induced by the external magnetic field) in the local apparent stiffness of the ECM samples may seem less substantial. However, for highly structured heterogeneous materials such as ECM, it is important to note the differences when measuring the mechanical response of such materials at different length scales. It has been observed that, for soft biological material, the difference in stiffness at the micro-scale level may amplify with a factor as large 1000 at the macro-scale level [136]. Since the ECM (made of 2.5 mg/ml Rat Tail Collagen Type 1 from BD Biosciences) used in the work reported in this chapter has been shown to be very soft [137], it is therefore reasonable to expect that a change of 25% in the local apparent stiffness of such a material at the micro-scale level will in fact translate to a much larger change in the stiffness of the overall sample (i.e., at the macro-scale level). Furthermore, individual longer ranged protein polymers like collagen with water trapped within them will contribute to macroscopic tensile resistance. However, these effects will not be observed in indentation measurements since the indenter produces local microscopic sample deformations according to the indenter geometry and the depth of penetration. The local volume of water around the indenter therefore contributes very little to the resistance to deformation, as the tissue surrounding the indenter is under very little stress and is therefore capable of accommodating these small fluctuations in water content. A tensile measurement, on the other hand, stresses all the constituents of the tissue. Trapped water, which is incompressible, will significantly increase the tissues resistance to deformation during an applied tensile stress.

4.5 Concluding remarks

The design of an experiment to investigate the uniaxial local apparent stiffness of ECM samples using an AFM was presented, and developed an analytical model to predict the change in the stiffness of such samples due to the influence of an external magnetic field. Experimental results were reported demonstrating (i) the effectiveness of this approach for active manipulation of ECM stiffness and (ii) validity of the analytical model.

The experimental results have demonstrated that the binding between the embedded beads and the collagen fibres plays a significant role in altering the local stiffness of ECM. This is due to the fact that beads attached to the fibers via bioconjugation create substantial additional resistance to deformation in the fibres when an external magnetic field is applied. These results suggest the possibility of creating desired 3D stiffness gradients in *in vitro* ECM to guide cell migration (i.e., 3D durotaxis).

Chapter 5

Effect of HMVEC sprouting behaviour in the modified ECM

5.1 Introduction

In the previous two chapters, it was shown that applying a magnetic field through an ECM modified with super paramagnetic beads, can change the ECM stiffness in the macro and micro scale. In this chapter an investigation was conducted on the sprouting behaviour of human microvascular endothelial cells (HMVECs) in the proposed modified ECM with a static constant external magnetic field applied in a certain direction.

Cell migration, proliferation and differentiation rely, to a great extent, on their microenvironment. Two groups of factors, namely the soluble cues and the mechanical cues, influence cell behaviour. The soluble cues consist of chemical growth factors such as the vascular endothelial growth factor (VEGF), metabolites and dissolved gases, and the mechanical cues involve composition, architecture and mechanical properties of the extracellular matrix (ECM).

It has been shown that the stiffness of the extracellular microenvironment, an insoluble cue, influences many types of cell behaviour. For endothelial cells (ECs) in particular, which are the primary cells responsible for angiogenesis, cell migration behaviour is significantly influenced by the stiffness of the ECM. For angiogenesis, changes in endothelial capillary cell shape

and function can be produced by changing ECM elasticity, adhesivity or topography, applying mechanical stresses, or altering cell-generated traction forces [138] [139] [140] [141] [142] [84]. There has been evidence that stress-induced distortion of the capillary cell cytoskeleton regulates Rho activity by controlling its upstream inhibitor, p190RhoGAP which bind to the transcription factor TFII-I [143] [144]. TFII-I binds to the initiator (Inr) region of the VEGFR2 gene promoter which is the main receptor for the growth factor VEGF and essential for angiogenesis. Mammoto et al has shown that an appropriate level of ECM stiffness may be required for optimal VEGFR2 expression and vascular development in vitro and in vivo. Furthermore, sudden changes in the mechanics of the ECM will cause a change in the active growth and differentiation of functional vascular networks in vivo [145].

Focal adhesion kinase (FAK) is an important signalling mediator between the cell and its environment (ECM). It has been shown that the deletion of FAK in isolated primary ECs results in reduced capillary formation and multiple cellular deficiencies in vitro [146]. The size and number of focal adhesions (FA) have shown to be good indicators of cell migration dynamics. It has also been observed that the mean size of focal adhesions robustly and precisely predicts cell motility independently of focal adhesion surface density [92]. There has also been evidence that cell motility and FAs are regulated by substrate flexibility. Pelham et al has shown that stiffer substrates produce an increased expression of FAKs such as vinculin, paxillin and phosphotyrosine [12]. Hence this dependence on substrate stiffness for cell motility and ECs vascular formations shows that it is possible to control angiogenesis by varying substrate stiffness.

There are many different ways by which the ECM stiffness can be altered for the purpose of observing in vitro cell behaviour in an ECM sample which have been discussed in section 2.4. These reported methods mainly manipulate soluble cues to vary the initial ECM stiffness. The ECM stiffness after fibrillogenesis is then assumed to constant. However, most in vivo ECMs have a stiffness that varies with time.

Manipulating the stiffness of ECM by mechanical means offers an alternative approach which does not rely on soluble cues. Recent results have

demonstrated the possibility of changing mechanical and rheological properties of composites with highly elastic polymer matrices that are filled with magnetic particles [104] [105]. The magnetic fields induce a magnetic moment on each of the micro magnetic particles. This causes a build up of forces within the polymer matrices. It had been reported that these materials show significant changes in their mechanical properties under the influence of magnetic fields. Similarly, the ECM is also a polymer matrix made up of many carbohydrate polymers attached to glycoproteins to form proteoglycans [147]. By embedding magnetic beads that bind onto these polymer chains, the stiffness of the ECM can also be manipulated by an external magnetic field.

Researchers will be able to study cellular responses to substrate stiffness by utilising this technique which dynamically alters the mechanical properties of the ECM. The work done in this chapter adopts this technique of exerting magnetic forces to magnetic beads embedded in the ECM, to investigate the reaction of the HMVECs to the induced change in stiffness in their microenvironment caused by the magnetic beads. This will provide useful information on the significance of substrate stiffness for HMVEC sprouting during angiogenesis.

5.2 Material and methods

Magnetic beads were embedded in the ECM and both the ECM and endothelial cells were introduced into a microfluidic device described in Section 5.2.2. The magnetic beads are embedded in the ECM via bio-conjugation between the beads and the ECM fibers as shown in Figure 5.1a. Applying an external magnetic field on the ECM produces a force gradient (as illustrated in Figure 5.1b) on the beads to resist the dislocation of the ECM fibers due to the migration of ECs. This increases the apparent stiffness in the vicinity of the ECs. With this approach, it is possible to observe the changes in sprouting behaviour of ECs when the apparent stiffness of the extracellular matrix changes.

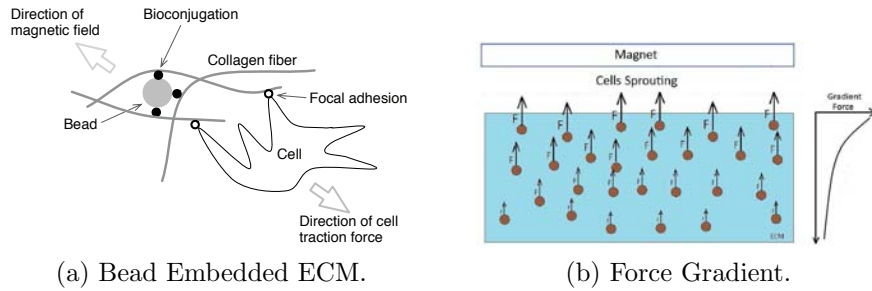


Figure 5.1: Schematic illustration of the proposed approach. (a) The magnetic beads are embedded in the ECM via bio-conjugation between the beads and the ECM fiber. (b) Applying an external magnetic field on the ECM produces forces on beads.. The magnetic field also collectively produces a force gradient on the beads to resist the dislocation of the ECM fibers due to migration of ECs.

5.2.1 Human microvascular endothelial cell culture

Adult human microvascular endothelial cells (HMVEC, Lonza, Walkersville, MD) were cultured in Endothelial Growth Medium-2MV (EGM-2MV, 2% serum, Lonza). Media was changed every two days, and cells were kept in a humidified, 5% CO_2 environment at $37^\circ C$. HMVECs were passaged once from passage 6 - 7 using EDTA solution (Gibco, Grand Island, NY). The HMVECs were delivered into cell seeding channel (a) in the microfluidic device at 3×10^6 cells/ml.

5.2.2 Microfluidic device design

The microfluidic devices (shown in Figure 5.2) were fabricated according to the design by Farahat et al [148]. Carefully patterned features were made on the surface of a polydimethylsiloxane (PDMS) substrate by imprinting with a silicon wafer mold using negative photoresist (SU-8). The PDMS layer is cut into individual devices and through holes are punched for the delivery of collagen, HMVECs and media. The PDMS layer was then plasma bonded onto a glass slide to create the microfluidic device. This device has 37 slots which allow the HMVECs to respond to a VEGF gradient and initiate sprouting. The sprouts will appear between the posts and progress from a region of low VEGF to the opposite channel which has

high VEGF levels.

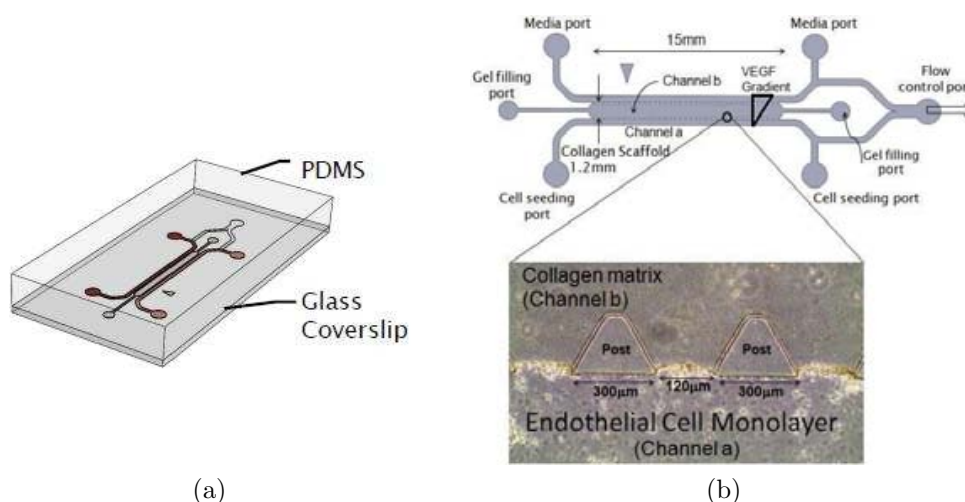


Figure 5.2: Microfluidic device for observation of HMVECs sprouting during angiogenesis. (a) The device is constructed from a PDMS layer made by standard soft lithographic techniques and bonded to a glass slide (b) The device consists of a central 3D collagen gel matrix (channel b) with a media channel on either side. The gel channel is bounded by 37 posts for the growth of endothelial cells. The endothelial cells were seeded in channel a.

Four permanent magnets, made of an alloy of neodymium, iron and boron (NdFeB) each sized 5mm by 4mm by 3mm and capable of producing a magnetic field of 0.65 T at the surface were placed on the cell seeding side of the microfluidic device. The magnets were located approximately 1.4 mm away from the EC sprouting region as shown in Figure 5.3b.

5.2.3 Embedding beads in ECM

To embed beads in the ECM with bio-conjugation, magnetic beads were prepared with a coating that has a good affinity with the collagen fibers to form a strong attachment. Similar approach as described in section 3.4.1 was used with streptavidin coated magnetic beads procured from Bangs Laboratory, IN, USA to enable bio-conjugation with the collagen fibers [115].

Once fibrillogenesis has occurred the magnetic beads and the collagen fibers

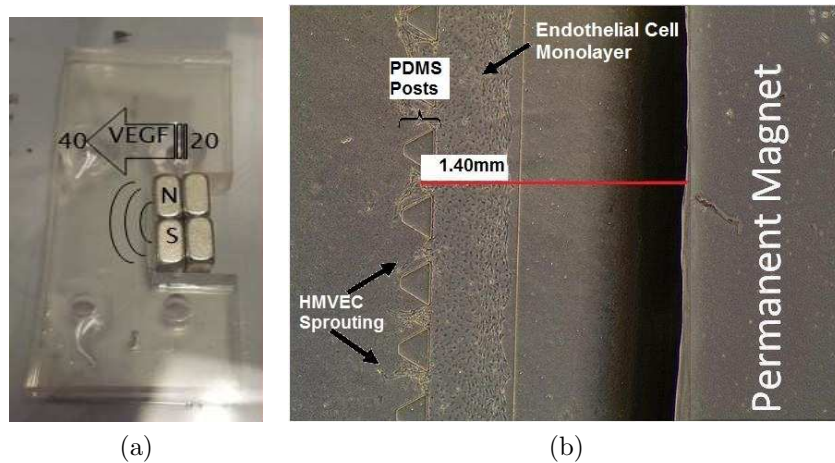


Figure 5.3: Experimental Setup (a) Four 5mm by 4mm by 3mm neodymium, iron and boron (NdFeB) alloyed magnets are placed next to the HMVEC monolayer with their poles facing the collagen channel. A VEGF gradient was added with the cell channel having 20ng/ml and the opposite channel having 40ng/ml. (b) View of the posts and the HMVEC monolayer with sprouts moving through the gel. The location of the permanent magnet is shown relative to the microfluidic device.

were observed by reflectance microscopy. Figures 5.4a and 5.4b show the reflectance microscopy image of the beads. It can be observed from the reflectance images that after fibrillogenesis, the ECM consists of a network of magnetic beads (bright spots) and collagen fibers (bright lines).

5.2.4 Tissue culture in microfluidic device

The collagen was prepared according to the recipes listed in Table 5.1. All of the samples contain 2.5mg/ml of Rat Tail Collagen Type 1 (obtained from BD Biosciences, NJ, USA). The streptavidin-coated magnetic beads were mixed into the collagen mixture. The collagen with a bead concentration of 0.075 mg/ml, was prepared according to the Table 5.1. Another collagen mixture without magnetic beads was also prepared as shown in the second column of Table 5.1 to serve as a control experiment.

The collagen - beads mixture was thoroughly vortexed for two minutes in an ice bath until a homogeneous solution was formed. 20 μ l of the mixture was then pipetted into the central 3D collagen gel port (channel

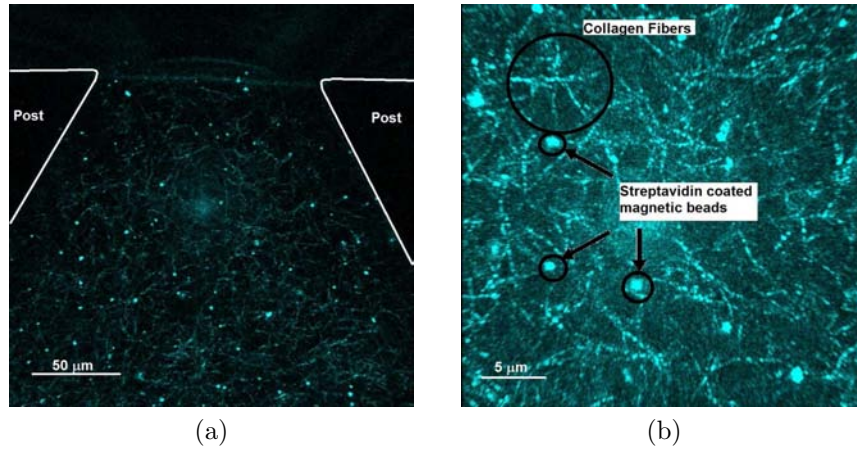


Figure 5.4: Reflectance image showing the location of superparamagnetic beads embedded in collagen. (a) Collagen - Bead matrix in the microfluidic device with posts. (b) Image obtained by 60x oil immersion objective lens in reflectance mode. The bright lines indicate collagen fibers and the bright spots are magnetic beads.

Table 5.1: Recipes for collagen preparation.

Components	Without magnetic beads	With magnetic beads (0.075 mg/ml) (Streptavidin coated)
Collagen (4.62 mg/ml)	0.216 ml (Diluted to 2.5 mg/ml)	0.216 ml (Diluted to 2.5 mg/ml)
Water	0.137 ml	0.131 ml
PBS (10x)	0.325 ml	0.325 ml
NAOH (0.5 N)	0.244 ml	0.244 ml
Beads (5 mg/ml)	0 ml	0.006 ml (Diluted to 0.075 mg/ml)
Total	0.400 ml	0.400 ml

b) carefully so that no visible air cavities were formed. For gelation, the devices were placed in an external incubator at 37°C and 5% CO_2 . To achieve self-assembly of collagen molecules into fibers and binding of beads to the collagen fibers, the samples were placed in the incubator for at least 22 hours to ensure that gelation occurred throughout the entire collagen strip.

Once gelation had occurred, HMVEC cells were delivered into channel (a) of the microfluidic device and 80 μ l of media (EGM-2MV) was added with 20 ng/ml and 40 ng/ml concentrations of VEGF (VEGF-A isoform VEGF(165), R&D Systems, Minneapolis, MN) to channel (a) and (b) respectively. The media in both channels were changed every day with the 20-40 ng/ml gradient maintained for a period of 4 days.

5.2.5 Magnetic force gradient

To compute the forces experienced by superparamagnetic particles, it is necessary to first compute the magnetic field, its magnetic field gradient and also obtain the magnetic moment of the beads m_{sat} . The force experienced by a single magnetic bead is given by the formula [11]

$$F = \nabla (m_{sat} \bullet B) \quad (5.1)$$

The magnetic field equation along the x-axis for a cuboid permanent magnet is given by [113]

$$B_x(x) = \frac{B_r}{\pi} \left[\tan^{-1} \left(\frac{ab}{2x\sqrt{4x^2 + a^2 + b^2}} \right) - \tan^{-1} \left(\frac{ab}{2(c+x)\sqrt{4(c+x)^2 + a^2 + b^2}} \right) \right] \quad (5.2)$$

where a , b and c are the height, width and thickness of the permanent magnet respectively.

The magnetic field distribution along the x axis for the permanent magnet that was used in this experiment is shown in Figure 5.5a, with $a = b = c = 5$ mm and $B_r = 1.2$ T. The magnetic field experienced by the magnetic beads in the ECM at 1.4mm away from the magnet is approximately 0.275 T (2750 Gauss).

According to Figure 5.5c, this produces a magnetic moment (m_{sat}) of 70emu/g. With this information and by using Equation 5.1 it can be calculated that each of the superparamagnetic beads experience a force

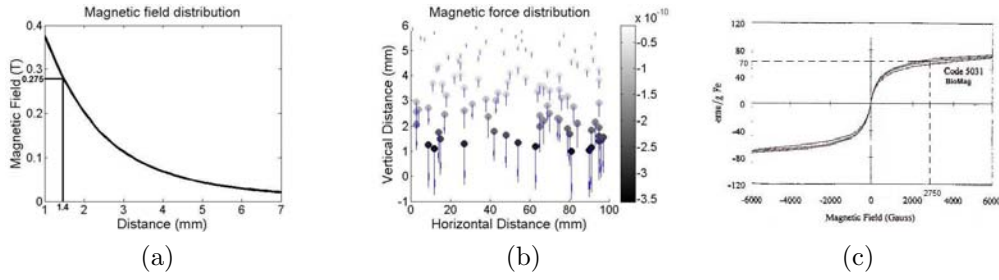


Figure 5.5: Magnet field and force analysis of BioMag superparamagnetic particles (a) Magnetic field generated, (b) Magnetic force on individual beads. The length of arrows and the grayscale intensities indicate the magnitude of force acting on each individual bead. (c) Magnetization of BioMag particles. Adapted from figure provided by Bangs Laboratory, Inc., U.S.A.

of about 0.32 nN towards the permanent magnet at a distance of 1.4 mm. This force decreases as the distance between the magnetic beads and the magnet increases. The reduction is shown in the simulated force gradient in Figure 5.5b. The permanent magnet is attached to the channel with the cells (channel a) and a VEGF gradient of 20ng/ml to 40ng/ml is added as shown in the Figure 5.3b.

In order to visualise the stresses exerted on the ECM by such forces, a simulation using COMSOL was done to investigate the von Mises stress produced by two layers of magnetic beads in the microfluidic device. The first layer has 15 beads at 50 μm away from the cells and second layer has 33 beads at 100 μm away from cells as shown in Figure 5.6a.

5.2.6 Quantification of endothelial cell sprouts

All the devices were imaged every 24hrs for 4 days using a phase contrast microscope and on day four the devices were imaged using fluorescence microscopy. The images were analysed by manually measuring the number of sprouts per device and sprout height. For each scenario, 8 devices were analysed and all 37 slots where the endothelial cells sprouted were imaged, resulting in a total of 296 slots per scenario. The conditions are summarised in Table 5.2. The average number of sprouts with heights above 100 μm per device was calculated together with their standard deviations and reported

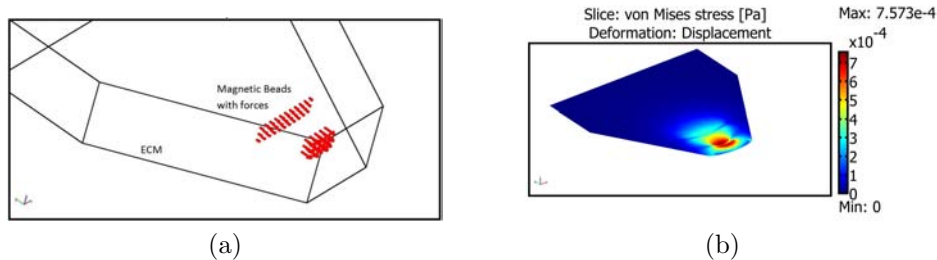


Figure 5.6: Simulation of forces on magnetic beads in the ECM (a) An example of magnetic beads embedded in the ECM. The magnetic beads are arranged in two layers experiencing forces generated by a magnetic field which are shown by the arrows. The layer further away with 33 beads experiences a lesser force compared to the layer with 15 beads which describes a gradient of forces exerted on the ECM (b) von Mises stress in the ECM due to the gradient of magnetic forces produced by the two layers of magnetic beads. It can be seen that there are varying stresses exerted in the ECM gel due to the forces from the magnetic beads. The red areas indicate regions of higher stress. These regions are situated close to the sprouting area hence increasing the amount of prestress present in this area.

in the results (Figure 5.8).

Table 5.2: **Experiment scenarios** Conditions of experiments and the number of devices used. Each scenario was done twice.

Scenario	No. of devices	Bead concentration	Magnetic field
1	4	0.075 mg/ml	off
2	4	0.075 mg/ml	on
3	4	0 mg/ml	off
4	4	0 mg/ml	on

$n = 2$

5.2.7 Cell immunofluorescence staining

The sprouts were fixed at day 4 with 4% paraformaldehyde into both the HMVEC channel and the opposite media channel and incubated at room temperature for 20 minutes. The devices were washed thrice by delivering 1x PBS into both channels. The cells were permeabilized with 0.5% Triton

X-100 for 10 mins in room temperature. Focal adhesions were stained with primary antibody anti-vinculin (Sigma V9131) overnight in 4°C, washed five times with wash buffer (0.5% BSA in PBS) and secondary antibody goat anti mouse (Invitrogen A21123) for 2 hours. After washing with wash buffer 3 times, cell nuclei and the actin filament were stained with 405 hoechst (Invitrogen H1399) and 488 phalloidin (Invitrogen A12379) at 4°C overnight. Images were obtained using a phase contrast microscope, Olympus CKX 41 and a confocal microscope, Olympus IX 81. Fluorescent image processing was done using IMARIS[®] software to extract the different immunofluorescence channels from the image data. A two-tailed, non-paired, Student's *t*-test was used to compare the number of focal adhesions in each scenario.

5.3 Results and discussion

5.3.1 Sprouting number and height of sprouts

Figure 5.7 shows the phase images taken on Day 1 and Day 4 of the experiment. From Figure 5.7b it can be observed that, although a VEGF gradient of 20ng/ml to 40ng/ml was added to the device, very little sprouting occurred during the first four days. It can be clearly observed that there was a higher level of angiogenic activity on Day 4 (Figure 5.7d), for the case where the device was exposed to an external magnetic field. The amount of cell invasion into the collagen with beads and the magnetic field has markedly increased in this case.

Lumen formation has been observed to be highly dependent on substrate stiffness [149]. Endothelial cells increase their spreading and extension formation with increasing stiffness of the ECM [150]. The chart in Figure 5.8 shows the average sprout height and number of sprouts in each of the scenarios in this study. From this chart it can be seen that the device with the magnetic field and magnetic beads contains the largest number of sprouts that are greater than 100 μ m on Day 4. This indicates that the forces produced by the magnetic field on the magnetic beads had resulted

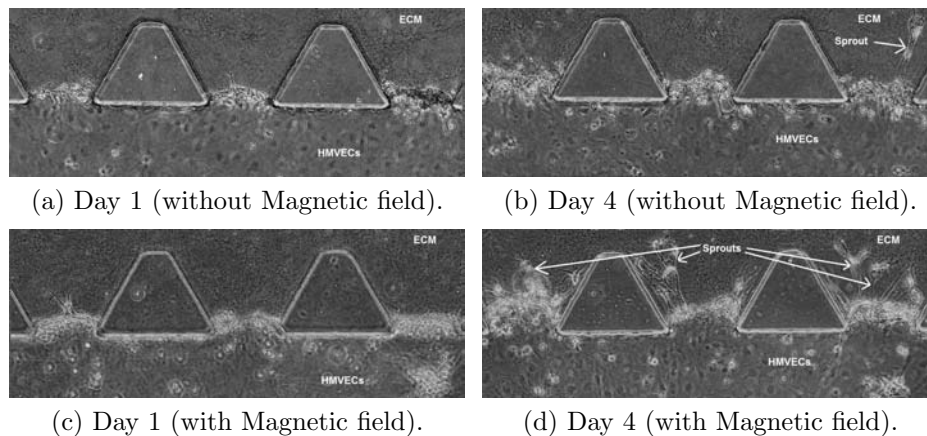


Figure 5.7: Sprouting behaviour and structure at different magnetic conditions. Images of ECs migration on Day 1 and Day 4 in collagen gel with beads, without magnetic field (a and b) and with magnetic field (c and d). More sprouts have occurred in (c) and (d) indicating a preferential HMVEC sprouting condition where the beads exert magnetic forces within the ECM.

in an increased stiffening for HMVEC sprouting.

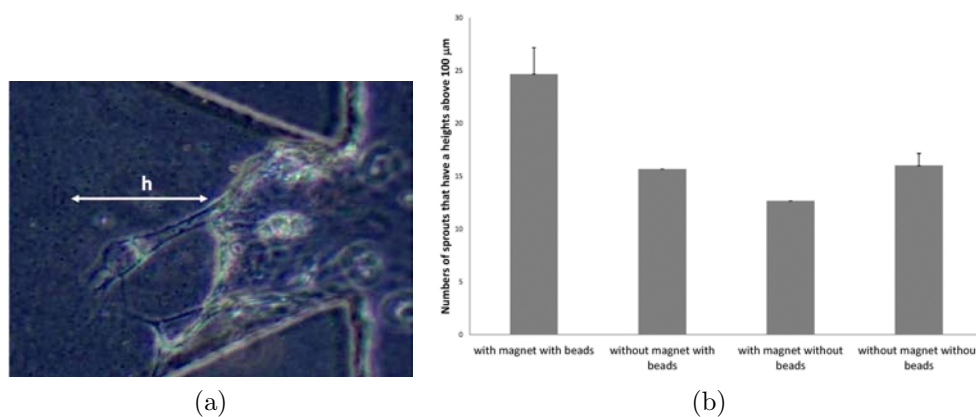


Figure 5.8: Quantification of the extent of sprouting in microfluidic devices. (a) Height (h) of each sprout is measured and counted. (b) Average number of sprouts that have heights above $100\mu\text{m}$ for each scenario were measured on Day 4.

The active signals 405 hoechst blue and 488 phaloidin green (produced from the confocal image in Figure 5.9) indicate no toxicities inflicted by the magnetic beads on the ECs during their proliferation stage. It can hence be concluded that the embedding of beads in the ECM did not impact EC

proliferation and migration as compared to that in pure collagen.

It can also be verified that the cell density (number of blue dots in Figure 5.9a and Figure 5.9b) along the monolayer was consistent between the two sets of samples. The green colour (from the stains for the actin filament) shows the cell structure of the ECs during angiogenesis. From the reflectance images shown in Figure 5.9c and Figure 5.9d it can be seen that the brighter areas, which indicate higher concentrations of collagen density, corresponded to locations of the tip cells [151].

Figure 5.9 shows two sets of images of the microfluidic channel taken on Day 4. It can be seen that on Day 4 the ECs in the microfluidic device under the influence of the magnetic field with magnetic beads had migrated further into the region of higher VEGF concentration, as compared to the ECs in the microfluidic device without the magnetic field. Cell spreading is known to be in direct relation with substrate stiffness. Particularly, there is a significant reduction in cell spreading on soft substrates compared to cell spreading on rigid substrates [152]. It can be seen from Figure 5.9a and 5.9b that the leading tip cell is more spread with increased filopodia extrusion in the device with magnetic field and magnetic beads which is indicative of a stiffer substrate in 5.9b than 5.9a.

5.3.2 HMVEC focal adhesion numbers and size are dependent on amount of prestress in ECM

Vinculin staining was done on Day four to investigate the effect of the magnetic field on HMVEC focal adhesions. Focal adhesions (FAs) are areas on a cell membrane that transmit force and regulate signals. They mediate Cell-ECM adhesions and interactions such as anchorage. FAs function as mechanical linkages to the ECM and serve as a biological signalling complexes that concentrate and direct many signalling proteins through integrin binding and clustering [93]. Vinculin is known to be one of the primary proteins that exists in FAs [94]. Due to their dynamic nature, FAs may increase or decrease in size depending on their constituent proteins. These proteins act in response to the external microenvironment, one of the

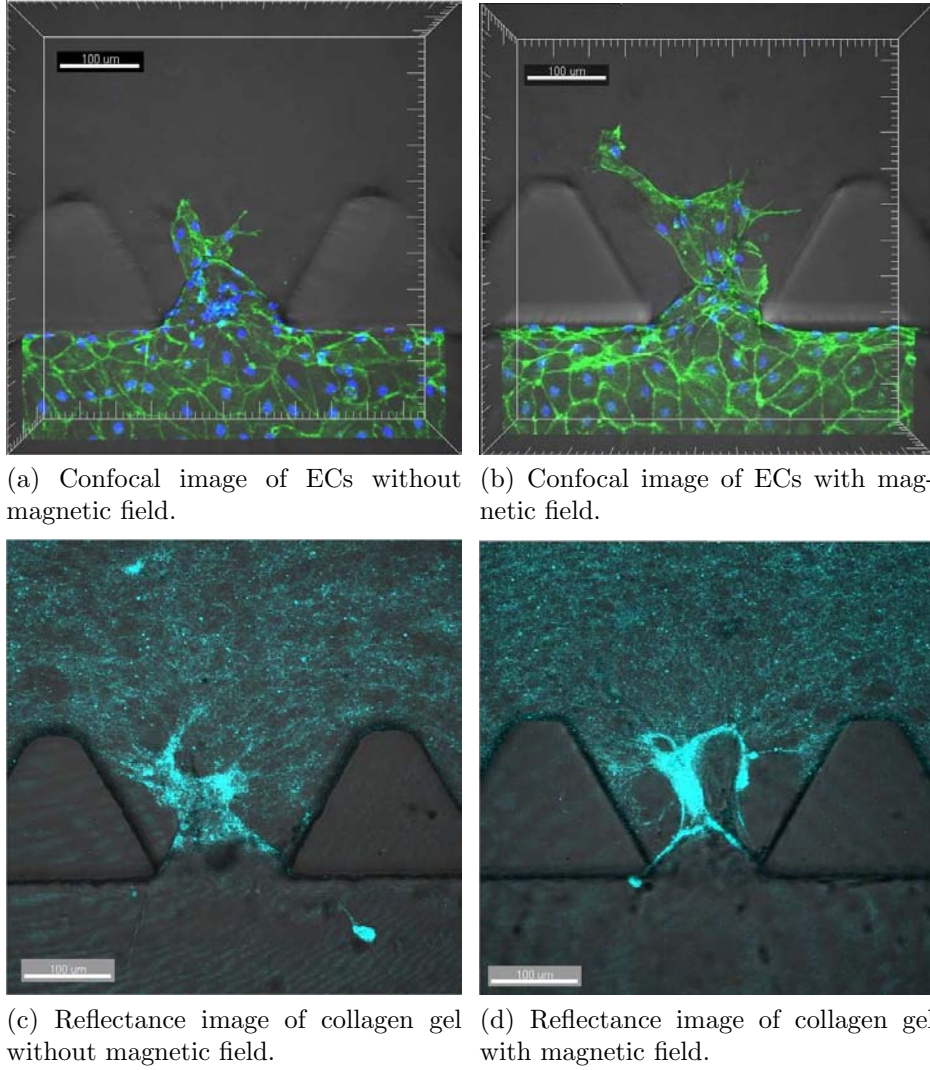


Figure 5.9: Confocal images of ECs on day 4. The nucleus is stained with 405 hoechst blue and the actin filament is stained with 488 phalloidin green. Greater expression of actin stress fibers were observed in (b) compared to (a). The leading cell's (tip cell) filopodia extensions are more in number and spread in (b) compared to (a). Brighter areas in the reflectance images (c) and (d) show higher collagen concentrations where the tip cells and lumen walls are located.

stimuli being matrix stiffness. FAs are able to sense the stiffness of the extracellular matrix and act according to it [96]. A stiffer matrix contributes to more FAs. Furthermore focal adhesions on stiffer substrates are static, stronger, larger and more stable [12]. In this work, vinculin was stained on sprouting HMVEC to observe the effect of FA formation in the different sets as described in Table 5.2.

The red fluorescent vinculin stained spots shown as in Figure 5.11a were counted using an Imaris spot counter imaging tool and the results are shown in Figure 5.11b. An IMARIS measuring tool was used to measure the largest diameter of FA in each scenario as shown in Figure 5.11c.

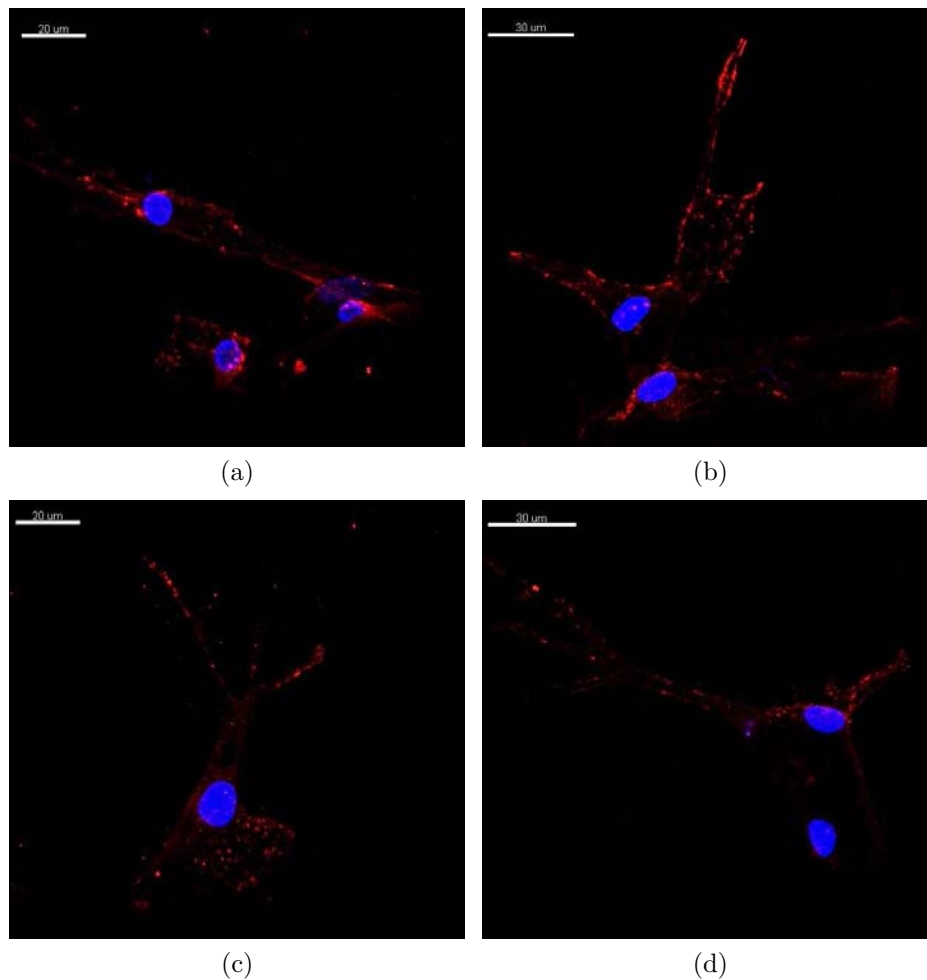


Figure 5.10: HMVECs stained with vinculin to observe Focal adhesions (red) and nucleus stained with Hoechst (blue). (a) Focal adhesion staining of ECs on Day 4 without a magnetic field and ECM with magnetic beads, (b) Focal adhesion staining of ECs on Day 4 with a magnetic field and ECM with magnetic beads, (c) Focal adhesion staining of ECs on Day 4 without a magnetic field and ECM without magnetic beads, (d) Focal adhesion staining of ECs on Day 4 with magnetic field and ECM without magnetic beads.

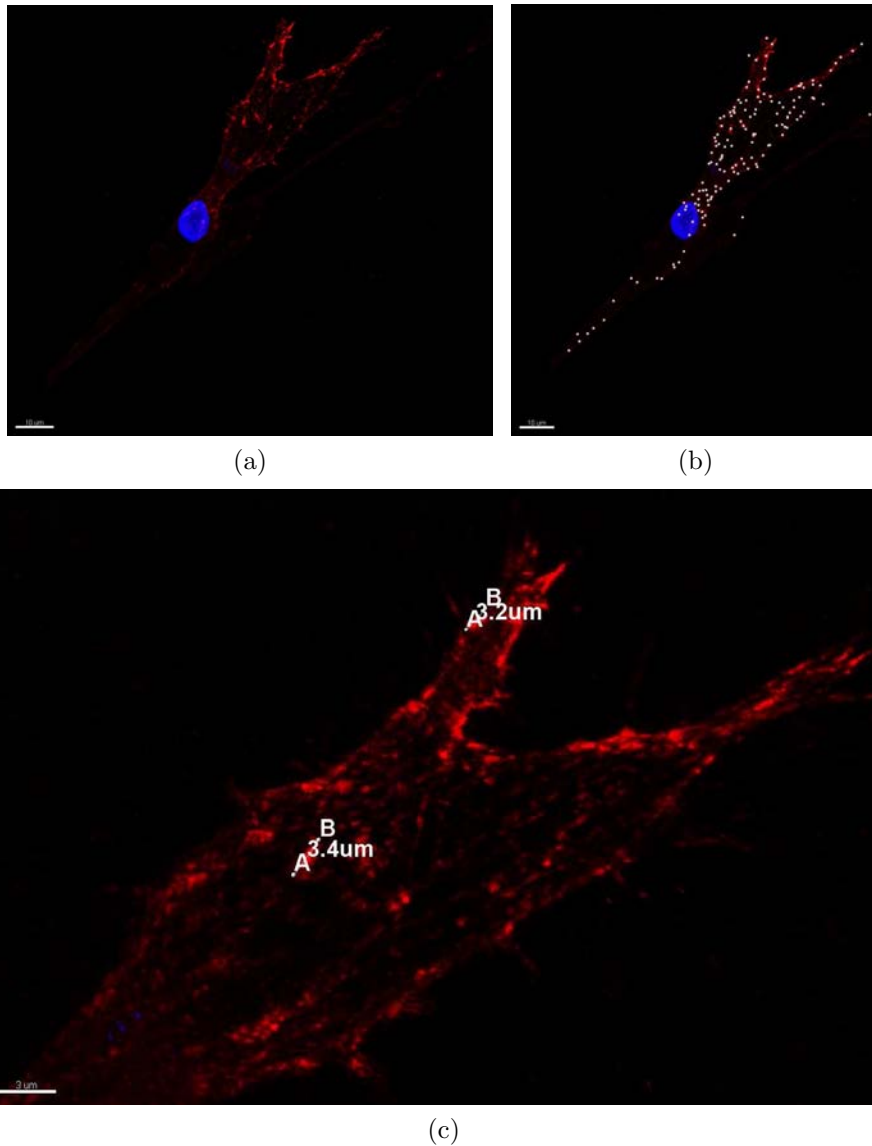


Figure 5.11: Quantification of focal adhesions according to numbers and size. (a) Example image of an Endothelial cell stained with vinculin in ECM with beads and with magnetic field, (b) An example of FA counting done with IMARIS spot counter imaging tool, (c) Diameter of the FAs were measured using IMARIS measuring tool. The largest diameters were selected and measured.

The results from the number of FAs and largest diameters of FAs in each scenario are shown in Table 5.3. From Table 5.3 it can be seen that the device with a magnetic field applied produced more and larger FAs. This result implies that the magnetic bead embedded ECM with a magnetic field

provided a stiffer substrate for HMVECs to adhere to. The higher number and larger size of focal adhesions on the leading cell indicate that they are more stable and stronger, hence leading to higher migration and angiogenic activities [92] as shown by the sprout heights in Figure 5.8.

Table 5.3: Focal adhesion analysis

Set No.	Total number of FAs			Maximum diameter of FAs (μm)		
	Mean	Variance	P value	1st largest diameter	2nd largest diameter	3rd largest diameter
1	110	25	0.0009*	2.1	2.0	2.0
2	164	35		3.1	2.9	3.0
3	75	20.9	0.7277	1.3	1.4	1.3
4	78	20.8		1.5	1.2	1.4

5.4 Concluding remarks

It was shown that the application of a magnetic field on the embedded beads significantly affected the activities of ECs. Embedding these particles in the ECM creates a crosslink zone as the beads bind onto the collagen fibers, resulting in an increase in the stiffness of the collagen. More significantly, when the magnetic field is present, a bead located approximately 1.4 mm away from the permanent magnet is estimated to exert a force of 0.12 nN. Collectively such forces in general oppose the cell traction forces (estimated to be up to 57 nN for an EC [8]) as ECs move away from the monolayer and into the collagen gel. This resistance can be considered as an increase in the apparent stiffness of the ECM in the vicinity of the migrating cells. This effect has been shown in Figure 5.6b when the forces by two layers of magnetic beads were simulated and the region of high stress was shown to be near the area of sprouting HMVECs. Therefore the cells tend to migrate preferentially in such an environment, since ECs are known to have increased motility and spreading in areas with higher stiffness [153].

It has been observed in previous literature that a reduction in collagen density would lead to a significant decrease in the expression of vinculin [154]. From the immunofluorescent staining results reported in section 5.3.2, vinculin recruitment in focal adhesions was observed to increase by 49% in the device with magnetic field during angiogenesis. This could be due to the deformation and movement of collagen when the beads were pulled closer towards the permanent magnet which resulted in an area of higher collagen density near the HMVEC sprouting region within the microfluidic device.

The results from this work have demonstrated the possibility of creating desired stiffness gradients in an ECM *in vitro* to influence cell behaviour. In order to practically apply this approach of active ECM stiffness manipulation, further experimentation and analysis to clarify various issues. First, the effect of a number of variables on the stiffness of the bead-embedded ECM remains to be explored; these variables include bead concentration, size and placement of the magnets and their distance to the ECM sample,

and the strength of the magnetic field, etc.

Second, although magnetic beads have been used in many applications (both *in vivo* and *in vitro*), their effect on the actual biological behaviour of cells are not yet fully understood. This is particularly true when an ensemble of beads is embedded in the ECM via bio-conjugation. It may be argued (based on available experimental results, e.g., [121] [122] [155]) that the bio-compatibility and toxicity of these magnetic beads with respect to its biological environment solely depend on the coating on the surface of the magnetic particles. Hence it is essential to verify that such an ensemble of beads do not directly interfere with the natural behaviour of cells.

Chapter 6

Localisation of magnetic fields

6.1 Introduction

Results from the previous chapters show the possibility of changing the stiffness of a modified ECM and affecting endothelial cell sprouting behaviour during angiogenesis. In this chapter, a novel approach to generate a micromagnetic field is introduced. This approach uses a specialized electromagnetic needle (EMN) and collectors.

Vascularisation by endothelial cells (EC) is a key component in tissue engineering and is essential to the organisation and architecture of new tissues. Cellular differentiation, proliferation and apoptosis of ECs is dependent on the bio-chemical and mechanical properties of the extracellular matrix (ECM). In particular, ECM stiffness has been shown to affect EC growth rate and vascularisation. Embedding super paramagnetic micro beads in the ECM and applying magnetic field gradients induces stress in the ECM. Consequently, as the apparent stiffness sensed by the ECs changes, the cell growth rate is enhanced or reduced, hence simulating or inhibiting angiogenesis. However, the growth direction of the angiogenesis is only determined by biological behaviour and happens in a uncontrolled manner. This chapter aims to address this issue and engineer an approach to influence the growth of vascular networks. Vascularisation is driven by a single leading cell (tip cell) which secretes bio-chemical cues to the following cells. Manipulating the path and diffusion of the leading cell would result in a controlled directional growth and thus enable engineering of ar-

bitrary networks in tissues. In the previous chapters, streptavidin-coated micro beads have been attached to collagen fibers. By utilising localised magnetic fields, these micro beads can be trapped and moved to arbitrary positions. If strong localised fields on a micro scale can be generated, micro magnetic beads can be trapped in the vicinity of the leading cell. This will provide a certain degree of control over the local ECM stiffness near the cell and influence its migration direction.

Directing the beads in the stiff ECM requires strong magnetic forces and demands novel concepts of micromagnetic field generation. Section 2.6 has described a few methods used to create high magnetic fields and forces to trap and move magnetic particles in fluid medium. In this chapter a system of equivalent magnetic dipoles and COMSOL[®] were used to analyse the magnetic fields produced by conical shaped electromagnetic needles. This chapter will describe novel electromagnetic needle designs and implementations that will produce high field gradients and localised magnetic field concentrations. This chapter also describes the experimental results performed to obtain the force applied by an electromagnetic needle on a single magnetic bead.

6.2 Magnetism

Magnetic fields are generally created by two sources; permanent magnets and moving electric charges. Permanent magnets are made up of particles containing non-zero intrinsic magnetic moments. They create a constant magnetic field.

Magnetic fields can also be generated dynamically by moving electric charges based on Ampere's Law, which states:

$$\oint_C \mathbf{B} \cdot d\mathbf{l} = \mu_0 \int_S \mathbf{J} \cdot d\mathbf{S} \quad (6.1)$$

where \mathbf{J} is the current density passing through the surface area, S , \mathbf{B} is the magnetic field, μ_0 is the magnetic constant and C is the closed curve around S . Ampere's Law states that every electric current generates magnetic fields

and that the strength of the magnetic field is defined by the electric current density. For electric conductors, this current density is obtainable by $J = \frac{I}{R^2\pi}$ where I the current and R is the radius of the conductor cross-section. Applying Amperes Law to a single conductor yields:

$$B = \frac{\mu_0 I}{2\pi} \cdot \frac{1}{r} \text{ for } r > R_{\text{Conductor}} \quad (6.2)$$

Magnetic fields are vector fields which may be described at any given point by their direction and magnitude. There are two types of fields referred to as magnetic fields; the H-field and B-field. Both fields are closely related but distinguishable from each other. Historically, H-field is known as 'magnetic field'. However, for many purposes utilising the magnetic B field is more practical. When any material is exposed to a magnetic field, its response depends on its intrinsic magnetic properties. This response results in the magnetisation (M) of the material which is related to the material's magnetic permeability, μ , hence obtaining the relation between H-field and B-field. From here on the term 'magnetic field' will refer to the B-field.

$$B = \mu(H + M) \quad (6.3)$$

If two magnetic fields overlap, their vector fields can simply be added utilising the principle of superposition. With this powerful relation, it is possible to render strong concentrated localized magnetic fields by skillfully placing magnetic fields which cancel each other out or add up.

This has two important implications for magnetic fields. First, the magnetic field decrease with $\approx \frac{1}{r}$, where r is the distance away from the source of magnetic field. Second, by superposing fields, the field strength can be increased. Considering a coil, through superposition, a constant magnetic field is created in the centre axis of the coil.

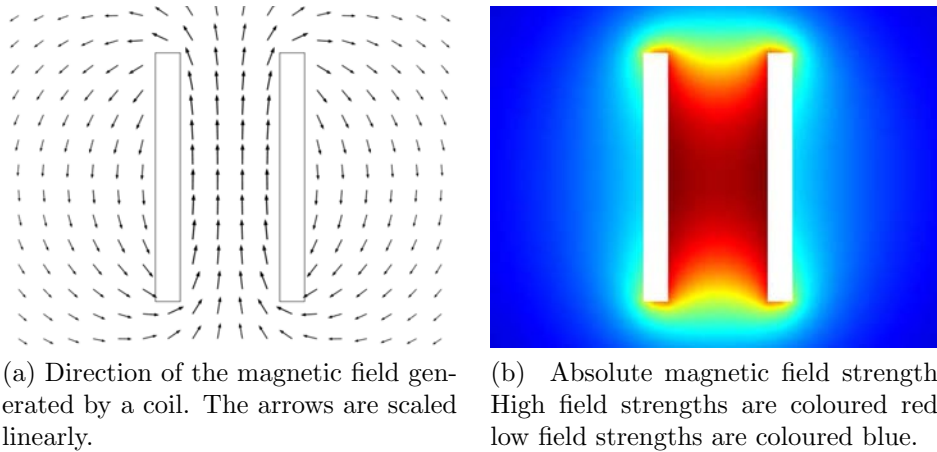


Figure 6.1: Magnetic Field generated by a coil.

Figure 6.1 shows the field generated by a coil in a physics simulation. Figure 6.1(a) shows the direction of the magnetic field plots and Figure 6.1(b) the absolute value of the magnetic field. As expected, the magnetic field is strongest where both fields overlap and superpose.

By using the principle of superposition, magnetic fields generated using different geometries can be plotted by using a method based on a system of equivalent magnetic dipoles [156]. An elementary magnetic dipole of volume V' , has a magnetic moment, $d\mathbf{m}$,

$$d\mathbf{m} = \mathbf{M}dV'$$

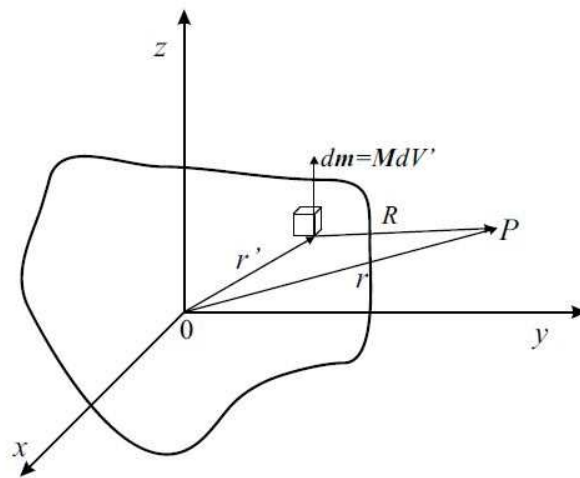


Figure 6.2: Elementary magnetic dipole.

This magnetic moment produces a field at point P, the elementary magnetic scalar potential,

$$d\varphi_m = \frac{1}{4\pi} \frac{\mathbf{R}d\mathbf{m}}{R^3} = \frac{1}{4\pi} \frac{\mathbf{R}\mathbf{M}}{R^3}dV' \quad (6.4)$$

Where $R = |\mathbf{r} - \mathbf{r}'|$ is the distance from the point where the magnetic field is being calculated to the elementary source, and $\mathbf{R} = \mathbf{r} - \mathbf{r}'$.

After integration, the magnetic scalar potential is obtained as,

$$\varphi_m = \frac{1}{4\pi} \int_V \frac{\mathbf{R}\mathbf{M}}{R^3}dV' \quad (6.5)$$

Subsequently the magnetic field vector can be expressed as

$$\mathbf{B} = -\nabla\varphi_m \quad (6.6)$$

6.2.1 Magnetic material properties

When exposed to magnetic fields, all materials interact with the field. This interaction with the magnetic field depends on an intrinsic material property. There are three main types of magnetic materials; ferromagnetism and paramagnetism and super paramagnetism. Magnetic materials are typically characterised by their hysteresis curve as shown in Figure 6.3. The hysteresis loop represents the materials response to an external magnetic field, B, in terms of its own magnetisation, M. The magnetisation M, is the materials response to the applied magnetic field.

The nominal values of saturation field, B_S , the remanence, B_R and the coercivity, H_C , characterize the magnetic properties. Figure 6.3 shows the hysteresis curves for three types of magnetism mentioned earlier. The curve plots the materials magnetisation, M , that results from an externally applied B -Field. The highest magnetisation possible is called saturation, B_S . Ferromagnetic materials exhibit a high magnetisation at their saturation. When the B field is removed, the material retains part of the

magnetisation. This is the remanence, B_R . In order to remove the remanence, a negative B field of the strength of the materials coercivity, H_C , has to be applied. Depending on the strength of the materials' remanence, hard magnetic materials typically have high remanences and soft magnetic materials have low remanences.

Contrary to ferromagnetism, paramagnetism and super paramagnetism exhibit neither remanence nor coercivity. Their magnetisation directly depends on the magnetic field and differs only in terms of their saturation magnetisation. Therefore the magnetisation is independent of previously applied magnetic fields. As an approximation for low field strengths, the material's magnetic permeability, μ and the closely related susceptibility $\chi = \mu - 1$ provide a linear relation between the H field and the magnetisation M : $M = \mu H$. Often μ is described relative to the vacuum permeability μ_0 : $\mu_r = \frac{\mu}{\mu_0}$. Therefore Equation 6.3 can be simplified to:

$$B = \mu_r \mu_0 H \quad (6.7)$$

6.2.2 Magnetic forces

When a material is magnetised, it starts interacting with the magnetic field in the same way that two magnets interact. Their attraction force depends on the magnetic field and the magnetisation of the material. This relation is mathematically described by:

$$F = -\nabla(-M \cdot B) \quad (6.8)$$

Magnetic fields decrease with $\frac{1}{r}$. The gradient of the field and thus the acting force will decay with $\approx \frac{1}{r^3}$. This requires the field source to be either very strong or very close in order to magnetically manipulate objects, thus a major challenge when designing devices for magnetic micro manipulation.

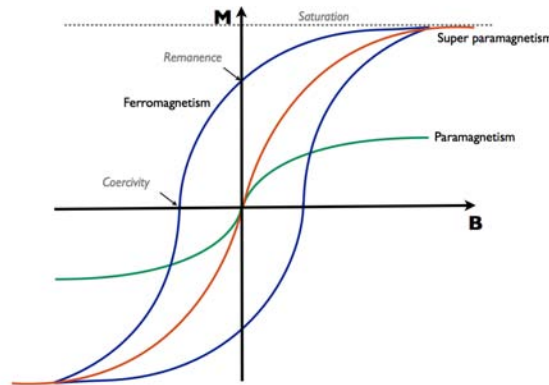


Figure 6.3: The hysteresis curve characterises the behaviour of materials when exposed to a magnetic field B . The magnetic field B is plotted against the magnetisation of the material. When a magnetic field is applied ferromagnetic materials exhibit a high magnetisation at their saturation. If the B field is removed the material retains part of the magnetisation. This is the remanence and if the inner magnetisation is completely removed a B field of the strength of the materials coercivity has to be applied. Contrary to ferromagnetic materials, paramagnetic and super paramagnetic don't exhibit any remanence and differ only in terms of their saturation magnetisation

6.2.3 Magnetic needles

A new approach for micro manipulation has been developed by using sharpened electromagnetic needles to generate microscale magnetic fields. In this approach, micro magnetic fields are generated and super paramagnetic micro or nano particles are trapped and arbitrarily manipulated [157]. Magnetic needles present many advantages in the field of magnetic micro manipulation because they are inexpensive, relatively easy to set up, very versatile and high forces can be applied.

In a magnetic needle, a solenoid is wrapped around a ferromagnetic core. Since the magnetisation, M , of ferromagnetic materials is high, high magnetic field strengths are generated. Figure 6.4 shows the schematic cross section of a magnetic needle. By using an external electric current, I and a high relative permeability, μ_r , a strong magnetic field is generated in the ferromagnetic core. The generated field at the sample is a result of the geometry of the core and in particular of the tip. For a single coil, the

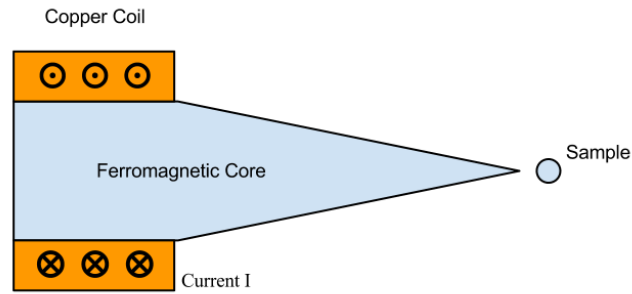


Figure 6.4: Schematic cross section of a magnetic needle. Magnetic needles consist of two parts: a ferromagnetic core and a electrical conductor wrapped around the coil. Through the external electric current, a magnetic field is induced in the ferromagnetic material. The magnetic field in the core is very strong due to the magnetisation of the ferromagnetic core. Thus, the utilised field at the sample is a result of the form of the core and in particular, of the tip

tip size determines the resulting field [158]. If the position of the needle relative to the sample is changed, the magnetic sample will follow the field gradient. Therefore the direction and magnitude of the force acting on the sample are adjusted and controlled by the position of the needle and the current through the conductor.

State of the art in electromagnetic needles

Electromagnetic needles (EMNs) were first proposed by B. Matthews *et al.* [157]. Matthews proposed a new temperature controlled electromagnetic device to generate custom magnetic fields. Contrary to previous bulky micro manipulators they developed an easily portable, cheap device which could produce high field gradients, high field strengths and thus high forces (up to 8nN at the tip) in order to micro manipulate micron and sub micron particles. At the same time they could generate localised fields on a very small scale and found the generated field to be closely related to the shape and size of the EMN tip leading to an optimisation challenge. Utilising a multi physics engine in order to simulate different EMN designs Xiang *et al.* [158] found ideal design parameters for the EMNs designed by Matthews which allowed them to generate maximum field gradients and

thus maximum forces. In 2010 Zhang *et al.* [159] addressed the issue of active control of the micro beads by designing a force-feedback control system that controlled the position of the particle. But instead of utilising a single needle they developed a quadrupole magnetic setup with 4 tips. All presented EMNs have the inherent disadvantage of proximity. If the needle is placed too far away from the sample field the gradients decrease quickly and the application of localised fields and forces becomes impossible.

In order to counter this challenge a different approach was engineered by T. Fallesen *et al.* [160] in 2010. They introduced a setup of two electromagnets. The setup creates a nearly uniform distribution of magnetic field below the gap of the two electromagnets. This enables micro manipulation at a distance of up to 10 μm . However, the forces applied are relatively low (12 pN), compared to EMNs. Furthermore, the device is unable to perform manipulations on single magnetic beads due to its high field distribution. Therefore, this approach is unable to generate sufficiently small field (or large forces) required to micromanipulate single magnetic beads, unlike magnetic needles.

6.2.4 Magnetic particles

In order to induce arbitrary strains into the ECM, super paramagnetic particles are added into the ECM similar to the previous chapters. Super paramagnetic particles are chosen for their excellent magnetic properties. If external magnetic fields are applied they exhibit a very strong magnetisation (see Figure 6.5) and thus the application of high magnetic forces becomes possible. In addition they do not retain any magnetisation when the field is removed. Therefore the induced strain is controlled only by the magnitude of the magnetic field. When such particles are implemented, two important challenges need to be addressed: The interaction of the particles with the biological system and their attachment to the existing structures in order to transfer the induced forces to the biological system.

These two challenges were resolved by coating the particles with Streptavidin. Streptavidin contains an Arg-Tyr-Asp (RYD) amino-acid sequence that mimics the Arg-Gly-Asp (RGD) receptor domain of fibronectin. This

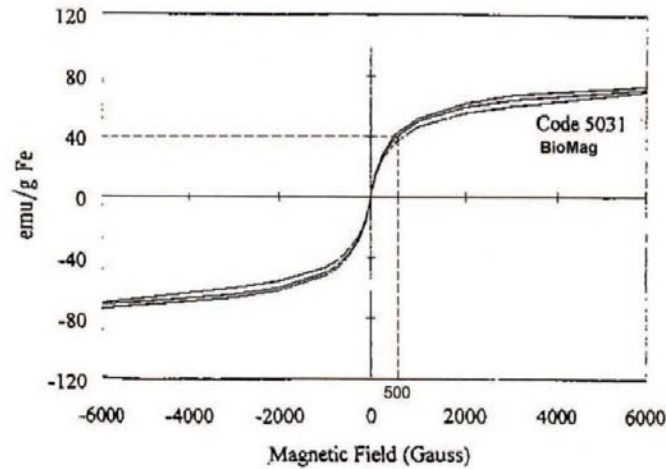


Figure 6.5: Magnetic hysteresis curve of the utilised super paramagnetic streptavidin-coated magnetic beads, Bangs Laboratories (Fishers, IN).

sequence enables streptavidin to affix to collagen-rich areas. The complementary shapes, charges, polarity, and hydrophobicity of the streptavidin and the collagen fibers permit multiple weak interactions which, in combination, produce a tight binding [115] [116] [117]. Since the super paramagnetic particles are attached to the ECM fibers, the forces applied to the magnetic field are transferred to the ECM and thus the apparent stiffness is changed at the micro and macro scale.

6.3 Simulation of magnetic fields and forces generated by electromagnetic needle (EMN) configurations

Electromagnetic needles were chosen for their highly localised magnetic fields. A simulation was done to determine the magnetic field strength and the forces acting on a single super-paramagnetic bead. The goal in the simulations is to design setups, which are able to exert significantly higher forces than the existing EMNs. Consequently the design of the setup was revised and new setups were designed in order to exert higher forces on the particles. These setups are simulated and discussed in section 6.3.3.

Section 6.2 introduced a method of obtaining the resultant magnetic fields using different geometries of permanent magnets by using a system of equivalent magnetic dipoles. This method is used to simulate the field generated by the electromagnetic needle tips. The electromagnetic needle is first modelled as a cone as shown in Figure 6.6. The cone is separated into many discs. Each disc represents one dipole element and the resultant scalar magnetic potential (φ_m) of the cone with a particular magnetization direction at point P is obtained by integrating each element down the apex.

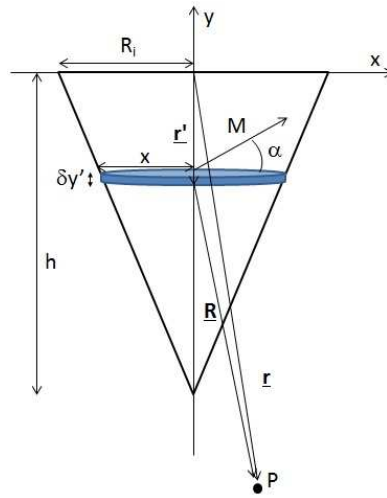


Figure 6.6: Magnetic field determination from conical geometries

$$\varphi_m = \frac{M}{4\pi} \int_{x_1}^{x_2} \int_{y_1}^{y_2} \int_{z_1}^{z_2} \frac{(x - x')\cos(\alpha) - (y - y')\sin(\alpha)}{[(x - x')^2 + (y - y')^2 + (z - z')^2]^{3/2}} dx' dy' dz' \quad (6.9)$$

The simulations were conducted with the AC/DC Simulation package of COMSOL Multiphysics. The magnitude of the force exerted on a single bead is determined by:

1. Magnitude of the magnetic field
2. Gradient of the magnetic field

The magnetic field magnitude increases the magnetisation of the particles and results in a stronger interaction between field and magnetic particles. The magnetic field gradient determines the interaction between particles

and field: Magnetic particles are pulled towards regions of higher magnetic fields. High magnetic field strengths and gradients lead to higher forces acting on individual magnetic beads. Therefore, the area near the tip of the needle where the magnetic field strength and gradient are strongest, will induce the highest forces on magnetic beads. Ideally, the tip of the needle should be in close contact with the magnetic particles. However, in our microfluidic device, the particles are embedded in collagen gel which is constrained in a device with a glass lid of 250 μm thick was bonded to it. Hence, the EMN tip is separated from the magnetic particles by this distance. To determine the force acting on the magnetic particles in the device, simulations were performed with consideration of the actual possible distances in which the needle can be placed away from the particles.

6.3.1 Single EMN

The first prototype electromagnetic needle was designed and sent for fabrication in ETH Zurich. Before implementing and operating the needle, estimations of the forces that it can generate are required. A COMSOL simulation of the needle was done in order to estimate the resulting field acting on the super paramagnetic beads. Then the calculation of the force acting on the beads was done according to Equation 6.8.

For the EMN a 2D axis rotational model was chosen. In the 2D axis rotational model the entire geometry of the needle is represented while utilising a 2D simulation. The model was set up in COMSOL as shown in Figure 6.7 (a) which shows the the location of the tip, above the ECM. High and low field strengths are coloured red and blue respectively. The sample position is indicated in the Figure 6.7 (b).

Therefore, it can be seen that the simulated EMN concentrates the magnetic flux at its tip. High fields and gradients are simulated around the tip's vicinity. At a sufficient distance away, the field is decreased at a rate of $\frac{1}{h}$, where h is the distance from the needle tip.

The simulation results (Figure 6.7 (b)) show fields of up to 219mT at the tip of the needle. Note that in practice, there may be a broader distribu-

tion of the field at the tip as the tip is more rounded. Simulation results show that at the working distance of $250\mu m$, the maximal field strength is $21.5mT$.

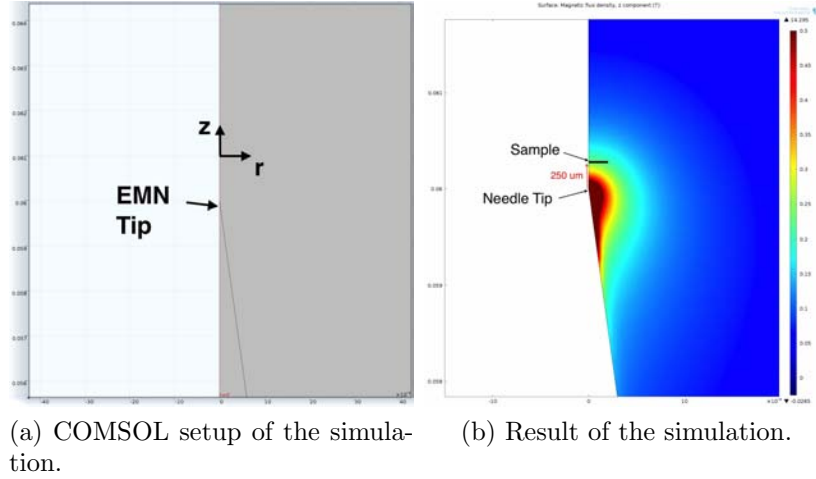


Figure 6.7: (a) A sketch of the geometry of EMN tip. (b) Magnetic B-Field generated by the EMN fabricated by the ETH Zurich. Strong fields are coloured red, weak blue. The maximal field strength is achieved at the tip of the needle. The sample is indicated at a distance of $250\mu m$ from the tip.

6.3.2 Force calculation single EMN

From the B-field simulated with COMSOL, the forces on the magnetic beads can be determined through the equation $F = \nabla(M \cdot B)$ (see Equation 6.8). The magnetisation, M , of the particles is dependant on the B-Field acting on them. M is approximately linear to the field for field strengths less than $100mT$ (Figure 6.5). Therefore, M is calculated by:

$$M = V_{particle} \times \rho_{Fe_2O_3} \times \Delta m B \quad (6.10)$$

where Δm the gradient of the hysteresis curve of the particles.

The relation of the B-Field and the magnetisation per mass is represented in the hysteresis curve (Figure 6.5). The total force acting on a single bead is calculated using the above equation. Figure 6.8 shows a plot of the results of the calculations vs the position of the beads.

At the working distance below the glass lid of $250\mu m$ the maximal total force is $F_{tot} = 19.6pN$. This force is directed towards the tip of the needle.

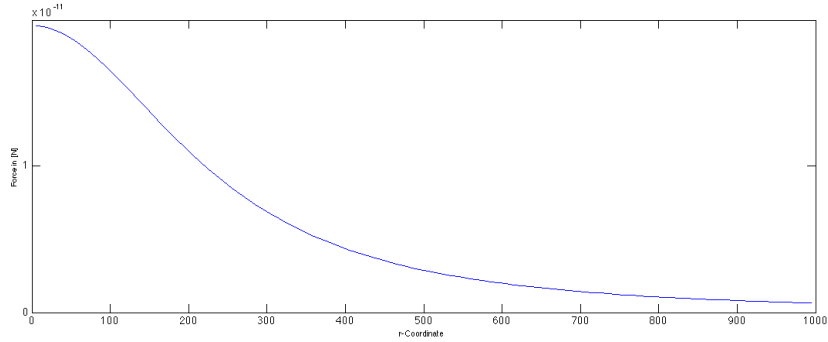


Figure 6.8: Total force acting on a single particle in the sample.

6.3.3 Single collector configurations

The results described in the section above showed that the forces exerted on the beads were relatively low compared to the force at the needle tip. For this application, it is necessary to design a setup which reduces the force decay over distance.

A non-field-generating needle tip (collector) is introduced to address this issue. This second needle tip operates as a field collector, allowing higher field strengths to be applied at longer distances. In a setup with multiple needles the field superposition described in section 6.2 is used to create the desired effect. Simulations were performed to quantify the improvements that can be achieved in a magnetic setup using a field collector. Figure 6.9 shows this setup. The field generated by the first generating needle tip (right) is collected by the second needle (left). The only difference between the EMN and the collector is that the collector is the core of the EMN. The collector and EMN core geometry are identical. As seen in section 6.3.1 the field generated by the first EMN is highly localised. Therefore, for significant field interactions between the two needle tips, they need to be placed at distances in order of microns ($10\mu m - 500\mu m$). The relevant parameters for the field interaction were identified: First the distance be-

Length	Core Diameter	Opening angle	Tip radius
20cm	0.5mm	16.7°	76.8 μ m

Table 6.1: Measures of the needle proposed by Xiang

tween the needle tips and second the angle β between the vertical axis and the centre axis of the EMNs.

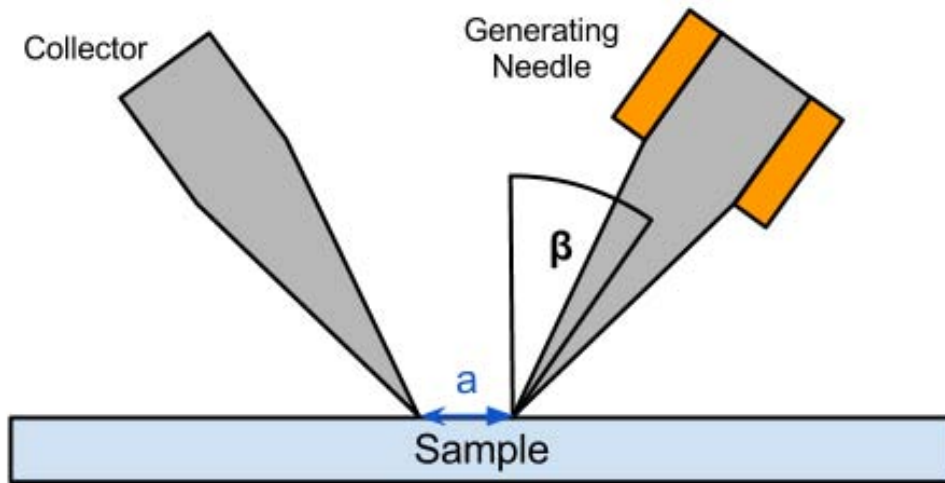
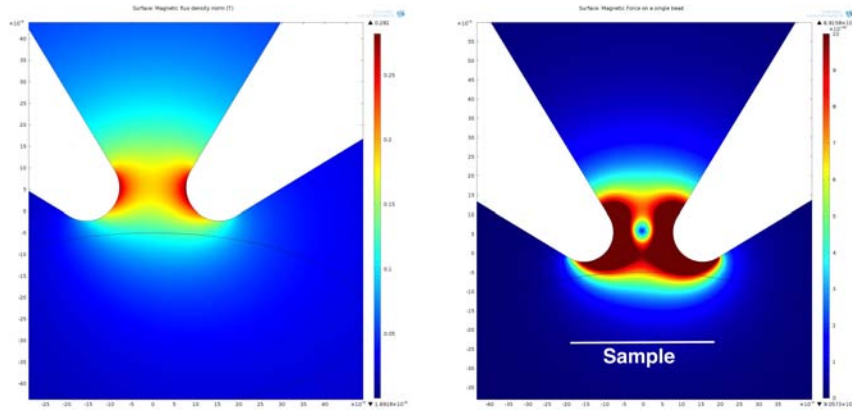


Figure 6.9: Magnetic Setup with a single collector. The first needle on the right side generates a magnetic field which is collected by the second non-generating needle. The tips of the needles are separated by distance a . Both needles are tilted at an angle β from the horizontal.

In order to observe the collector's influence on the magnetic field and forces, simulations were performed to calculate the magnetic field and magnetic force generated from the setup in Figure 6.9. In the simulation a numerically optimised EMN as proposed by Xiang *et al* [158] is implemented in COMSOL with the measures shown in Table 6.1. Unlike work performed in Xiang *et al* which optimized the needle geometry, this work chose to optimize the position and orientation of the needles relative to each other.



(a) COMSOL Simulation of the magnetic B-Field generated by a single EMN with a collector. The generating needle is on the right. High field strength is coloured red, low field strengths is coloured blue.

(b) COMSOL Simulation of the magnetic force acting on a single bead generated by an EMN with a collector. The generating needle is on the right. High forces are coloured red, low forces are coloured blue.

Figure 6.10: Simulation of the magnetic field and force generated by a single EMN and collector

The results of the simulation are shown in Figure 6.10a. The figure presents the absolute field strength. The absolute magnitude of force refers to the force that would act on a single magnetic bead. The second plot (Figure 6.10b) is a 2D plot of the forces generated by the setup. High and low forces and field strengths are coloured red and blue respectively. The threshold is chosen such that all forces above 1 nN are in dark red. These two plots offer a qualitative analysis of the fields and forces. Contrary to the earlier simulations using a single EMN, the field and force are not symmetrical about the maximum point. Even though the collector only acts passively, its field is similar to the field generated by the EMN. The collector is not merely absorbing the field, but acting like a second EMN. Also, the collector limits the distribution of the EMN field, as the field distribution on the left of the collector is significantly lower than the field distribution on the right of the EMN (shown in Figure 6.10a). Although the distribution area of the magnetic field becomes limited with a collector, the field strength and gradient is increased.

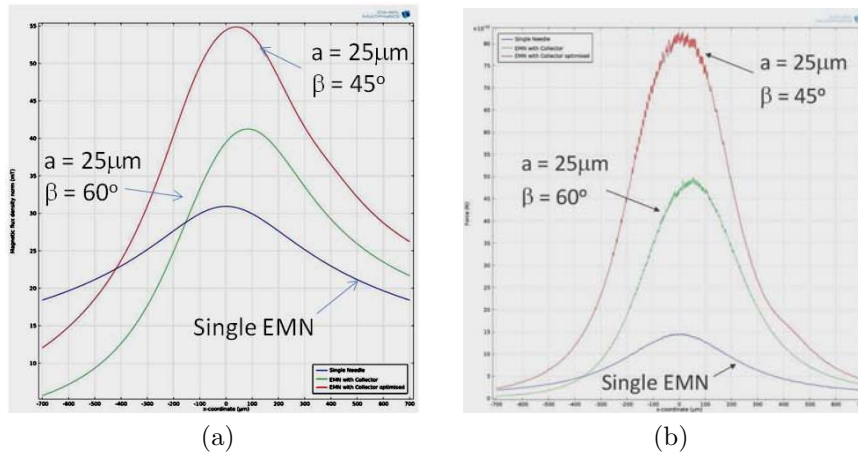


Figure 6.11: (a) Simulation of the magnetic field strength for 3 different setups along the sample (b) Simulation of the magnetic forces for 3 different setups along the sample

Figure 6.11a shows the magnetic field strength experienced by a bead at a point 250 μm away from the needle tip.

The graph contain three plots: The blue line is a reference field. This is generated by a single EMN with no collector. The green line indicates the field created by a collector and EMN at a distance 25 μm apart and at an angle of 60° to the vertical. Last but not least the red line represents a third setup which is a numerically optimised setup with one collector.

The field collector serve two purposes: First it increases the maximum field strength and second it increases the field gradient. Both effects lead to higher applicable magnetic forces.

The first significant difference between the setup with a collector and that of a single EMN without a collector can be observed between the green and the blue line. Even though the absolute field strength is only increased by 77% the force is increased by 460% as shown in Figure 6.11b. This effect occurs due to the collector which limits the field. Thus the gradient is much higher, resulting in a stronger force on the beads. As predicted the maximum force does not exist at the middle of the two tips, but it is shifted towards the EMN.

The position of the collector and EMN relative to each other (see Figure

6.9) is optimized to maximize the force and field obtained. While a single needle could generate $30.9mT$ in the sample the optimised setup generated a maximum field of $54.8mT$. Running the simulation to this data showed that the single EMN setup was able to exert forces of up to $14.6pN$ while an optimised collector setup was able to exert forces of up to $82.7pN$.

6.4 Experimental determination of magnetic fields and forces generated by electromagnetic needle

6.4.1 Electromagnetic needle

The electromagnetic needle (EMN) was designed and built in ETH, Switzerland. The EMN consists of a high magnetic permeability $12.7mm$ diameter Mu-metal core and 450 windings of insulated copper wire as shown in Figure 6.12a. To incorporate the EMN into the current confocal microscope, a holder was designed and printed using a 3D SLA printer as shown in Figure 6.12c. The final EMN together with the holder is shown in Figure 6.12c

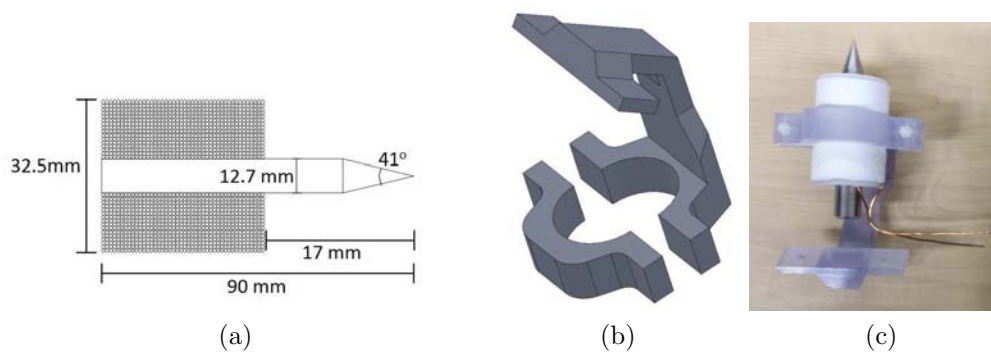


Figure 6.12: (a) Schematic design of the EMN. (b) CAD model of the EMN holder. (c) Actual image of EMN and holder.

6.4.2 Force calculation single EMN

An experimental setup was designed and built in order to measure the force generated by the EMN. The setup consists of a single microfluidic channel with the dimensions $100\ \mu\text{m}$ by $100\ \mu\text{m}$. Diluted particles were flowed through this channel. The particles under the influence of the magnetic field, reduce their velocity. In total two forces act on any particle: First the fluidic drag at a low Reynolds regime ($Re \approx 1.6 * 10^{-6}$) and second the magnetic forces in direction of the channel. [161]:

1. $F_{drag} = 6\pi\mu rv$

2. F_{mag}

Where r is the particle radius, μ the kinematic viscosity and v the velocity difference between particle and water.

The equation of motion for the particle is:

$$\frac{dw}{dt} = \frac{F_{mag} - F_{drag}}{m_p} \quad (6.11)$$

Where m_p is the particle mass and w the particles velocity

In order to determine the magnetic forces exerted on the particle a force equilibrium is considered. If particles are trapped such that the magnetic forces and the drag forces are in equilibrium, then the particles stop moving and the above equation is simplified to:

$$F_{mag} = 6\pi\mu rv \quad (6.12)$$

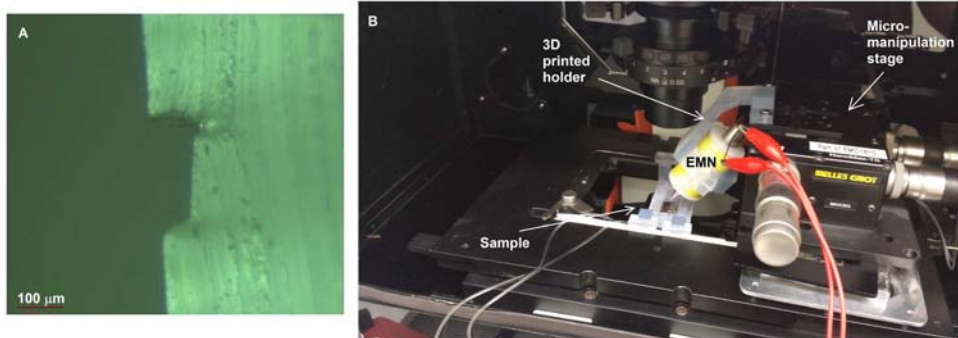
where v becomes the current velocity set at the inlet.

In this setup the velocity of the fluid can be controlled by a variable flowrate pump. A microfluidic channel was fabricated using standard soft lithography. The dimensions of the channel crosssection (shown in Figure 6.13a) were determined by a microscope. In order to use the electromagnetic needle in an existing microscope that is available in SMART BioSyM, a holder

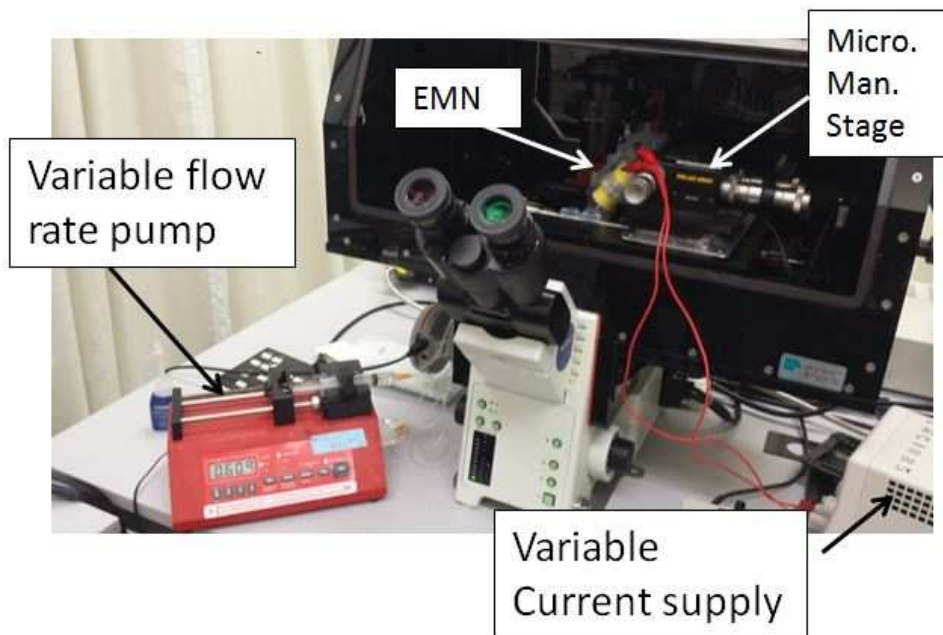
was designed and fabricated by a 3D SLA machine from SMART BioSyM. The final setup can be seen from Figure 6.13b.

The microscopic images shown in Figure 6.14a shows the flow of magnetic beads when the electromagnetic needle is turned off and Figure 6.14b shows the attraction of magnetic beads when the electromagnetic needle is turned on.

The velocity of the fluid was recorded when the forces were in equilibrium. Starting from high velocities the velocity was reduced until the particles were first trapped. After 5 trials, an average force of $F_{mag} = 15.0 \pm 1pN$ is obtained which is comparable with the simulated value of $F_{mag} = 19.6pN$.



(a) (A) Cross-section of microfluidic channel (B) Experimental setup



(b) Experimental setup for determining of magnetic forces on super paramagnetic beads

Figure 6.13: Experimental Setup

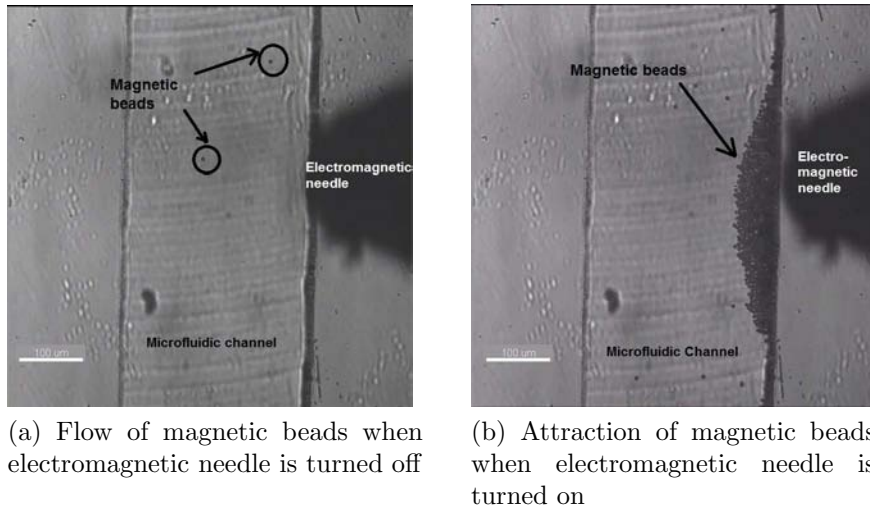


Figure 6.14: Microscopic images of super paramagnetic beads movement

6.4.3 Magnetic field mapping with microscopic hall sensor

Microscopic hall sensors, procured from Magcam (Figure 6.15), were used to characterize the magnetic field generated by the electromagnetic needles. The hall sensors have a $10\ \mu\text{m} \times 10\ \mu\text{m}$ sensing area and hence a high resolution map of the magnetic field can be analysed.

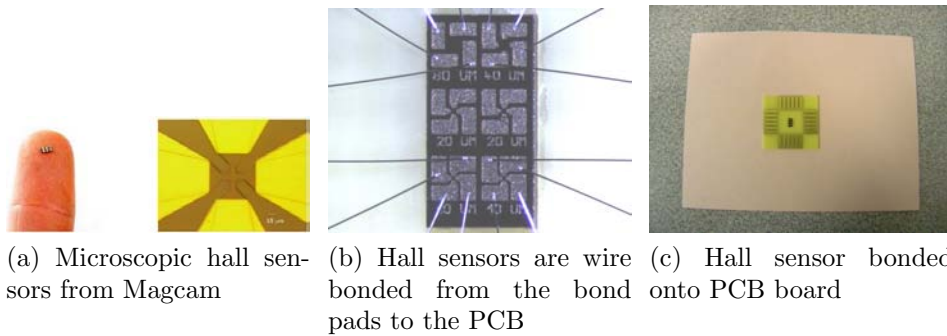


Figure 6.15: Microscopic hall sensors

In order to have the collector and EMN at a specific angle and distance, a holder was fabricated to contain both the collector and EMN as shown in Figure 6.16

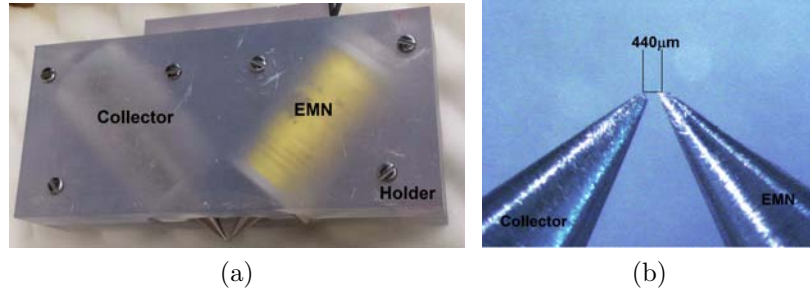


Figure 6.16: Electromagnetic needle holder containing both EMN and collector spaced $440\mu\text{m}$ apart and at angle of 50°

Figure 6.16 shows an EMN and collector held in place by a 3D printed holder. The angle of both the collector and EMN are 50° to the vertical and positioned such that their tips are $440\mu\text{m}$ apart. The resultant field is plotted by acquiring output data of the microscopic hall sensor across the needle tips as shown in the Figure 6.17.

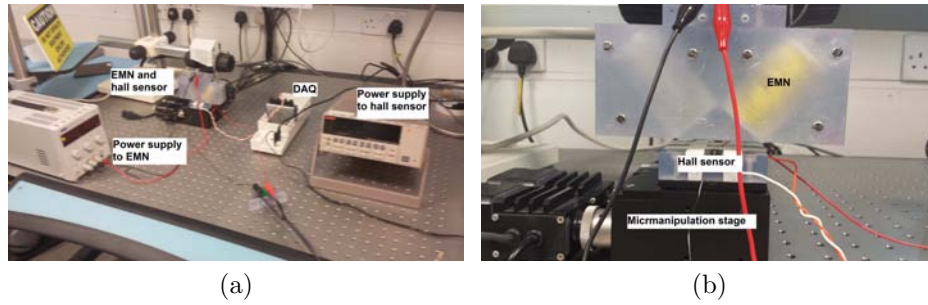


Figure 6.17: Hallsensor fixed onto a micromanipulation stage and moved in steps of $50\mu\text{m}$ at a distance of $700\mu\text{m}$ from the tip of the EMN and collector

Figure 6.17 shows the experimental setup for acquiring the hall sensor output data. The hall sensor is connected to a DAQ and the voltage output signal (V_H) is converted into magnetic field components (B) by the following conversion formula,

$$B = \frac{V_H - V_{off}}{I \times S} \quad (6.13)$$

Where V_{off} is the voltage from the sensor in the absence of magnetic field, I is the supply current and S is the sensitivity of the hall sensor according

to Figure 6.18.

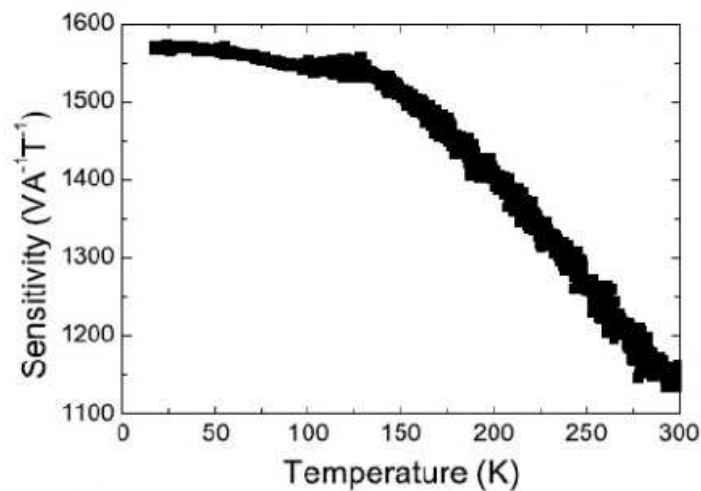


Figure 6.18: Sensitivity plot of microscopic hall sensor

By converting the hall sensor data into magnetic field magnitude, the surface plot of each configuration is plotted as shown in Figure 6.19

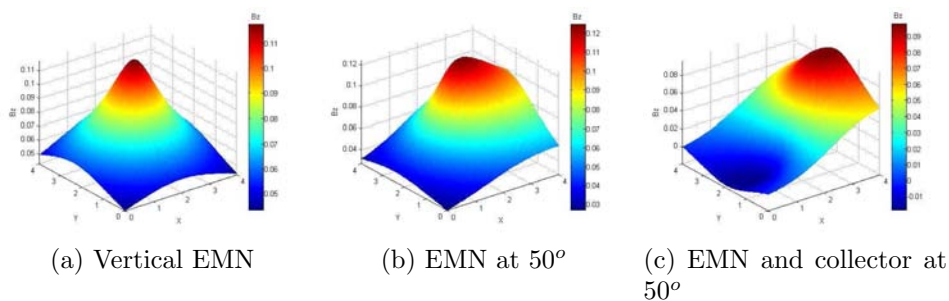


Figure 6.19: Surface plots of hall sensor data with different EMN and collector configurations. The height and colour of the plots correspond to the magnitude of the magnetic field

From the magnetic field data collected by the hall sensors, thresholding was done to determine how localised the magnetic field is with different configurations. The magnetic field threshold was kept at an arbitrary value of 0.095 tesla. The value for this threshold is considered arbitrary since it is only chosen to show the effect of localisation in different configurations of the EMN as shown in Figure 6.20.

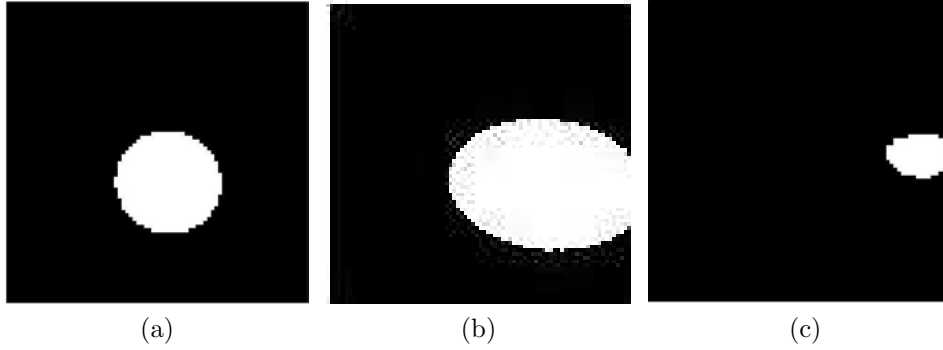


Figure 6.20: (a) Vertical EMN produced and area of $1.54mm^2$ threshold at a magnitude of $0.095T$, (b) EMN at 50° produced and area of $3.55mm^2$ threshold at a magnitude of $0.095T$, (c) EMN and collector at 50° produced and area of $0.40mm^2$ threshold at a magnitude of $0.095T$

From Figure 6.20, it can be seen that the EMN and the collector positioned at 50° to the vertical produced the most localised magnetic field with a minimal area of $0.40mm^2$. This shows that due to the presence of a collector, the field does not stray too far from the tip of the EMN as shown in Figure 6.20c. The EMN and collector configuration provides a possibility of localising the magnetic field hence being able to concentrate magnetic fields onto precise areas. With this approach, the capability of exerting magnetic forces accurately to trap and manipulate each individual magnetic beads, is improved. Furthermore the results from the hall sensor correspond with the COMSOL simulation results done in section 6.3.

6.5 Preliminary results of influencing HMVEC sprouting by changing local stiffness of ECM

The growth of microcapillaries which is also known as angiogenesis is involved in any biological processes such as growth and development, repair of wounds and increasing body mass. Endothelial cells (ECs) plays a key role in angiogenesis. The start of angiogenesis occurs when ECs detach from the main vascular wall and invade into the surrounding extracellular

matrix (ECM) as a vascular sprout as shown in Figure 6.21.

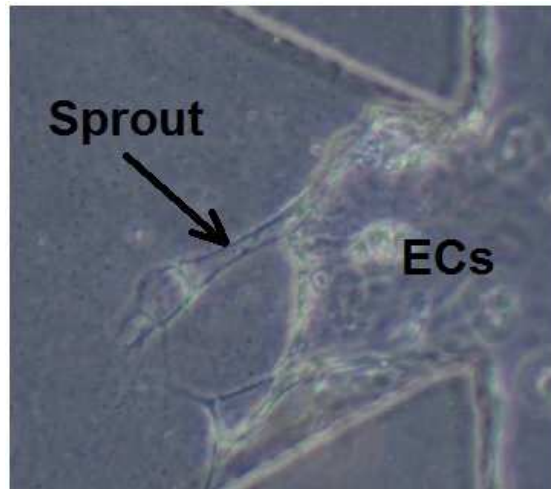


Figure 6.21: Example of endothelial sprouting

The abnormal growth of blood vessels leads to a variety of disorders such as arthritis and the growth and metastasis of tumors. Hence understanding the mechanisms of angiogenesis is important to the treatment of these pathologies. It is well known that many chemical growth factors affect EC sprouting such as vascular endothelial growth factors and Sphingosine-1-phosphate. However apart from chemical growth factors, the mechanical properties and the state of stress of the ECM has also shown to greatly influence endothelial sprouting and vascular network formation. [162] [163] [164] [165] [166]

In order to explore the effect of such states of stress in ECM for endothelial sprouting, the electromagnetic needle is used to exert forces on magnetic beads embedded in the ECM at the vicinity of sprouting endothelial cells in a microfluidic device as shown in Figure 6.22.

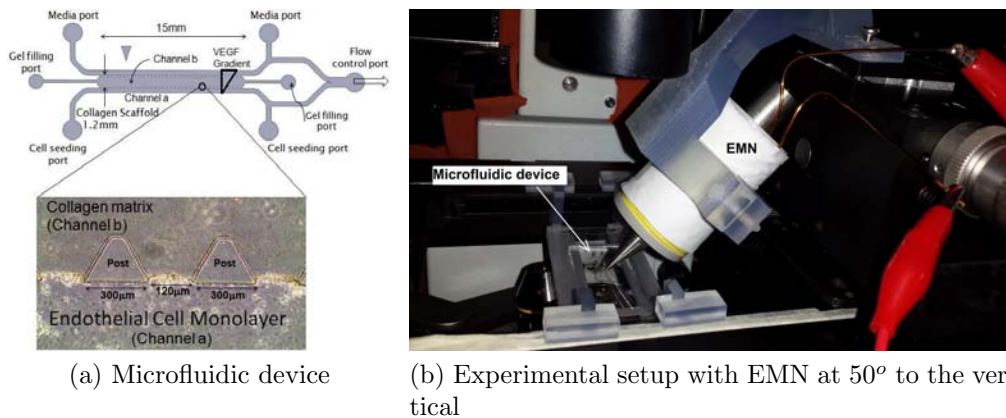


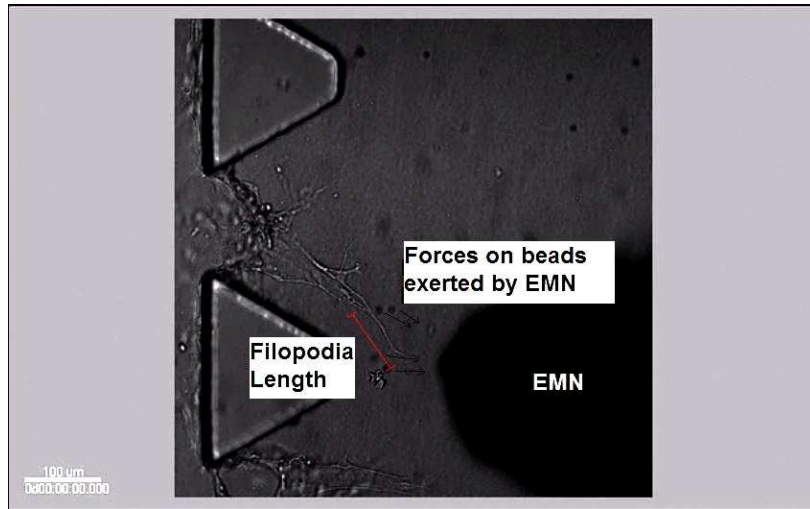
Figure 6.22: (a) Microfluidic device used for observation of HMVEC sprouting. (b) Experimental setup of endothelial cells and EMN in a confocal microscope installed together with an incubator

6.5.1 Results and discussion

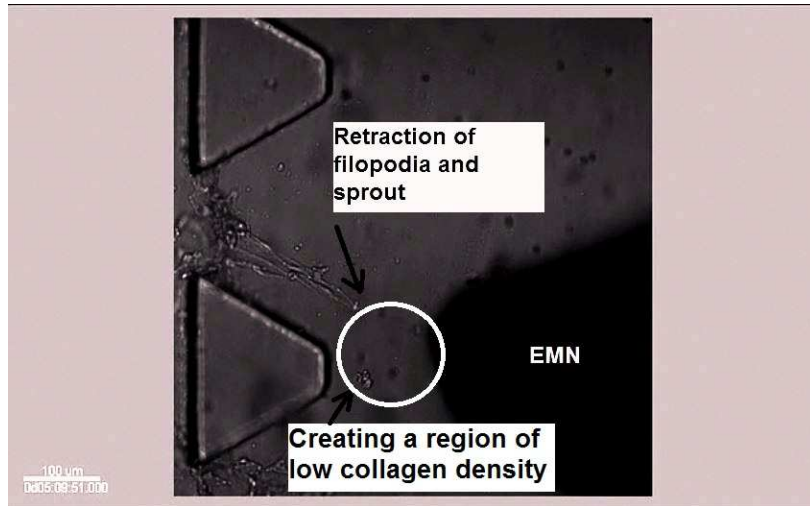
Preliminary results on a sprouting endothelial cell are shown in Figure 6.23. Although a VEGF gradient of 20-40 is introduced in the microfluidic device, results show that the sprouting endothelial cells retracted back into the monolayer. This shows that the forces exerted by the magnetic beads in the vicinity of the sprouting endothelial cells have created a less preferential condition for sprouting.

One reason for such a reaction could be due to the creation of a void in the collagen where the beads have displaced towards the electromagnetic needle. Since endothelial cells have been known to migrate preferentially in collagen rich areas, the reduction of collagen fibers could have triggered an inhibition to the protrusion and forward motion of the lumen.

The result presented in Figure 6.23 shows an effect in the sprouting behaviour of endothelial cells within 5 hours when external forces are exerted in their microenvironment. Although the results shown here are preliminary, it reflects the reaction of endothelial cells during angiogenesis. Further analysis and statistical observations are required to fully characterize the behaviour of sprouting endothelial cells in different stress states.



(a) Sprouting condition at the beginning of experiment



(b) Sprouting condition at end of experiment (after 5hrs)

Figure 6.23: Changes in sprouting HMVEC with magnetic forces within ECM exerted by electromagnetic needle

6.6 Concluding remarks

The work presented in this chapter demonstrated novel methods for generating micro magnetic fields. The functional principle of this method is based on an electro magnetic needle combined with field collector. The field collectors serve dual purposes: First they increase maximal field strength and second they increase the field gradient, both leading to higher applicable magnetic forces.

In the simulations the geometry of the EMN and the field collectors were optimised and the ideal setup parameters to generate magnetic fields were established. A setup that includes an EMN and collector was developed which could outperform a conventional EMN.

In addition an experimental setup which measures the forces exerted on specific beads by micro magnetic fields was designed, built and tested. In this setup the forces generated by the EMN from ETH Zurich were verified and compared to a COMSOL simulation.

After optimising the parameters for the EMN and collector, a final design was chosen. This had a single EMN combined with a collector, which was able to exert the highest forces onto magnetic micro particles.

Microscopic hall sensors were used to analyse the actual setups which included the EMN with and without the collector. The results were in close agreement with the COMSOL simulation. Both the simulation results and the experimental results verified that a combination of an EMN with a collector produced a more localised magnetic field to precisely manipulate single or a small group of magnetic beads.

Preliminary work with the EMN on endothelial sprouting within a modified ECM during angiogenesis has shown that exerting forces on the ECM through embedded magnetic beads caused a change in the sprouting behaviour. This provides the possibility of using EMNs and magnetic beads to externally influence the cellular behaviour such as migration, proliferation, apoptosis and differentiation.

Chapter 7

Conclusion

This work shows the possibility of altering the stiffness of the extracellular matrix (ECM) to influence cellular growth. At the macro scale, it has been shown that the uniaxial stiffness of the ECM can be altered actively to a significant degree by embedding (in the ECM) magnetic beads that are bio-conjugated with the collagen fibers and applying an external magnetic field as shown in Chapter 3. The application of an external magnetic field on a modified ECM sample creates a pre-tension in the collagen fibers which resists external deformations.

In Chapter 4 the local stiffness of the ECM was also investigated using an AFM, and an analytical model was developed to predict the change in the stiffness of such samples due to the influence of an external magnetic field. The experimental results have demonstrated that the binding between the embedded beads and the collagen fibres plays a significant role in altering the local stiffness of the ECM. This is due to the fact that beads attached to the fibers via bioconjugation create substantial additional resistance to deformation in the fibres when an external magnetic field is applied.

Due to these changes in stiffness at the macro and micro scale, the cellular behaviour of endothelial cells (ECs) have been significantly affected. When the magnetic field is present in a bead embedded collagen microfluidic device as described in Chapter 5, a bead located approximately 1.4 mm away from the permanent magnet is estimated to exert a force of 0.12 nN. Collectively such forces in general oppose the cell traction forces as ECs move away from the monolayer and into the collagen gel. This resistance can be considered as an increase in the apparent stiffness of the ECM in the vicinity of the migrating cells. The cells tend to migrate preferentially

in such an environment, since ECs are known to increase motility and spreading in areas with higher stiffness.

Chapter 6 demonstrated novel methods for generating micro magnetic fields. The magnetic field is generated by an electromagnetic needle (EMN). The propagation of the magnetic field is controlled by collectors. The field collectors serve two purposes: First they increase maximal field strength and second they increase the field gradient. Both effects lead to higher applicable magnetic forces.

The EMN was also used to exert point forces in the ECM and subsequent endothelial sprouting behaviour was observed. Preliminary results have shown that ECs have retracted from their original position during exposure to magnetic forces for 5 hours. Thus this method has shown the possibility of influencing angiogenesis by preventing further invasion of EC tip cells into the extracellular matrix along the direction of a higher VEGF signal.

7.1 Contribution

The contribution of this thesis is summarized as follows:

1. *Development and characterisation of a new platform for changing the extracellular matrix stiffness*

A new method was developed to alter the stiffness of modified ECM samples, in which the embedded superparamagnetic beads were coated with streptavidin to form strong covalent bonds with the ECM fibers. The macro-scale uniaxial stiffness of the modified ECM with a magnetic field perpendicular to the direction of a tensile force was characterised. A mechanical model of the ECM behaviour under uniaxial tension was established and validated with experimental stretch tests. The results showed that the macro-scale stiffness of the ECM could be increased by up to 59%. Also an innovative method to quantify the micro-scale change in stiffness of the modified ECM in the presence of a magnetic field was developed. This was done by using

a micro-indentation technique based on a Hertzian contact model. A customised device that could be easily integrated with an existing atomic force microscope was used to verify experimentally the changes in the micro-scale stiffness of the modified ECM. The results showed that the micro-scale stiffness could be increased by up to 25%. The difference between the changes of stiffness in micro-scale and macro-scale can be contributed to the highly structured heterogeneous property of the ECM.

2. *Study on the reaction of HMVEC sprouting during angiogenesis in the modified ECM*

An *in vitro* method was developed to study HMVEC sprouting during angiogenesis by using a microfluidic device containing modified ECM and under the influence of an external magnetic field. The experimental results thus obtained indicated that the change in stiffness of the ECM led to an increase of 56% in sprout height and 49% in the number of focal adhesions of sprouting HMVECs within the microfluidic device. Another technique for using an electromagnetic needle to exert point forces on magnetic beads embedded in a 3D ECM was developed. Observations of the reaction of HMVECs to these point forces in the 3D ECM point to the feasibility of this technique for practical application.

3. *Localisation of magnetic fields*

In order to exert controlled point forces on individual or a smaller group of magnetic beads in a microscopic region of interest, a new method was developed to generate stronger and more localized magnetic fields. This was achieved by utilising a novel combination of electromagnetic needles (EMN) and collectors. An in-depth simulation study, together with preliminary experimental results, has demonstrated the effectiveness of this method for more precise manipulation of individual (or a smaller group of) magnetic beads.

7.2 Future work

Further analysis of endothelial sprouting behaviour can be done and the underlying mechanisms for such behaviours can be further explored. This will also lead to the possibility of answering some of the key questions about the effect of external mechanical forces and the migration behaviour of different cell types due to mechanical signalling (Durotaxis).

The future prospects for the manipulation of magnetic beads in the extracellular matrix to influence sprouting comprises of:

- Statistically quantifying the amount of sprouting by carrying out systematic tests with controls and variables
- Tagging ECs with specific GFP biomarkers eg. vincullin, talin, paxillin which are all linked to the focal adhesions and good indicators of any changes occurring within the cell's microenvironment
- Using different types of microscopy (SEM, Reflectance, AFM etc) to identify the microscopic changes that occur within the ECM (collagen fiber orientation, collagen fiber density etc) when magnetic forces are exerted on the magnetic beads.
- Creating a vision system that is capable of analysing the relative cell movement and bead movement in the ECM to exert sizable forces on magnetic beads
- Incorporating the EMN with a collector design into existing microscope to allow a more localised force to be generated on the magnetic beads.
- Fully characterizing the size of forces that different combinations of EMN and collectors can exert on magnetic beads of different diameters.
- Establishing a method to observe the mechanism of filopodia extension and retraction when the local stiffness of the ECM is changed dynamically by the EMN and collector setup.

Publications

Journals

1. **Sahan C. B. Herath**, Yue Du, Dong-an Wang, Kin Liao, Qing-Guo Wang, Harry Asada, Peter C. Y. Chen, “Characterization of uniaxial stiffness of extracellular matrix embedded with magnetic beads via bio-conjugation and under the influence of an external magnetic field”, *Journal of the Mechanical Behaviour of Biomedical Materials*, vol. 30, pp. 253-265, 2014.
2. **Sahan C. B. Herath**, Yue Du, Shi Hui, Min-Cheol Kim, Dong-an Wang, Qing-Guo Wang, Krystyn J. Van Vliet, Harry Asada, and Peter C. Y. Chen, “Quantification of Magnetically Induced Changes in ECM Local Apparent Stiffness”, *Biophysical Journal*, vol. 106, No. 1, pp. 332-341, 2014.
3. Yue Du, **Sahan C. B. Herath**, Qing-Guo Wang, Harry Asada and Peter C. Y. Chen, “Analysis of Stiffness in Extracellular Matrix Embedded with Bio-conjugated Magnetic Beads in a Magnetic Field”, *International Journal of Bioscience, Biochemistry and Bioinformatics*, vol. 2, No. 5, pp. 329-335, 2012.
4. **Sahan C.B. Herath**, Sharghi Namini, Dong-an Wang, Harry Asada and Peter C. Y. Chen, “HMVEC Sprouting is Influenced by a Force Gradient Induced by Magnetic Beads Embedded in a Collagen Type-I Extracellular Matrix”, *To be submitted*.

Conferences

1. **Sahan Herath**, Sharghi Namini, Yue Du, Qing-Guo Wang, Dong-An Wang, Harry Asada, Peter Chen, 'Magnetically Manipulated ECM Stiffness Influences Vinculin Expression of Sprouting Human Microvascular Endothelial Cells', American Society for Cell Biology, Louisiana, USA, December 14-18, 2013.
2. Peter Chen, **Sahan Herath**, Dongan Wang, Su Kai, Liao Kin and Harry Asada, "Active Manipulation of ECM Stiffness", *Proceeding of 2011 International Conference of ASME Summer Bioengineering Conference*, Pennsylvania, USA, June 22-25, 2011.
3. Peter C. Y. Chen, **Sahan C.B. Herath**, Dong-an Wang and Harry Asada, "Active Manipulation of ECM Stiffness and Its Effect on Endothelial Cell Migration during Angiogenesis", *Proceeding of 2012 International Conference of Systems Biology and Bioengineering*, London, England, July 4-6, 2012.
4. Yue Du, **Sahan C. B. Herath**, Qing-Guo Wang, Harry Asada and Peter C. Y. Chen, "Analysis of Local Stiffness in ECM Embedded with Bioconjugated Magnetic Beads under the Influence of an External Magnetic Field," *Proceeding of 2012 International Conference on Biological and Life Sciences*, Singapore, July 23-24, 2012.
5. Yue Du, **Sahan C. B. Herath**, Qing-Guo Wang, Harry Asada and Peter C. Y. Chen, "Endothelial-cell-mediated Displacement of Extracellular Matrix during Angiogenesis", *Proceeding of 2012 International Conference on Applied Biomaterials and Biomechanics*, Bangkok, Thailand, December 22-23, 2012.

Appendix

1 Preparation of PEG coated magnetic beads

The coating on amine functionalised magnetic beads was applied via the following steps [167] [168] [169].

1. *Activation of PEG* — Dehydration of PEG was done by dissolving 6.03 grams of PEG in 150 ml toluene in a 3 neck flask from which 50 ml toluene/water micellar mixture was extracted by azeotropic distillation. The dehydrated PEG was then mixed with a catalyst, Triethylamine (TEA), in a 3 neck flask which was placed in salt-ice bath. 0.2 ml of Terephthaloyl chloride in 50 ml of anhydrous CH_2Cl_2 was poured into an equalised addition funnel and added dropwise into the 3 neck flask containing the PEG and TEA mixture. The reaction was carried out in an argon atmosphere. It was left for 1 hour in ice bath and for another 2 hours in room temperature. Magnetic stirring was maintained at 600 rpm throughout the reaction. After which the product was precipitated with 10-folds excess of ethyl ether. The powders were vacuum dried at room temperature in the dark.
2. *Coupling of PEG with magnetic beads* — The amine coated beads were washed with PBS thrice. Then 0.804 g of PEG was dissolved in 7.5 ml of 10 mM PBS (PH 7.4) and 0.5 ml of magnetic beads suspension. The final volume of the mixture was 9 ml. This reaction was carried out in an ice bath for 12 hrs and for another 12 hours in room temperature. Magnetic stirring at 600 rpm was maintained throughout the reaction.

3. *Zeta potential test* — The zeta potential measurement was carried out to ensure that coupling had occurred between the magnetic beads and PEG. Due to the charge shield effect of PEG, the results of the zeta potential test should show a lower value for the coupled beads compared to the amine coated beads. The beads were washed to change the solution from PBS to Deionised water prior to conducting the tests. The test results (as shown in Table 1) indicates a lower potential in the coupled PEG-bead solution compared to that in the solution of amine bead only. This indicates that PEG coupling had occurred for the amine coated beads.

Table 1: Zeta potential measurement

	No - PEG	PEG
Zeta Potential	41.2 ± 0.702 mV	12.8 ± 0.208 mV

2 Polyethylene glycol (PEG) coating

The amine coated magnetic beads were washed thrice with deionised water to remove the stock buffer solution. Then 1-ethyl-3-(3-dimethylaminopropyl) carbodiimide (EDC) and N-hydroxysuccinimide (NHS) in the ratio of 5:1 were mixed for 30 minutes to activate the coupling group. Once this was done, the EDC and NHS mixture, amine coated beads and PEG were added in the ratio of 1:1:2, respectively. For successful cross-linking between Polyethylene glycol (PEG) and Amine-coated beads to occur, this mixture was left for 24 hours on a vibrating platform. To check whether the PEG had successfully bound onto the Amine-coated magnetic beads, FTIR analysis was carried out. Figure 1 shows the results of the FTIR analysis.

Figure 1 reveals that narrow peaks were formed at wave number of 1100 cm^{-1} , 1600 cm^{-1} and 1500 cm^{-1} . It can thus be concluded that (i) due to the peak forming at 1100 cm^{-1} , a c-o-c ether group was present, (ii) due to the peak at 1600 cm^{-1} , a primary amide group of the bond was present,

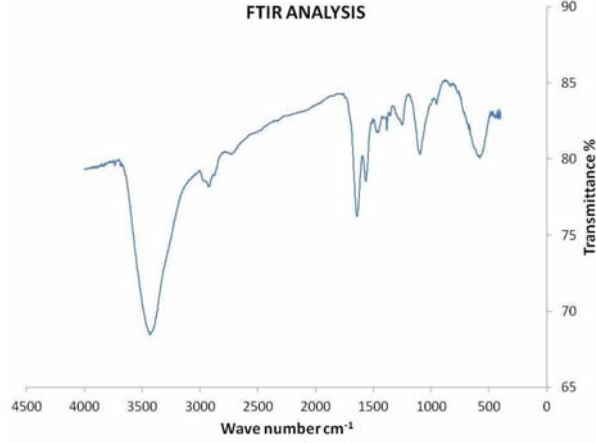


Figure 1: FTIR analysis for PEG coating of magnetic beads.

and (iii) due to the peak at 1500 cm^{-1} , a secondary amide group of the bond was present.

These results indicate that PEG was present in the sample due to the presence of a c-o-c ether group. Also the presence of primary amide group of the bonds between PEG and the amine functionalised beads, and secondary amide group of the bonds between PEG and the amine functionalised beads, showed that successful coupling between the magnetic beads and PEG had occurred.

3 Magnetic force

The magnetic field along the x -axis (as is indicated in Figure 4.6(a)) for a cuboid permanent magnet is given by [113]

$$B_x(d_x) = \frac{B_r}{\pi} \left[\tan^{-1} \left(\frac{ab}{2d_x \sqrt{4d_x^2 + \varphi_1}} \right) - \tan^{-1} \left(\frac{ab}{2\varphi_2 \sqrt{4\varphi_2^2 + \varphi_1}} \right) \right], \quad (1)$$

where B_r is the residual induction, $\varphi_1 = a^2 + b^2$, $\varphi_2 = c + d_x$, d_x is the distance in the x -direction of a point from the magnet, and a , b and c are the height, width and thickness of the permanent magnet, respectively.

Figure 2a shows a plot of the magnetic field along the x -axis generated using

Equation (1). By considering each bead as the point of origin, the magnetic forces acting on a group of randomly distributed beads are calculated using the expression $F = m (\nabla B_x(d_x))$, where $m = \eta HV$ is the magnetic moment of a bead, with $\eta = 5240 \text{ kg/m}^3$ being the density of iron oxide, H the induced auxiliary magnetic field, and V the volume of a single bead (with a radius of $1 \text{ }\mu\text{m}$).

Thus for the experiment setup as described in Section 4.2, a bead 4 mm away from the magnet will experience a magnetic field of $B = 0.05 \text{ T}$. Based on the magnetization curve (shown in Figure 3) for the beads used in this experiment, it can be concluded that the magnetization of such a bead is not saturated, and that the bead has an induced auxiliary magnetic field of $H = 40 \text{ emu/g}$. For the magnet used in our experiment, we have $a = b = c = 4 \text{ mm}$ and $B_r = 1.5\text{T}$. Hence for a single bead located at a distance of $d_x = 4 \text{ mm}$ away from the magnet the force acting on the bead is approximately 28 pN.

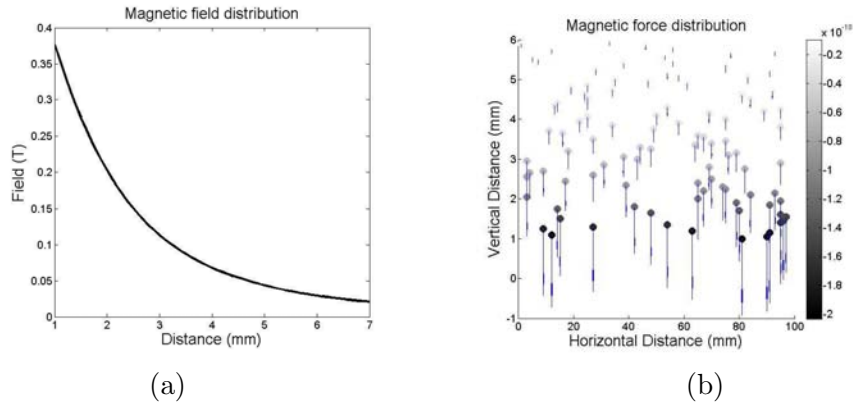


Figure 2: (a) Simulated magnetic field (b) Magnetic forces acting on beads. The length of arrows and the gray level of the points indicate the magnitude and direction of the force exerted on individual beads.

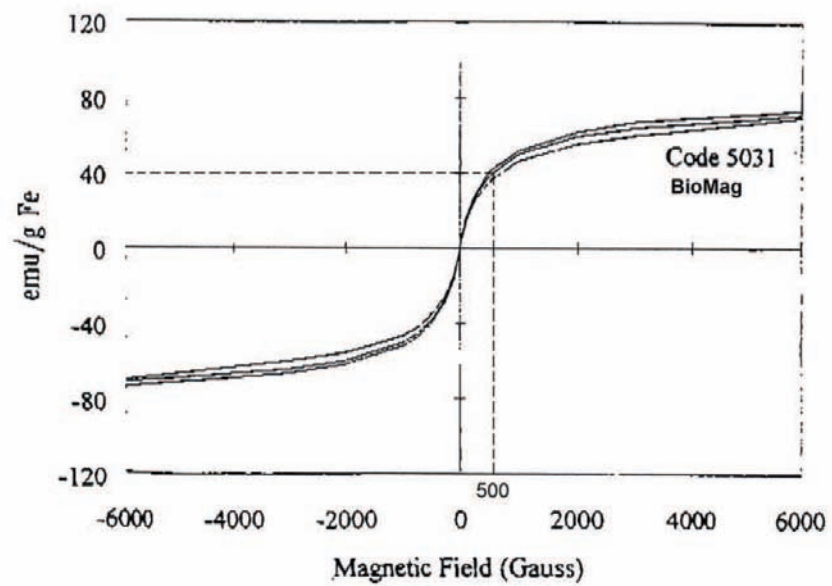
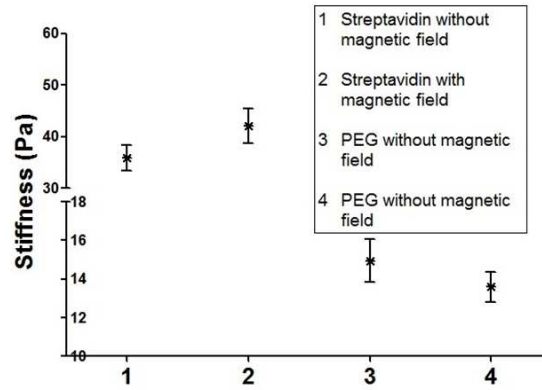
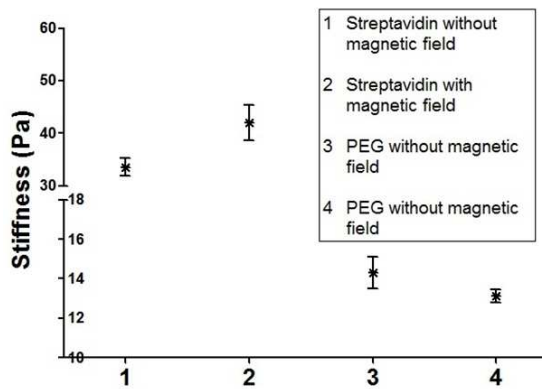


Figure 3: Magnetization of BioMag particles. (Adapted from figure provided by Bangs Laboratory, Inc., U.S.A.)

4 Modified Thompson- τ test



(a)



(b)

Figure 4: Results of statistical analysis using the modified Thompson- test. The asterisk indicates the mean and the two horizontal lines above and below the asterisk indicate the Standard Error of the Mean (SEM). When the outliers in the data as presented in (a) are excluded, data scattering is reduced due to the smaller standard deviation (not shown) and the relevant difference between the means in all cases increases as shown in (b). The reduced SEM in (b) further indicates that the sample mean thus obtained is a better estimate of the actual stiffness of the ECM for all cases.

Bibliography

- [1] Frederick H Silver, Joseph W Freeman, and Gurinder P Seehra. Collagen self-assembly and the development of tendon mechanical properties. *Journal of biomechanics*, 36(10):1529–1553, 2003.
- [2] Peter Fratzl, Klaus Misof, Ivo Zizak, Gert Rapp, Heinz Amenitsch, and Sigrid Bernstorff. Fibrillar structure and mechanical properties of collagen. *Journal of structural biology*, 122(1):119–122, 1998.
- [3] Andrew J Maniotis, Christopher S Chen, and Donald E Ingber. Demonstration of mechanical connections between integrins, cytoskeletal filaments, and nucleoplasm that stabilize nuclear structure. *Proceedings of the National Academy of Sciences*, 94(3):849–854, 1997.
- [4] Christopher B Raub, Vinod Suresh, Tatiana Krasieva, Julia Lyubovitsky, Justin D Mih, Andrew J Putnam, Bruce J Tromberg, and Steven C George. Noninvasive assessment of collagen gel microstructure and mechanics using multiphoton microscopy. *Biophysical Journal*, 92(6):2212–2222, 2007.
- [5] David L Christiansen, Eric K Huang, and Frederick H Silver. Assembly of type i collagen: fusion of fibril subunits and the influence of fibril diameter on mechanical properties. *Matrix Biology*, 19(5):409–420, 2000.
- [6] Robert S Fischer, Margaret Gardel, Xuefei Ma, Robert S Adelstein, and Clare M Waterman. Local cortical tension by myosin ii guides 3d endothelial cell branching. *Current Biology*, 19(3):260–265, 2009.
- [7] *Cell Migration*. 2011. <http://www.cellmigration.org>.

- [8] Nina Tymchenko, Jonas Wallentin, Sarunas Petronis, LM Bjursten, Bengt Kasemo, and Julie Gold. A novel cell force sensor for quantification of traction during cell spreading and contact guidance. *Biophysical journal*, 93(1):335–345, 2007.
- [9] Zhaochun Yang, Jeen-Shang Lin, Jianxin Chen, and James HC Wang. Determining substrate displacement and cell traction fields a new approach. *Journal of theoretical biology*, 242(3):607–616, 2006.
- [10] Charlie Gosse and Vincent Croquette. Magnetic tweezers: micromanipulation and force measurement at the molecular level. *Biophysical journal*, 82(6):3314–3329, 2002.
- [11] Philip Kollmannsberger and Ben Fabry. High-force magnetic tweezers with force feedback for biological applications. *Review of Scientific Instruments*, 78(11):114301–114301, 2007.
- [12] Robert J Pelham and Yu-li Wang. Cell locomotion and focal adhesions are regulated by substrate flexibility. *Proceedings of the National Academy of Sciences*, 94(25):13661–13665, 1997.
- [13] Michael P Sheetz, Dan P Felsenfeld, and Catherine G Galbraith. Cell migration: regulation of force on extracellular-matrix-integrin complexes. *Trends in cell biology*, 8(2):51–54, 1998.
- [14] Chun-Min Lo, Hong-Bei Wang, Micah Dembo, and Yu-li Wang. Cell movement is guided by the rigidity of the substrate. *Biophysical journal*, 79(1):144–152, 2000.
- [15] Richard K Assoian and Eric A Klein. Growth control by intracellular tension and extracellular stiffness. *Trends in cell biology*, 18(7):347–352, 2008.
- [16] Dennis P McDaniel, Gordon A Shaw, John T Elliott, Kiran Bhadri-raj, Curt Meuse, Koo-Hyun Chung, and Anne L Plant. The stiffness of collagen fibrils influences vascular smooth muscle cell phenotype. *Biophysical journal*, 92(5):1759–1769, 2007.
- [17] Rebecca G Wells. The role of matrix stiffness in regulating cell behavior. *Hepatology*, 47(4):1394–1400, 2008.

- [18] Revathi Ananthakrishnan and Allen Ehrlicher. The forces behind cell movement. *International journal of biological sciences*, 3(5):303, 2007.
- [19] Karl Kadler. Extracellular matrix. 1: fibril-forming collagens. *Protein profile*, 1(5):519–638, 1993.
- [20] Yu-Long Sun, Zong-Ping Luo, Andrzej Fertala, and Kai-Nan An. Direct quantification of the flexibility of type i collagen monomer. *Biochemical and biophysical research communications*, 295(2):382–386, 2002.
- [21] V Ottani, D Martini, M Franchi, A Ruggeri, and M Raspanti. Hierarchical structures in fibrillar collagens. *Micron*, 33(7):587–596, 2002.
- [22] R Puxkandl, I Zizak, O Paris, J Keckes, W Tesch, S Bernstorff, P Purslow, and P Fratzl. Viscoelastic properties of collagen: synchrotron radiation investigations and structural model. *Philosophical Transactions of the Royal Society of London. Series B: Biological Sciences*, 357(1418):191–197, 2002.
- [23] Anton V Persikov, John AM Ramshaw, Alan Kirkpatrick, and Barbara Brodsky. Amino acid propensities for the collagen triple-helix. *Biochemistry*, 39(48):14960–14967, 2000.
- [24] Lei Huang, Karthik Nagapudi, Robert P. Apkarian, and Elliot L Chaikof. Engineered collagen–peo nanofibers and fabrics. *Journal of Biomaterials Science, Polymer Edition*, 12(9):979–993, 2001.
- [25] Rachel Z Kramer, Manju G Venugopal, Jordi Bella, Patricia Mayville, Barbara Brodsky, and Helen M Berman. Staggered molecular packing in crystals of a collagen-like peptide with a single charged pair. *Journal of molecular biology*, 301(5):1191–1205, 2000.
- [26] DJ Hulmes, Tim J Wess, Darwin J Prockop, and Peter Fratzl. Radial packing, order, and disorder in collagen fibrils. *Biophysical Journal*, 68(5):1661–1670, 1995.

- [27] AJ Hodge and JA Petruska. Recent studies with the electron microscope on ordered aggregates of the tropocollagen molecule. *Aspects of protein structure*, pages 289–300, 1963.
- [28] TJ Wess, AP Hammersley, L Wess, and A Miller. A consensus model for molecular packing of type i collagen. *Journal of structural biology*, 122(1):92–100, 1998.
- [29] JW Smith. Molecular pattern in native collagen. *Nature*, 219:157–158, 1968.
- [30] David JS Hulmes and Andrew Miller. Quasi-hexagonal molecular packing in collagen fibrils. 1979.
- [31] Benedicto de Campos Vidal. Image analysis of tendon helical superstructure using interference and polarized light microscopy. *Micron*, 34(8):423–432, 2003.
- [32] PETER P Purslow, TJ Wess, and DW Hukins. Collagen orientation and molecular spacing during creep and stress-relaxation in soft connective tissues. *The Journal of Experimental Biology*, 201(1):135–142, 1998.
- [33] Paris O Keckes J Tesch W Bernstorff S Purslow P Fratzl P Puxkandl R, Zizak I. Viscoelastic properties of collagen: synchrotron radiation investigations and structural model. *Phil. Trans. R. Soc. Lond.*, 357:191–197, 2002.
- [34] Ingomar Jäger and Peter Fratzl. Mineralized collagen fibrils: a mechanical model with a staggered arrangement of mineral particles. *Biophysical Journal*, 79(4):1737–1746, 2000.
- [35] HRC Screen, DA Lee, DL Bader, and JC Shelton. An investigation into the effects of the hierarchical structure of tendon fascicles on micromechanical properties. *Proceedings of the Institution of Mechanical Engineers, Part H: Journal of Engineering in Medicine*, 218(2):109–119, 2004.

- [36] RK Hansen and MJ Bissell. Tissue architecture and breast cancer: the role of extracellular matrix and steroid hormones. *Endocrine-related cancer*, 7(2):95–113, 2000.
- [37] John McNeish. Embryonic stem cells in drug discovery. *Nature Reviews Drug Discovery*, 3(1):70–80, 2004.
- [38] Pascale V Guillot, Wei Cui, Nicholas M Fisk, and Dame Julia Polak. Stem cell differentiation and expansion for clinical applications of tissue engineering. *Journal of cellular and molecular medicine*, 11(5):935–944, 2007.
- [39] Tenneille E Ludwig, Veit Bergendahl, Mark E Levenstein, Junying Yu, Mitchell D Probasco, and James A Thomson. Feeder-independent culture of human embryonic stem cells. *Nature methods*, 3(8):637–646, 2006.
- [40] Jean Lu, Runhua Hou, Carmen Jane Booth, Shih-Hung Yang, and Michael Snyder. Defined culture conditions of human embryonic stem cells. *Proceedings of the National Academy of Sciences*, 103(15):5688–5693, 2006.
- [41] Yoav Soen, Akiko Mori, Theo D Palmer, and Patrick O Brown. Exploring the regulation of human neural precursor cell differentiation using arrays of signaling microenvironments. *Molecular systems biology*, 2(1), 2006.
- [42] Masafumi Nakajima, Toshinari Ishimuro, Koichi Kato, In-Kap Ko, Isao Hirata, Yusuke Arima, and Hiroo Iwata. Combinatorial protein display for the cell-based screening of biomaterials that direct neural stem cell differentiation. *Biomaterials*, 28(6):1048–1060, 2007.
- [43] Albert J Keung, Sanjay Kumar, and David V Schaffer. Presentation counts: microenvironmental regulation of stem cells by biophysical and material cues. *Annual review of cell and developmental biology*, 26:533–556, 2010.
- [44] Yasuhiro Sawada, Masako Tamada, Benjamin J Dubin-Thaler, Oksana Cherniavskaya, Ryuichi Sakai, Sakae Tanaka, and Michael P

- Sheetz. Force sensing by mechanical extension of the src family kinase substrate p130cas. *Cell*, 127(5):1015–1026, 2006.
- [45] RL Duncan and CH Turner. Mechanotransduction and the functional response of bone to mechanical strain. *Calcified tissue international*, 57(5):344–358, 1995.
- [46] I Komuro, Youichi Katoh, Toshikazu Kaida, Yoshikazu Shibasaki, Masahiko Kurabayashi, Eitetsu Hoh, Fumimaro Takaku, and Yoshio Yazaki. Mechanical loading stimulates cell hypertrophy and specific gene expression in cultured rat cardiac myocytes. possible role of protein kinase c activation. *Journal of Biological Chemistry*, 266(2):1265–1268, 1991.
- [47] Matthias Chiquet, Ana Sarasa Renedo, François Huber, and Martin Flück. How do fibroblasts translate mechanical signals into changes in extracellular matrix production? *Matrix Biology*, 22(1):73–80, 2003.
- [48] Uday Chippada, Bernard Yurke, Penelope C Georges, and Noshir A Langrana. A nonintrusive method of measuring the local mechanical properties of soft hydrogels using magnetic microneedles. *Journal of biomechanical engineering*, 131(2):021014–021014, 2009.
- [49] Francis J Alenghat, Ben Fabry, Kenneth Y Tsai, Wolfgang H Goldmann, and Donald E Ingber. Analysis of cell mechanics in single vinculin-deficient cells using a magnetic tweezer. *Biochemical and biophysical research communications*, 277(1):93–99, 2000.
- [50] Andreas R Bausch, Florian Ziemann, Alexei A Boulbitch, Ken Jacobson, and Erich Sackmann. Local measurements of viscoelastic parameters of adherent cell surfaces by magnetic bead microrheometry. *Biophysical Journal*, 75(4):2038–2049, 1998.
- [51] Benjamin D Matthews, David A LaVan, Darryl R Overby, John Karavitis, and Donald E Ingber. Electromagnetic needles with submicron pole tip radii for nanomanipulation of biomolecules and living cells. *Applied Physics Letters*, 85(14):2968–2970, 2004.

- [52] Anthony HB de Vries, Bea E Krenn, Roel van Driel, and Johannes S Kanger. Micro magnetic tweezers for nanomanipulation inside live cells. *Biophysical journal*, 88(3):2137–2144, 2005.
- [53] FHC Crick and AFW Hughes. The physical properties of cytoplasm: A study by means of the magnetic particle method part i. experimental. *Experimental Cell Research*, 1(1):37–80, 1950.
- [54] Steven B Smith, Laura Finzi, and Carlos Bustamante. Direct mechanical measurements of the elasticity of single dna molecules by using magnetic beads. *Science*, 258(5085):1122–1126, 1992.
- [55] TR Strick, JF Allemand, D Bensimon, A Bensimon, and V Croquette. The elasticity of a single supercoiled dna molecule. *SCIENCE-NEW YORK THEN WASHINGTON-*, pages 1835–1837, 1996.
- [56] Shaw-Ruey Lyu, Jeh-En Tzeng, Chia-Yuan Kuo, Ai-Ru Jian, and De-Shin Liu. Mechanical strength of mediopatellar plica—the influence of its fiber content. *Clinical Biomechanics*, 21(8):860–863, 2006.
- [57] Valerie I Walters, Albert L Kwansa, and Joseph W Freeman. Design and analysis of braid-twist collagen scaffolds. *Connective tissue research*, 53(3):255–266, 2012.
- [58] BP Chan, TY Hui, OCM Chan, K-F So, W Lu, KMC Cheung, E Salomatina, and A Yaroslavsky. Photochemical cross-linking for collagen-based scaffolds: a study on optical properties, mechanical properties, stability, and hemocompatibility. *Tissue engineering*, 13(1):73–85, 2007.
- [59] Ratchada Sopakayang, Raffaella De Vita, Albert Kwansa, and Joseph W Freeman. Elastic and viscoelastic properties of a type i collagen fiber. *Journal of Theoretical Biology*, 293:197–205, 2012.
- [60] Ludwig T., R. Kirmse, K. Poole, and U. S. Schwarz. Probing cellular microenvironments and tissue remodeling by atomic force microscopy. *Pflügers Archiv-European Journal of Physiology*, 456(1):29–49, 2008.

- [61] Alonso J. L. and W. H. Goldmann. Feeling the forces: atomic force microscopy in cell biology. *Life sciences*, 72(23):2553–2560, 2003.
- [62] Lin D. C., E. K. Dimitriadis, F. Horkay, et al. Robust strategies for automated afm force curve analysis-i. non-adhesive indentation of soft, inhomogeneous materials. *Transactions-American Society of Mechanical Engineers Journal of Biomechanical Engineering*, 129(3):430, 2007.
- [63] Stolz M., R. Raiteri, A. U. Daniels, M. R. VanLandingham, W. Baschong, and U. Aebi. Dynamic elastic modulus of porcine articular cartilage determined at two different levels of tissue organization by indentation-type atomic force microscopy. *Biophysical Journal*, 86(5):3269–3283, 2004.
- [64] Natalie DeWitt. Angiogenesis. *Nature*, 438(7070):931–931, 2005.
- [65] Anneli Ny, Marta Koch, Martin Schneider, Elke Neven, Ricky T Tong, Sunit Maity, Christian Fischer, Stephane Plaisance, Diether Lambrechts, Christophe Héligon, et al. A genetic xenopus laevis tadpole model to study lymphangiogenesis. *Nature medicine*, 11(9):998–1004, 2005.
- [66] Michael Simons. Angiogenesis where do we stand now? *Circulation*, 111(12):1556–1566, 2005.
- [67] Peter Carmeliet. Angiogenesis in life, disease and medicine. *Nature*, 438(7070):932–936, 2005.
- [68] Brian P Eliceiri, Robert Paul, Pamela L Schwartzberg, John D Hood, Jie Leng, and David A Cheresh. Selective requirement for src kinases during vegf-induced angiogenesis and vascular permeability. *Molecular cell*, 4(6):915–924, 1999.
- [69] Gavin Thurston, John S Rudge, Ella Ioffe, Hao Zhou, Leorah Ross, Susan D Croll, Nicole Glazer, Jocelyn Holash, Donald M McDonald, and George D Yancopoulos. Angiopoietin-1 protects the adult vasculature against plasma leakage. *Nature medicine*, 6(4):460–463, 2000.

- [70] Nicholas W Gale and George D Yancopoulos. Growth factors acting via endothelial cell-specific receptor tyrosine kinases: Vegfs, angiopoietins, and ephrins in vascular development. *Genes & development*, 13(9):1055–1066, 1999.
- [71] Peter C Maisonpierre, Chitra Suri, Pamela F Jones, Sona Bartunkova, Stanley J Wiegand, Czeslaw Radziejewski, Debra Compton, Joyce McClain, Thomas H Aldrich, Nick Papadopoulos, et al. Angiopoietin-2, a natural antagonist for tie2 that disrupts in vivo angiogenesis. *Science*, 277(5322):55–60, 1997.
- [72] Lisa M Coussens, Wilfred W Raymond, Gabriele Bergers, Marion Laig-Webster, Ole Behrendtsen, Zena Werb, George H Caughey, and Douglas Hanahan. Inflammatory mast cells up-regulate angiogenesis during squamous epithelial carcinogenesis. *Genes & development*, 13(11):1382–1397, 1999.
- [73] Napoleone Ferrara. Role of vascular endothelial growth factor in the regulation of angiogenesis. *Kidney international*, 56(3):794–814, 1999.
- [74] Jussi Taipale, T Makinen, Elena Arighi, Eola Kukk, M Karkkainen, and Kari Alitalo. Vascular endothelial growth factor receptor-3. In *Vascular Growth Factors and Angiogenesis*, pages 85–96. Springer, 1999.
- [75] Shay Soker, Seiji Takashima, Hua Quan Miao, Gera Neufeld, and Michael Klagsbrun. Neuropilin-1 is expressed by endothelial and tumor cells as an isoform-specific receptor for vascular endothelial growth factor. *Cell*, 92(6):735–745, 1998.
- [76] Toyoaki Murohara, Takayuki Asahara, Marcy Silver, Christophe Bauters, Haruchika Masuda, Christoph Kalka, Marianne Kearney, Donghui Chen, JF Symes, MC Fishman, et al. Nitric oxide synthase modulates angiogenesis in response to tissue ischemia. *Journal of Clinical Investigation*, 101(11):2567, 1998.
- [77] Wolfgang Schaper. Collateral vessel growth in the human heart role of fibroblast growth factor-2. *Circulation*, 94(4):600–601, 1996.

- [78] C Sunderkötter, K Steinbrink, M Goebeler, RANJIT Bhardwaj, and C Sorg. Macrophages and angiogenesis. *Journal of Leukocyte Biology*, 55(3):410–422, 1994.
- [79] Harold F Dvorak. How tumors make bad blood vessels and stroma. *The American journal of pathology*, 162(6):1747, 2003.
- [80] Peter Baluk, Hiroya Hashizume, and Donald M McDonald. Cellular abnormalities of blood vessels as targets in cancer. *Current opinion in genetics & development*, 15(1):102–111, 2005.
- [81] Chang-Geol Lee, Marcus Heijn, Emmanuelle di Tomaso, Genevieve Griffon-Etienne, M Ancukiewicz, Chieko Koike, KR Park, Napoleone Ferrara, Rakesh K Jain, Herman D Suit, et al. Anti-vascular endothelial growth factor treatment augments tumor radiation response under normoxic or hypoxic conditions. *Cancer Research*, 60(19):5565–5570, 2000.
- [82] Paxton V Dickson, John B Hamner, Thomas L Sims, Charles H Fraga, Catherine YC Ng, Surender Rajasekeran, Nikolaus L Hagedorn, M Beth McCarville, Clinton F Stewart, and Andrew M Davidoff. Bevacizumab-induced transient remodeling of the vasculature in neuroblastoma xenografts results in improved delivery and efficacy of systemically administered chemotherapy. *Clinical Cancer Research*, 13(13):3942–3950, 2007.
- [83] Daniela E Fuentes and Peter J Butler. Coordinated mechanosensitivity of membrane rafts and focal adhesions. *Cellular and molecular bioengineering*, 5(2):143–154, 2012.
- [84] Sanjay Kumar, Iva Z Maxwell, Alexander Heisterkamp, Thomas R Polte, Tanmay P Lele, Matthew Salanga, Eric Mazur, and Donald E Ingber. Viscoelastic retraction of single living stress fibers and its impact on cell shape, cytoskeletal organization, and extracellular matrix mechanics. *Biophysical journal*, 90(10):3762–3773, 2006.
- [85] Kaustabh Ghosh, Zhi Pan, E Guan, Shouren Ge, Yajie Liu, Toshio Nakamura, Xiang-Dong Ren, Miriam Rafailovich, and Richard AF

- Clark. Cell adaptation to a physiologically relevant ecm mimic with different viscoelastic properties. *Biomaterials*, 28(4):671–679, 2007.
- [86] Donald E Ingber. Tensegrity ii. how structural networks influence cellular information processing networks. *Journal of Cell Science*, 116(8):1397–1408, 2003.
- [87] Kaustabh Ghosh, Charles K Thodeti, Andrew C Dudley, Akiko Mamamoto, Michael Klagsbrun, and Donald E Ingber. Tumor-derived endothelial cells exhibit aberrant rho-mediated mechanosensing and abnormal angiogenesis in vitro. *Proceedings of the National Academy of Sciences*, 105(32):11305–11310, 2008.
- [88] Kevin D Costa, William J Hucker, and Frank C-P Yin. Buckling of actin stress fibers: a new wrinkle in the cytoskeletal tapestry. *Cell motility and the cytoskeleton*, 52(4):266–274, 2002.
- [89] Shuqi Chen and Timothy A Springer. Selectin receptor–ligand bonds: Formation limited by shear rate and dissociation governed by the bell model. *Proceedings of the National Academy of Sciences*, 98(3):950–955, 2001.
- [90] Christophe Helary, Isabelle Bataille, Aicha Abed, Corinne Illoul, Annie Anglo, Liliane Louedec, Didier Letourneur, Anne Meddahi-Pelle, and Marie Madeleine Giraud-Guille. Concentrated collagen hydrogels as dermal substitutes. *Biomaterials*, 31(3):481–490, 2010.
- [91] Clarence E Chan and David J Odde. Traction dynamics of filopodia on compliant substrates. *Science*, 322(5908):1687–1691, 2008.
- [92] Dong-Hwee Kim and Denis Wirtz. Focal adhesion size uniquely predicts cell migration. *The FASEB Journal*, 27(4):1351–1361, 2013.
- [93] Günther Schlunck, Hong Han, Thomas Wecker, Daniel Kampik, Tobias Meyer-ter Vehn, and Franz Grehn. Substrate rigidity modulates cell–matrix interactions and protein expression in human trabecular meshwork cells. *Investigative ophthalmology & visual science*, 49(1):262–269, 2008.

- [94] Benjamin Geiger. A 130k protein from chicken gizzard: its localization at the termini of microfilament bundles in cultured chicken cells. *Cell*, 18(1):193–205, 1979.
- [95] JL Coll, A Ben-Ze’ev, RM Ezzell, JL Rodriguez Fernandez, H Baribault, RG Oshima, and ED Adamson. Targeted disruption of vinculin genes in f9 and embryonic stem cells changes cell morphology, adhesion, and locomotion. *Proceedings of the National Academy of Sciences*, 92(20):9161–9165, 1995.
- [96] Dennis E Discher, Paul Janmey, and Yu-li Wang. Tissue cells feel and respond to the stiffness of their substrate. *Science*, 310(5751):1139–1143, 2005.
- [97] Albert K Harris, David Stopak, and Patricia Wild. Fibroblast traction as a mechanism for collagen morphogenesis. 1981.
- [98] Kevin Burton and D Lansing Taylor. Traction forces of cytokinesis measured with optically modified elastic substrata. *Nature*, 385(6615):450–454, 1997.
- [99] Adam J Engler, Shamik Sen, H Lee Sweeney, and Dennis E Discher. Matrix elasticity directs stem cell lineage specification. *Cell*, 126(4):677–689, 2006.
- [100] Ben Harland, Sam Walcott, and Sean X Sun. Adhesion dynamics and durotaxis in migrating cells. *Physical biology*, 8(1):015011, 2011.
- [101] Muhammad H Zaman, Linda M Trapani, Alisha L Sieminski, Drew MacKellar, Haiyan Gong, Roger D Kamm, Alan Wells, Douglas A Lauffenburger, and Paul Matsudaira. Migration of tumor cells in 3d matrices is governed by matrix stiffness along with cell-matrix adhesion and proteolysis. *Proceedings of the National Academy of Sciences*, 103(29):10889–10894, 2006.
- [102] Jorge Alfredo Uquillas, Vipuil Kishore, and Ozan Akkus. Genipin crosslinking elevates the strength of electrochemically aligned collagen to the level of tendons. *Journal of the Mechanical Behavior of Biomedical Materials*, 2012.

- [103] Robert J Kane and Ryan K Roeder. Effects of hydroxyapatite reinforcement on the architecture and mechanical properties of freeze-dried collagen scaffolds. *Journal of the mechanical behavior of biomedical materials*, 7:41–49, 2012.
- [104] GV Stepanov, SS Abramchuk, DA Grishin, LV Nikitin, E Yu Kramarenko, and AR Khokhlov. Effect of a homogeneous magnetic field on the viscoelastic behavior of magnetic elastomers. *Polymer*, 48(2):488–495, 2007.
- [105] Yinling Wang, Yuan Hu, Lin Chen, Xinglong Gong, Wanquan Jiang, Peiqiang Zhang, and Zuyao Chen. Effects of rubber/magnetic particle interactions on the performance of magnetorheological elastomers. *Polymer testing*, 25(2):262–267, 2006.
- [106] Peter CY Chen, Sahan C Herath, Dong-an Wang, Kai Su, Kin Liao, and Harry Asada. Active manipulation of uniaxial ecm stiffness by magnetic anchoring of bio-conjugated beads. In *ASME Summer Bioengineering Conference*, pages 1–14.
- [107] Paul Z Elias and Myron Spector. Viscoelastic characterization of rat cerebral cortex and type i collagen scaffolds for central nervous system tissue engineering. *Journal of the Mechanical Behavior of Biomedical Materials*, 12:63–73, 2012.
- [108] Michael Kaliske and H Rotherth. Formulation and implementation of three-dimensional viscoelasticity at small and finite strains. *Computational Mechanics*, 19(3):228–239, 1997.
- [109] Brian Savage, Dimitri Komatitsch, and Jeroen Tromp. Effects of 3d attenuation on seismic wave amplitude and phase measurements. *Bulletin of the Seismological Society of America*, 100(3):1241–1251, 2010.
- [110] Saber Saffar and Amir Abdullah. Longitudinal wave propagation in multi cylindrical viscoelastic matching layers of airborne ultrasonic transducer; new method to consider the matching layers diameter (frequency <100 khz). *Ultrasonics*, 2013.

- [111] CT Lim, EH Zhou, and ST Quek. Mechanical models for living cellsa review. *Journal of biomechanics*, 39(2):195–216, 2006.
- [112] Tirupathi R Chandrupatla, Ashok D Belegundu, T Ramesh, and Chaitali Ray. *Introduction to finite elements in engineering*. Prentice-Hall Englewood Cliffs, NJ, 1991.
- [113] Jan Lipfert, Xiaomin Hao, and Nynke H Dekker. Quantitative modeling and optimization of magnetic tweezers. *Biophysical Journal*, 96(12):5040–5049, 2009.
- [114] Y Pedro Kato, David L Christiansen, Rita A Hahn, Sheu-Jane Shieh, Jack D Goldstein, and Frederick H Silver. Mechanical properties of collagen fibres: a comparison of reconstituted and rat tail tendon fibres. *Biomaterials*, 10(1):38–42, 1989.
- [115] Cheng Guo and Laura J Kaufman. Flow and magnetic field induced collagen alignment. *Biomaterials*, 28(6):1105–1114, 2007.
- [116] Ronald E Stenkamp, Isolde Le Trong, Lisa Klumb, Patrick S Stayton, and Stefanie Freitag. Structural studies of the streptavidin binding loop. *Protein Science*, 6(6):1157–1166, 1997.
- [117] Harvey Lodish. *Molecular cell biology*. Macmillan, 2008.
- [118] Yue Du, Sahan CB Herath, Qing-Guo Wang, Harry Asada, and Peter CY Chen. Analysis of stiffness in extracellular matrix embedded with bio-conjugated magnetic beads in a magnetic field. *International Journal of Bioscience, Biochemistry and Bioinformatics*, 2(5):329–335, 2012.
- [119] Sahan CB Herath, Peter CY Chen, Yue Du, Shi Hui, Dong-an Wang, Qing-Guo Wang, and Harry Asada. Active manipulation of ecm microscale stiffness. In *International Conference on Environmental, Biomedical and Biotechnology*, volume 41, 2012.
- [120] Peter CY Chen, Sahan CB Herath, Dong-an Wang, and Harry Asada. Active manipulation of ecm stiffness and its effect on endothelial cell migration during angiogenesis. In *Proceedings of the World Congress on Engineering*, volume 1, 2012.

- [121] Shinobu Yanada, Mitsuo Ochi, Nobuo Adachi, Hiroo Nobuto, Muhammad Agung, and Seiichi Kawamata. Effects of cd44 antibody– or rgds peptide–immobilized magnetic beads on cell proliferation and chondrogenesis of mesenchymal stem cells. *Journal of Biomedical Materials Research Part A*, 77(4):773–784, 2006.
- [122] V Conrad-Lapostolle, L Bordenave, and Ch Baquey. Optimization of use of uea-1 magnetic beads for endothelial cell isolation. *Cell biology and toxicology*, 12(4-6):189–197, 1996.
- [123] UO Hafeli. Magnetic nano and microparticles for targeted drug delivery. *MML Series*, 8:77, 2006.
- [124] Chen P. C. Y., S. C. B. Herath, D. A. Wang, K. Su, K. Liao, and H. Asada. Active manipulation of uniaxial ecm stiffness by magnetic anchoring of bio-conjugated beads. In *ASME Summer Bioengineering Conference*, pages 1–14, 2011.
- [125] Kaufman J. D., G. J. Miller, E. F. Morgan, and C. M. Klapperich. Time-dependent mechanical characterization of poly (2-hydroxyethyl methacrylate) hydrogels using nanoindentation and unconfined compression. *Journal of materials research*, 23(05):1472–1481, 2008.
- [126] VanLandingham M. R., J. S. Villarrubia, W. F. Guthrie, and G. F. Meyers. Nanoindentation of polymers: an overview. In *Macromolecular symposia*, volume 167, pages 15–44. Wiley-Blackwell, 111 River Street Hoboken NJ 07030-5774 USA, 2001.
- [127] Emiliios K Dimitriadis, Ferenc Horkay, Julia Maresca, Bechara Kachar, and Richard S Chadwick. Determination of elastic moduli of thin layers of soft material using the atomic force microscope. *Biophysical Journal*, 82(5):2798–2810, 2002.
- [128] Landau L. D., E. M. Lifshitz, J. B. Sykes, W. H. Reid, and E. H. Dill. Theory of elasticity: Vol. 7 of course of theoretical physics. *Physics Today*, 13:44, 1960.
- [129] Dembo M. and Yu-Li Wang. Stresses at the cell-to-substrate interface during locomotion of fibroblasts. *Biophysical journal*, 76(4):2307–2316, 1999.

- [130] William R Thompson. On a criterion for the rejection of observations and the distribution of the ratio of deviation to sample standard deviation. *The Annals of Mathematical Statistics*, 6(4):214–219, 1935.
- [131] Wilhelmine Stefansky. Rejecting outliers by maximum normed residual. *The Annals of Mathematical Statistics*, 42(1):35–45, 1971.
- [132] Kiviranta P., J. Rieppo, R. K. Korhonen, P. Julkunen, J. Töyräs, and J. S. Jurvelin. Collagen network primarily controls poisson’s ratio of bovine articular cartilage in compression. *Journal of Orthopaedic Research*, 24(4):690–699, 2006.
- [133] Hjortdal J. Ø. Regional elastic performance of the human cornea. *Journal of biomechanics*, 29(7):931–942, 1996.
- [134] Schwartz N. J., R. S. Mackay, and J. L. Sackman. A theoretical and experimental study of the mechanical behavior of the cornea with application to the measurement of intraocular pressure. *The bulletin of mathematical biophysics*, 28(4):585–643, 1966.
- [135] Fung Y. C. Elasticity of soft tissues in simple elongation. *American Journal of Physiology–Legacy Content*, 213(6):1532–1544, 1967.
- [136] McKee C. T., J. A. Last, P. Russell, and C. J. Murphy. Indentation versus tensile measurements of young’s modulus for soft biological tissues. *Tissue Engineering Part B: Reviews*, 17(3):155–164, 2011.
- [137] Kreger S. T., B. J. Bell, J. Bailey, E. Stites, J. Kuske, B. Waisner, and S. L. Voytik-Harbin. Polymerization and matrix physical properties as important design considerations for soluble collagen formulations. *Biopolymers*, 93(8):690–707, 2010.
- [138] Donald E Ingber and Judah Folkman. Mechanochemical switching between growth and differentiation during fibroblast growth factor-stimulated angiogenesis in vitro: role of extracellular matrix. *The Journal of cell biology*, 109(1):317–330, 1989.
- [139] Christopher S Chen, Milan Mrksich, Sui Huang, George M Whitesides, and Donald E Ingber. Geometric control of cell life and death. *Science*, 276(5317):1425–1428, 1997.

- [140] Laura E Dike, Christopher S Chen, Milan Mrksich, Joe Tien, George M Whitesides, and Donald E Ingber. Geometric control of switching between growth, apoptosis, and differentiation during angiogenesis using micropatterned substrates. *In Vitro Cellular & Developmental Biology-Animal*, 35(8):441–448, 1999.
- [141] Kevin Kit Parker, AMY Lepre Brock, Cliff Brangwynne, Robert J Mannix, Ning Wang, Emanuele Ostuni, Nicholas A Geisse, Josephine C Adams, George M Whitesides, and Donald E Ingber. Directional control of lamellipodia extension by constraining cell shape and orienting cell tractional forces. *The FASEB Journal*, 16(10):1195–1204, 2002.
- [142] Benjamin D Matthews, Darryl R Overby, Robert Mannix, and Donald E Ingber. Cellular adaptation to mechanical stress: role of integrins, rho, cytoskeletal tension and mechanosensitive ion channels. *Journal of cell science*, 119(3):508–518, 2006.
- [143] Akiko Mammoto, Sui Huang, and Donald E Ingber. Filamin links cell shape and cytoskeletal structure to rho regulation by controlling accumulation of p190rhogap in lipid rafts. *Journal of cell science*, 120(3):456–467, 2007.
- [144] Wei Jiang, Raffaella Sordella, Guang-Chao Chen, Shweta Hakre, Ananda L Roy, and Jeffrey Settleman. An ff domain-dependent protein interaction mediates a signaling pathway for growth factor-induced gene expression. *Molecular cell*, 17(1):23–35, 2005.
- [145] Akiko Mammoto, Kip M Connor, Tadanori Mammoto, Chong Wing Yung, Dongeun Huh, Christopher M Aderman, Gustavo Mostoslavsky, Lois EH Smith, and Donald E Ingber. A mechanosensitive transcriptional mechanism that controls angiogenesis. *Nature*, 457(7233):1103–1108, 2009.
- [146] Tang-Long Shen, Ann Y-J Park, Ana Alcaraz, Xu Peng, Ihnkyung Jang, Pandelakis Koni, Richard A Flavell, Hua Gu, and Jun-Lin Guan. Conditional knockout of focal adhesion kinase in endothelial

- cells reveals its role in angiogenesis and vascular development in late embryogenesis. *The Journal of cell biology*, 169(6):941–952, 2005.
- [147] Elizabeth D Hay. *Cell biology of extracellular matrix*. Springer, 1991.
- [148] Waleed A Farahat, Levi B Wood, Ioannis K Zervantonakis, Alisha Schor, Sharon Ong, Devin Neal, Roger D Kamm, and H Harry Asada. Ensemble analysis of angiogenic growth in three-dimensional microfluidic cell cultures. *PloS one*, 7(5):e37333, 2012.
- [149] Amir Shamloo and Sarah C Heilshorn. Matrix density mediates polarization and lumen formation of endothelial sprouts in vegf gradients. *Lab on a Chip*, 10(22):3061–3068, 2010.
- [150] Brooke N Mason, Alina Starchenko, Rebecca M Williams, Lawrence J Bonassar, and Cynthia A Reinhart-King. Tuning 3d collagen matrix stiffness independently of collagen concentration modulates endothelial cell behavior. *Acta Biomaterialia*, 2012.
- [151] Nathaniel D Kirkpatrick, Stylianos Andreou, James B Hoying, and Urs Utzinger. Live imaging of collagen remodeling during angiogenesis. *American Journal of Physiology-Heart and Circulatory Physiology*, 292(6):H3198–H3206, 2007.
- [152] Grégory Giannone and Michael P Sheetz. Substrate rigidity and force define form through tyrosine phosphatase and kinase pathways. *Trends in cell biology*, 16(4):213–223, 2006.
- [153] Penelope C Georges and Paul A Janmey. Cell type-specific response to growth on soft materials. *Journal of Applied Physiology*, 98(4):1547–1553, 2005.
- [154] Christophe F Deroanne, Alain C Colige, Betty V Nusgens, and Charles M Lapiere. Modulation of expression and assembly of vinculin during *in vitro* fibrillar collagen-induced angiogenesis and its reversal. *Experimental cell research*, 224(2):215–223, 1996.
- [155] Urs O Häfeli and Gayle J Pauer. *In vitro* and *in vivo* toxicity of magnetic microspheres. *Journal of Magnetism and Magnetic Materials*, 194(1):76–82, 1999.

- [156] Dragutin Veličković, FH Uhlmann, K Brandisky, and R Stancheva. *Fundamentals of Modern Electromagnetics for Engineering: Static and Stationary Electrical and Magnetic Field: textbook for Graduate Students*. Technische Universitaet Ilmenau, 2005.
- [157] Benjamin D. Matthews, David a. LaVan, Darryl R. Overby, John Karavitis, and Donald E. Ingber. Electromagnetic needles with sub-micron pole tip radii for nanomanipulation of biomolecules and living cells. *Applied Physics Letters*, 85(14):2968, 2004.
- [158] Yu Xiang, Jacob Miller, Vincent Sica, and David a. LaVan. Optimization of force produced by electromagnet needles acting on superparamagnetic microparticles. *Applied Physics Letters*, 92(12):124104, 2008.
- [159] Zhipeng Zhang, Yanan Huang, and CH Menq. Actively controlled manipulation of a magnetic microbead using quadrupole magnetic tweezers. *Robotics, IEEE Transactions on*, 26(3):531–541, 2010.
- [160] Todd Fallesen, David B Hill, Matthew Steen, Jed C Macosko, Keith Bonin, and George Holzwarth. Magnet polepiece design for uniform magnetic force on superparamagnetic beads. *The Review of scientific instruments*, 81(7):074303, July 2010.
- [161] Usha K Veeramachaneni and R Lloyd Carroll. Magnetic particle motion in a gradient field. In *Proceedings of the COMSOL Conference*, 2007.
- [162] Robert B Vernon and E Helene Sage. Between molecules and morphology. extracellular matrix and creation of vascular form. *The American journal of pathology*, 147(4):873, 1995.
- [163] Donald E Ingber. Mechanical signaling and the cellular response to extracellular matrix in angiogenesis and cardiovascular physiology. *Circulation Research*, 91(10):877–887, 2002.
- [164] Thomas Korff and Hellmut G Augustin. Tensional forces in fibrillar extracellular matrices control directional capillary sprouting. *Journal of Cell Science*, 112(19):3249–3258, 1999.

- [165] Oliver Cassell, OP Stefan Hofer, Wayne A Morrison, and Kenneth R Knight. Vascularisation of tissue-engineered grafts: the regulation of angiogenesis in reconstructive surgery and in disease states. *British journal of plastic surgery*, 55(8):603–610, 2002.
- [166] D Ingber. Mechanochemical control of cell fate switching. *Principles of Tissue Engineering*, Lanza R, Langer R, Vacanti J (eds). Elsevier/Academic Press: London, pages 207–216, 2007.
- [167] Dong-an Wang, Christopher G Williams, Qiang Li, Blanka Sharma, and Jennifer H Elisseff. Synthesis and characterization of a novel degradable phosphate-containing hydrogel. *Biomaterials*, 24(22):3969–3980, 2003.
- [168] Susan J Sofia, V Premnath, and Edward W Merrill. Poly (ethylene oxide) grafted to silicon surfaces: grafting density and protein adsorption. *Macromolecules*, 31(15):5059–5070, 1998.
- [169] Kurt Nilsson and Klaus Mosbach. Immobilization of enzymes and affinity ligands to various hydroxyl group carrying supports using highly reactive sulfonyl chlorides. *Biochemical and biophysical research communications*, 102(1):449–457, 1981.